

PARTICLE TRANSFER AND GAMMA RAY

STUDIES OF ^{144}Pm

PARTICLE TRANSFER AND GAMMA RAY

STUDIES OF ^{144}Pm

By

MALCOLM RONALD MACPHAIL, B.Sc.

A Thesis

Submitted to the School of Graduate Studies

in Partial Fulfilment of the Requirements

for the Degree

Doctor of Philosophy

McMaster University

August 1973

DOCTOR OF PHILOSOPHY (1973)
(Physics)

McMASTER UNIVERSITY
Hamilton, Ontario

TITLE: Particle Transfer and Gamma Ray Studies of ^{144}Pm

AUTHOR: Malcolm Ronald Macphail, B.Sc. (Edinburgh)

SUPERVISOR: Professor R. G. Summers-Gill.

NUMBER OF PAGES: xi, 139

SCOPE AND CONTENTS:

The nuclear structure of ^{144}Pm has been investigated by a combination of particle and γ ray spectroscopy. The $^{143}\text{Nd}(^3\text{He},d)^{144}\text{Pm}$ and $^{143}\text{Nd}(\alpha,t)^{144}\text{Pm}$ reactions revealed a group of twelve levels up to an excitation of 514 keV, and other levels beyond 840 keV. The electromagnetic decays of the levels were found from high resolution singles and coincidence studies of the $^{141}\text{Pr}(\alpha,n\gamma)^{144}\text{Pm}$ and $^{144}\text{Nd}(p,n\gamma)^{144}\text{Pm}$ reactions.

The spins, parities and spectroscopic factors of the low lying levels, determined from the particle transfer and γ ray studies, can be successfully explained in terms of the mixed configurations $\pi 2d_{5/2} \nu 2f_{7/2}$ and $\pi 1g_{7/2} \nu 2f_{7/2}$. The observed γ ray branching ratios are also consistent with this interpretation. Tentative spin and parity assignments have also been made for levels beyond 840 keV.

Shell model calculations employing a surface delta interaction, have been carried out and shown to give reasonable agreement with the experimental data.

ACKNOWLEDGEMENTS

I should like to express my sincere appreciation to all those who have helped in the course of this work. I would especially like to thank:

Professor R. G. Summers-Gill, my supervisor, for his many suggestions and ideas.

The other members of my Supervisory Committee, Drs. J. A. Kuehner and C. Calvo for their guidance.

Past and present members of the group: Hamish Robertson for his insight; Don Dohan and Terry Taylor for their invaluable assistance with the long accelerator experiments; Sherali Hussein, Tony Pierce and Neil Sanderson for their friendship; and Konrad Aniol and Aquila Islam for their help, freely given.

Dave Kelly for assistance with many computer programs.

Brian Cook for many informative discussions.

Phil Ashbaugh and the staff of the accelerator.

Finally, Mrs. Edna Williams for her efforts in typing this thesis.

This work was supported by grants to the group from the National Research Council of Canada. Financial assistance from McMaster University is gratefully acknowledged.

To my mother

TABLE OF CONTENTS

CHAPTER	Page
INTRODUCTION	1
I NUCLEAR THEORY	5
1.1 The Shell Model	5
1.2 N=83 Odd-Odd Nuclei	7
II PROTON TRANSFER STUDIES	10
2.1 Direct Reaction Theory	10
a Stripping Reactions	10
b Spectroscopic Factors	12
c The Distorted Wave Born Approximation (DWBA)	13
2.2 Experimental Outline	15
a The FN Tandem van de Graaff Accelerator	15
b The Enge Spectrograph	19
c Excitation Energies and Cross Sections	21
d Target Preparation	23
2.3 Experimental Results	25
a The $^{143}\text{Nd}({}^3\text{He},d){}^{144}\text{Pm}$ Reaction	25
b $({}^3\text{He},d)$ Angular Distributions	27
c The $^{143}\text{Nd}(\alpha,\epsilon){}^{144}\text{Pm}$ Reaction	32
d $({}^3\text{He},d)/(\alpha,\epsilon)$ Cross Section Ratios	34
e Extraction of Spectroscopic Factors	39

CHAPTER	Page
III GAMMA RAY STUDIES	45
3.1 Introduction	45
3.2 Electromagnetic Transitions in Nuclei	45
3.3 Gamma Ray Singles Studies	48
a Experimental Outline	48
b γ Ray Singles Experiments	49
c $(\alpha, n\gamma)$ and $(p, n\gamma)$ Excitation Functions	56
d X Ray Region in the (α, n) Reaction	59
3.4 γ - γ Coincidence Studies	69
a Experimental Outline	69
b γ - γ Coincidence Results	74
IV LEVEL SCHEME OF ^{144}Pm	78
4.1 Introduction	78
4.2 Energy Levels Below 600 keV	78
a Construction of Low Energy Scheme	78
b Parity Assignments	80
c Spin Assignments	80
d Proton Transfer Reactions	83
e γ Ray Intensity Ratios	84
f Lifetimes	89
g Branching Ratios	90
h Ground State Magnetic Moment	98
4.3 Energy Levels Above 600 keV	102
a Construction of High Energy Scheme	102
b Interpretation of High Energy Scheme	106

CHAPTER

Page

4.4 Shell Model Calculations

107

a Introduction

107

b The Odd-Odd N=83 Nuclei

109

SUMMARY

117

APPENDIX

I A1.1 Level Schemes of ^{143}Pm and ^{145}Pm

119

a Introduction

119

b Experimental Studies

119

c Q Value and Spin Assignments for ^{145}Pm

121

2 A2.1 Q Values

126

3 A3.1 γ Ray Absorption in Targets

129

4 A4.1 Decay of ^{144}Pm

133

REFERENCES

136

LIST OF FIGURES

<u>FIGURE</u>		<u>Page</u>
1.1	Energy levels of the odd proton N=82 nuclei	9
2.1	DWBA angular distributions for the ($^3\text{He},d$) reaction	16
2.2	FN tandem accelerator laboratory	17
2.3	Engel split-pole magnetic spectrograph	20
2.4	Deuteron spectrum from the ($^3\text{He},d$) reaction	28
2.5	Experimental angular distributions for the ($^3\text{He},d$) reaction	31
2.6	Triton and deuteron spectra from the (α,t) and ($^3\text{He},d$) reactions	33
2.7	($^3\text{He},d$)/(α,t) cross section ratios for low lying levels in ^{144}Pm	38
2.8	Spectroscopic factors and spins for low lying levels in ^{144}Pm	41
2.9	($^3\text{He},d$)/(α,t) cross section ratios for high energy levels in ^{144}Pm	44
3.1	Ge(Li) spectra (0.9 cm^3) from the (α,n) and (p,n) reactions	53
3.2	Ge(Li) spectra (50 cm^3) from the (α,n) and (p,n) reactions	54
3.3	γ ray excitation functions for the (α,n) reaction	57
3.4	γ ray excitation functions for the (p,n) reaction	58
3.5	Low energy γ ray spectrum from the (α,n) reaction	65
3.6	Block diagram of γ - γ coincidence system for two detectors	70

FIGURE

		<u>Page</u>
3.7	Block diagram of γ - γ coincidence system for three detectors	73
3.8	Ge(Li) - Ge(Li) coincidence spectra	76
4.1	Proposed level scheme of ^{144}Pm (<600 keV)	79
4.2	(p,n)/(α ,n) γ ray intensity ratios	86
4.3	(α ,n) γ ray intensity ratios	88
4.4	χ^2 plots for branching ratios in ^{144}Pm	96
4.5	Proposed level scheme of ^{144}Pm (>600 keV)	103
4.6	Theoretical spectra of ^{140}La , ^{142}Pr and ^{144}Pm	111
4.7	Root mean square energy deviation for spectra of ^{140}La , ^{142}Pr and ^{144}Pm	112
A1.1	Deuteron spectra from the $^{142}\text{Nd}(^3\text{He},d)^{143}\text{Pm}$ and $^{144}\text{Nd}(^3\text{He},d)^{145}\text{Pm}$ reactions	120
A1.2	($^3\text{He},d$)/(α ,t) cross section ratios for levels in ^{143}Pm and ^{145}Pm	124
A3.1	γ ray attenuation in the (α ,n) and (p,n) reactions	131
A4.1	Decay of strongest lines in (p,n) target	135

LIST OF TABLES

<u>TABLE</u>		<u>Page</u>
2.1	Isotopic composition of target materials	24
2.2	Optical model parameters for the $^{143}\text{Nd}(^3\text{He},d)^{144}\text{Pm}$ reaction	29
2.3	Level energies and proton transfer cross sections for ^{144}Pm	35
2.4	Proton transfer spectroscopic factors for ^{144}Pm	42
3.1	γ ray energy standards	50
3.2	γ ray energies and intensities from the (a,n) and (p,n) reactions	60
3.3	γ ray energies and intensities from impurity reactions	63
3.4	Low energy lines from the (a,n) reaction	67
3.5	Results of γ - γ coincidence experiments	77
4.1	Summed spectroscopic factors from proton transfer reactions to ^{144}Pm	85
4.2	(p,n)/(a,n) γ ray intensity ratios	92
4.3	Gyromagnetic ratios used in branching ratio analysis	93
4.4	Wave vectors from proton transfer and γ ray studies	97
4.5	Relative phases for β amplitudes	99
4.6	Comparison of calculated and experimental branching ratios	100
4.7	Experimental and theoretical configuration mixing amplitudes	114
A1.1	Level energies and proton transfer cross sections for ^{143}Pm	122

TABLE

Page

A1.2 Level energies and proton transfer cross sections
for ^{145}Pm

123

A2.1 ($^3\text{He},d$) Q values

127

A3.1 Uncertainties in γ ray attenuation

132

INTRODUCTION

The nuclear force has proved to be so complex that no exact description of it yet exists more than 60 years after it was first proposed. Our present understanding of nuclear properties has thus evolved from attempts to classify experimental information in terms of a simple model of the nucleus. The situation, however, is characterized by the existence of several nuclear models, each one being able to describe either a certain type of reaction or having its applicability to restricted groups of nuclei.

One of the most successful nuclear models, the shell model (Mayer 1948, 1949; Haxel, Jensen and Suess 1948, 1949), has met with considerable success in accounting for the properties of odd mass spherical nuclei. Nuclei in the regions of singly and doubly closed shells are of special interest, since their properties can be understood in terms of a relatively simple shell model. Included in this category are the series of odd-odd nuclei with 83 neutrons, one beyond a closed shell of 82.

The low lying levels of these nuclei are expected to arise from the $2d_{5/2}$ and $1g_{7/2}$ proton configurations, and the $2f_{7/2}$ neutron configuration only, thus affording an excellent opportunity to apply the techniques of the shell model. This region is probably one of the most appropriate of the periodic table in which to systematically study residual neutron-proton interactions. Unfortunately, on account of the difficulties in studying nuclei with high level densities, the experimental information was very limited. Within the

last decade, however, the advent of fast computers and sophisticated experimental techniques have enabled both theoretical and experimental investigations to extend to a wider range of nuclei, including odd-odd nuclei.

The N=83 odd-odd nuclei, which include ^{134}Sb , ^{136}I , ^{138}Cs , ^{140}La , ^{142}Pr , ^{144}Pm , ^{146}Eu and ^{148}Tb , differ by the successive addition of two protons beyond the Z=50 closed shell. The extreme members of this series are perhaps the most difficult to study since they are too far from the region of stability to be reasonably accessible. The β and γ ray decay of the fission product ^{138}Xe has been the subject of several investigations. In the most recent by Monnard et al. (1972) low spin states in ^{138}Cs were identified up to an excitation of 2300 keV.

Investigations of the β decay of ^{140}Ba to ^{140}La , performed by several groups (Geiger et al. 1961, Agarwal et al. 1964 and Burde et al. 1965), resulted in a number of spin-parity assignments, as well as lifetime determinations. ^{140}La and ^{142}Pr were extensively studied by Kern et al. (1967, 1968) and Journey et al. (1970) by means of high resolution (d,p) and (n, γ) reactions. The spins, parities and decay properties of many of the low lying levels were thus found.

^{144}Pm , next in this series, has been the subject of very little study. Investigations of the $^{144}\text{Pm}(\text{o.c.})^{144}\text{Nd}$ reaction (Raman 1967, and Arya et al. 1971), and the α decay of ^{148}Eu (Toth et al. 1964) indicate a 5^- spin-parity assignment for the

ground state. The level structure of ^{144}Pm was otherwise completely unknown. Neither ^{142}Pr nor ^{144}Pm can be studied by β decay because their neighbouring isobars are stable. Lastly, ^{146}Eu was investigated following the decay ^{146}Sm by Antman et al. (1970) who identified several low spin states.

Many of these experiments have allowed only specific nuclear properties to be studied. While this can be an asset in understanding complicated nuclei, it also gives an incomplete picture. The present work was undertaken to provide additional experimental information necessary for the evaluation of detailed theoretical studies of the odd-odd $N=83$ nuclei, and has utilized the techniques of both particle and γ ray spectroscopy.

Initially the $^{144}\text{Nd}(d,\alpha)^{142}\text{Pr}$ reaction was investigated together with singles and coincidence γ ray studies of the $^{139}\text{La}(\alpha,n\gamma)^{142}\text{Pr}$ and $^{142}\text{Ce}(p,n\gamma)^{142}\text{Pr}$ reactions to locate certain low lying levels not observed by Kern et al. (1968). This work, in addition to high resolution (d,p) studies of Hussein (1973), enabled the $J=6$ and 7 levels to be identified. This was later confirmed by the work of Aniol (1973). Subsequently, a study of ^{144}Pm was performed and is described in detail in this thesis.

Since the level structure of ^{144}Pm had not previously been investigated, the $^{143}\text{Nd}(^3\text{He},d)^{144}\text{Pm}$ and $^{143}\text{Nd}(\alpha,p)^{144}\text{Pm}$ proton transfer reactions were carried out, as described in chapter II, to establish the energy levels, spectroscopic factors and possible spins and parities. The results of $^{141}\text{Pr}(\alpha,n\gamma)^{144}\text{Pm}$ and

$^{144}\text{Nd}(p,n\gamma)^{144}\text{Pm}$ experiments were essential in the construction of the level scheme. The γ ray studies, which included high resolution singles and coincidence experiments, are discussed in chapter III.

In chapter IV the interpretation of the experimental data and resulting level scheme are discussed in the light of the shell model. The useful techniques which emerged from the data analysis are also described.

Chapter I
NUCLEAR THEORY

1.1 The Shell Model

The most important tool in ordering and relating experimental data on nuclei and their reactions has been the shell model. The model is easily formulated: nucleons in a nucleus move independently of each other in an average single particle potential. It is difficult to visualize and derive such a model from first principles, in view of the fact that the nucleon-nucleon force has a short range attractive component ($\sim 10^{-13}$ cm), and a highly repulsive hard core. One would have to extend the Hartree-Fock method of atomic physics to the many body problem, replacing the actual nucleon-nucleon interaction by an effective interaction. The more usual approach has been to use an appropriate average field to provide a complete set of single particle wavefunctions. For mathematical convenience, the field which is generally adopted corresponds to a three dimensional harmonic oscillator. The inclusion of a strong spin-orbit term is required to reproduce the experimental level ordering and the "magic numbers".

For a nucleus in its ground state, one can expect all the orbitals of lowest energy to be filled in accordance with the Pauli Exclusion Principle, which allows each single particle state to contain at most two nucleons. The principle also supports the idea of using an average central potential, because nucleons in

the low lying states cannot be scattered into other states which are already occupied. Since the central potential does not completely account for the forces between the nucleons, certain residual interactions are introduced, the most important being the pairing force which causes an even number of protons (or neutrons) to couple to give a ground state with zero total angular momentum. This is in agreement with known ground state spins of all even-even nuclei.

In the extreme single particle shell model, the ground state spin, parity and electromagnetic moments are attributed to the last unpaired nucleon in odd-A nuclei. While this is found experimentally for nuclei near the "magic" shells, which constitute very stable systems, or inert cores, there are many exceptions for nuclei which are removed from them. A more realistic shell model treatment would include the effects of several nucleons beyond an inert core.

To carry out such a calculation, a residual two body interaction, v_{ij} , is introduced to account for the interaction between the extra-core nucleons. The Hamiltonian, H , for a system of A nucleons, k of which are treated as extra-core or valence nucleons,

$$H = H_0 + \sum_{i,j}^k v_{ij},$$

where the summation extends over the valence nucleons only. H_0 is comprised of a simple harmonic oscillator potential and a spin orbit term, giving rise to eigenfunctions which constitute a complete set of single particle states. Each state is defined by its principal quantum number n , orbital angular momentum quantum

number l , and total spin quantum number j .

Multiparticle antisymmetric wavefunction for the valence nucleons are determined from single particle wavefunctions, and comprise the basis for evaluating the matrix elements of the residual interaction. It is then possible to find the eigen-values and wavefunction of the nuclear states by diagonalizing the Hamiltonian matrix. A more detailed account of the shell model and shell model calculations can be found in numerous articles (eg. de Shalit and Talmi 1963, Mang and Weidenmuller 1968).

The shell model can also be generalized to include collective nuclear motion. In fact the shell model employs an average field in which the nucleons move and which is generated collectively by all the nucleons. In the usual shell models, this field is considered a static quantity, but a more complete description must take into account variables in the field associated with collective motion. Collective models of the nucleus have been discussed in numerous works (e.g. Davidson 1968, Rowe 1970, Eisenberg and Greiner 1972). For nuclei with few nucleons outside closed shells, however, the static shell model is most convenient.

1.2 N=83 Odd-Odd Nuclei

On the basis of the shell model the low lying levels of the odd-odd N=83 nuclei should be explicable in terms of interactions between the protons outside the Z=50 closed shell and the single neutron outside the N=82 closed shell. The proton orbits of interest, before the shell closure of Z=82, are $1g_{7/2}$, $2d_{5/2}$, $1h_{11/2}$, $2d_{3/2}$ and

$3s_{1/2}$, as shown in Fig. 1.1, while the odd neutron may be ascribed to the $2f_{7/2}$ orbit. Experimental support for these assignments is provided by the proton transfer studies of Wildenthal et al. (1971), and the neutron transfer work cited by McGowan et al. (1969).

It is thus reasonable to assume that the low lying levels of the odd-odd nuclei arise from coupling the $2f_{7/2}$ neutron to the protons in the $1g_{7/2}$ and $2d_{5/2}$ states. The latter are conveniently described using the quasiparticle formalism which incorporates the important pairing correlations among these protons (Struble 1967). In this picture, the coupling of the $2f_{7/2}$ neutron to the single $1g_{7/2}$ and $2d_{5/2}$ quasiproton states gives rise to fourteen states of the form

$$|JM\rangle_1 = \alpha_1 |\pi 2d_{5/2} \nu 2f_{7/2}; JM\rangle + \beta_1 |\pi 1g_{7/2} \nu 2f_{7/2}; JM\rangle$$

and

$$|JM\rangle_2 = \alpha_2 |\pi 2d_{5/2} \nu 2f_{7/2}; JM\rangle + \beta_2 |\pi 1g_{7/2} \nu 2f_{7/2}; JM\rangle.$$

For $J=0$ and 7 the α amplitudes are zero. Normalization and orthogonality conditions require

$$(\alpha_1^2 + \beta_1^2) = (\alpha_2^2 + \beta_2^2) = 1$$

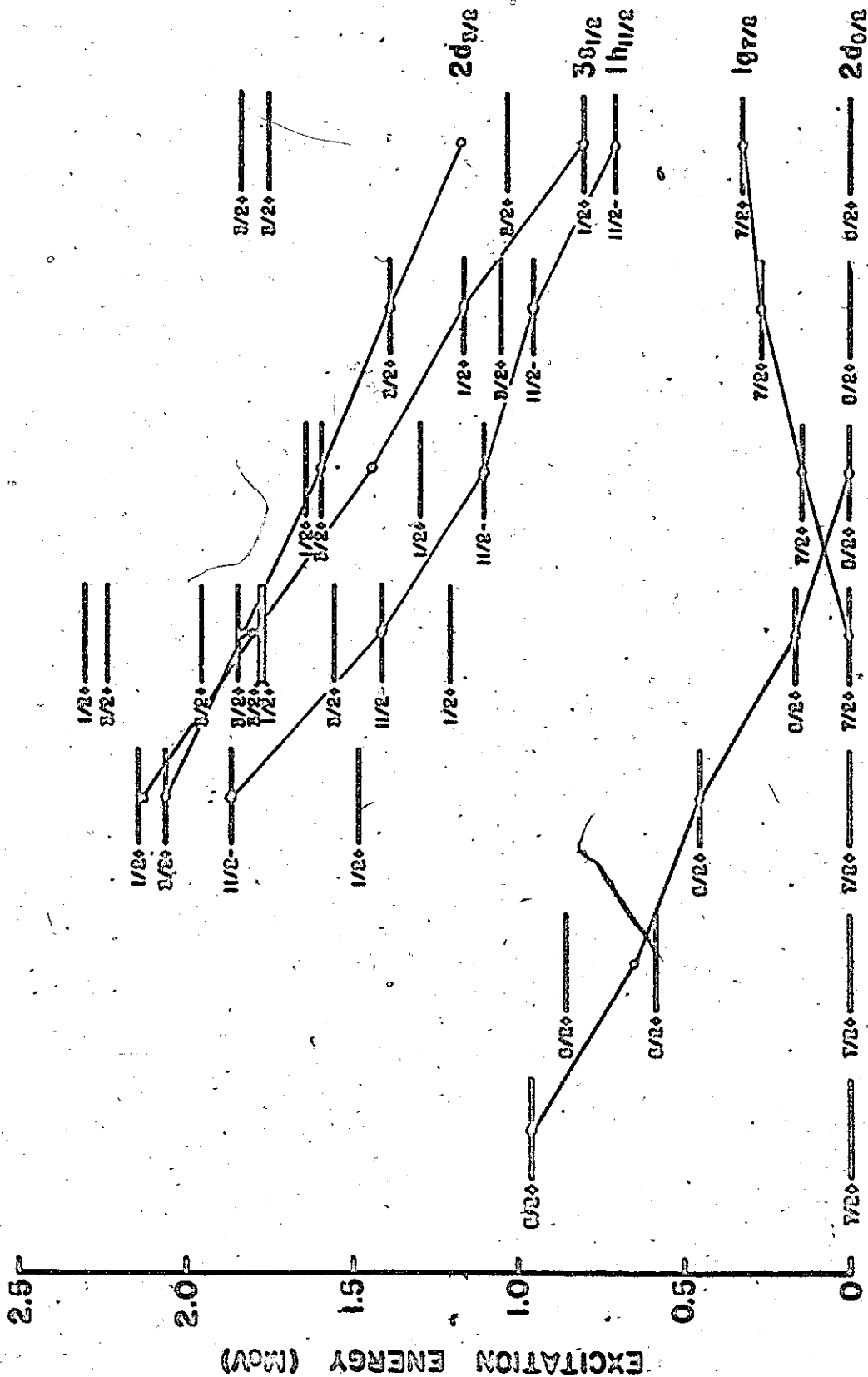
and

$$\alpha_1 \alpha_2 + \beta_1 \beta_2 = 0.$$

The studies of Kern et al. (1967, 1968) and Jurney et al. (1970) have demonstrated that such a model gives a good description of the low lying levels of both odd-odd nuclei ^{140}La and ^{142}Pr . Spectroscopic factors and γ ray branching ratios for these nuclei could be reproduced quite well from empirical values of α and β .

Fig. 1.1

Levels of the odd proton $N=82$ nuclei. The sloping lines join the centroids of the $2d_{5/2}$, $1g_{7/2}$, $1h_{11/2}$, $3s_{1/2}$ and $2d_{3/2}$ orbits, as indicated. Data taken from Wildenthal et al. (1971) and Holm et al. (1970).



1000 1050 1100 1150 1200 1250 1300 1350



Chapter II

PROTON TRANSFER STUDIES

2.1 Direct Reaction Theory

2.1a Stripping Reactions

One of the most valuable sources of information on the structure of both stable and unstable nuclei is the study of particle transfer reactions. Such reactions are conveniently classified as direct, if the transition from the initial state to the final state proceeds with minimum rearrangement of the nucleons in the target, or compound, if the reaction involves complicated intermediate states. A judicious choice of reaction products and an understanding of the reaction mechanism enable specific nuclear properties to be studied.

The most studied and best understood reactions of this type are the single nucleon stripping (and pick-up) reactions, in which one nucleon is exchanged between a light projectile and a target nucleus. The stripping reaction transfers a single nucleon to one of the unfilled states in the target nucleus, whereas the pick-up reaction removes a nucleon from one of the occupied states. In the simplest case, where a nucleon (n, l, j) is transferred to a target with spin J_A to form a final state with spin J_B , the experimental differential cross section $\left(\frac{d\sigma}{d\Omega}\right)_{nlj}^{\text{exp}}$ can be written as the product

$$\left(\frac{d\sigma}{d\Omega}\right)_{nlj}^{\text{exp}} = S(nlj) \frac{2J_B + 1}{(2J_A + 1)} \left(\frac{d\sigma}{d\Omega}\right)_{nlj}^{\text{DWBA}} \quad 2.1$$

where $\left(\frac{d\sigma}{d\Omega}\right)_{nlj}^{DWBA}$ is a theoretical cross section, calculated using the Distorted Wave Born Approximation (DWBA), discussed in section 2.1c. N is a normalization factor which depends on the type of incident and outgoing particles involved. $S(nlj)$, usually referred to as the spectroscopic factor, is a measure of the single particle component (nlj) in the final nuclear state. It will be convenient in the subsequent analysis if relative spectroscopic factors are considered rather than absolute spectroscopic factors. The number of (nlj) vacancies (or holes) in the target can thus be included in the calculation of $\left(\frac{d\sigma}{d\Omega}\right)_{nlj}^{DWBA}$.

To extract information on the states of interest, a comparison is made between the shapes of the experimentally measured angular distributions and those computed for different (nlj) transfers. The shapes of the angular distributions are characteristic of the l value of the transferred nucleon, the j dependence being relatively small. For a given state, the complete (nlj) specification is deduced by a combination of assumptions and deductions based on a general nuclear model. The spectroscopic strength, denoted by $(2J_B + 1) S(nlj)$, can thus be extracted using equation 2.1, and compared with model calculations.

An alternative method of obtaining l values, is to compare two direct reactions that transfer the same single nucleon between the same initial and final states. The reactions differ only in the identity of the spectator nucleons, e.g. $(^3\text{He}, d)$ and (α, t) reactions, which transfer a proton to a given target. The ratio of the cross

sections for such reactions depends on the appropriate l and Q values but, from equation 2.1, is independent of the spectroscopic strength and target spin. By comparing the experimental ratio for a given level with those computed for different l values, one can infer the l value of the transferred nucleon.

In cases where a state can be populated by more than one (nlj) transfer, the experimental cross section can be written as the sum of the cross sections for the individual (nlj) components.

$$\text{Hence } \left(\frac{d\sigma}{d\Omega}\right)^{\text{exp}} = \sum_i \left(\frac{d\sigma}{d\Omega}\right)^{\text{exp}}_{(nlj)_i}$$

The cross section ratio, R , is then dependent on the spectroscopic factor for each (nlj) transfer, and is given by

$$R = N \sum_i S(nlj)_i \left(\frac{d\sigma}{d\Omega}\right)^{\text{DWBA}}_{(nlj)_i} / N' \sum_k S(nlj)_k \left(\frac{d\sigma}{d\Omega}\right)^{\text{DWBA}}_{(nlj)_k}$$

where the primed quantities distinguish the two reactions considered.

2.1b Spectroscopic Factors

The spectroscopic factor $S(nlj)$ depends on the detailed structure of target and residual nuclei. It is defined as the overlap between the final nuclear state and the initial nuclear state, coupled to that of the transferred nucleon, and satisfying anti-symmetrization requirements. Spectroscopic factors obey sum rules, which provide a method for separately studying the properties of the target and residual nuclei. The general treatment of sum rules and the evaluation of spectroscopic factors has been discussed in several works (e.g. MacFarlane and French 1960).

In the case of proton transfer to form ^{144}Pr , the spectroscopic factors can be easily calculated if it is assumed that the low lying levels arise from the coupling of $2d_{5/2}$ and $1g_{7/2}$ proton states to a $2f_{7/2}$ neutron state, which is the ground state of ^{143}Nd . The final nuclear states have wavefunctions of the form

$$\psi_{J_B} = \alpha_{J_B} |\pi 2d_{5/2} \nu 2f_{7/2}; J_B\rangle + \beta_{J_B} |\pi 1g_{7/2} \nu 2f_{7/2}; J_B\rangle$$

and the target state is

$$\psi_{J_A} = |\nu 2f_{7/2}; J_A = 7/2\rangle.$$

Treating ^{142}Nd as an inert core during the proton transfer, one

obtains

$$S(2d_{5/2}) = \alpha_{J_B}^2, \quad S(1g_{7/2}) = \beta_{J_B}^2,$$

so that $\sum_{n,l,j} S(n,l,j) = 1$ for a given final state.

2.1c The Distorted Wave Born Approximation (DWBA)

DWBA is, at present, one of the most widely used methods of approximation in the analysis of single nucleon transfer reactions.

It has been the subject of numerous studies (Satchler 1964, 1965), so that only an outline is given here. Since the exact details of the interaction between the colliding particles require a complete knowledge of the nuclear force, certain approximations must be made in calculating reaction cross sections.

DWBA assumes that elastic scattering is the dominant process when two nuclei collide, and that reactions may be treated using the methods of perturbation theory. The elastic scattering, caused by the long range Coulomb force and the short range nuclear force, is

approximated by a phenomenological two body potential - the optical potential. The parameters associated with the optical potentials are chosen so as to satisfy experimental data from elastic scattering experiments, and in some cases are further adjusted to reproduce the observed angular distributions for states with well known properties. The matrix element describing the transition, contains the elastic scattering wave functions (the distorted waves in the approximation) generated by the optical potentials, and an effective interaction responsible for the transition between these elastic scattering states. The evaluation of the matrix element is greatly simplified by the introduction of a zero-range approximation, which assumes that the outgoing particle is emitted at the same point at which the incident particle is absorbed. Calculations by Austern (1964) show that the inclusion of finite range effects does not appreciably change the shapes of the computed angular distributions, although their magnitudes are modified.

Several computer codes have been constructed to calculate DWBA angular distributions without further approximations. The one used in the present work, called "DWUCK", was written by P.D. Kunz at the University of Colorado, and modified by J.C. Tippet for the CDC6400 computer at McMaster University. Using DWUCK it is possible to include first order effects due to a finite range interaction, and also due to the non-local nature of the optical potentials (Percy and Buck 1962).

DWBA analyses have been employed extensively to interpret

reaction data throughout the periodic table. In particular, properties of the odd proton $N=82$ nuclei have been extracted from the proton transfer work of Wildenthal et al. (1971). Numerous studies of the odd neutron nuclei in this mass region have also been analyzed in terms of DWBA theory (McGowan et al. 1969). The calculated angular distributions for the different $(n\ell j)$ transfers expected in the $^{143}\text{Nd}(^3\text{He}, d)^{144}\text{Pm}$ reaction are shown in Fig. 2.1.

2.2 Experimental Outline

2.2a The FN Tandem van de Graaff Accelerator

The experimental investigations of ^{144}Pm , carried out at the McMaster Tandem van de Graaff Laboratory, involved studies of the $^{143}\text{Nd}(^3\text{He}, d)^{144}\text{Pm}$, $^{143}\text{Nd}(\alpha, t)^{144}\text{Pm}$, $^{141}\text{Pr}(\alpha, n\gamma)^{144}\text{Pm}$ and $^{144}\text{Nd}(p, n\gamma)^{144}\text{Pm}$ reactions. As in nearly all studies of this nature, a basic requirement is a stable beam of particles, which is spatially well defined. The production of such a beam, and a description of supporting equipment are outlined in this section.

The main components of the accelerator comprise the negative ion source, high voltage system and beam transport system (Fig. 2.2). A negatively charged ion beam is initially produced by a duoplasmatron, or a radio frequency source. In the former, used in the present studies, a hot cathode (filament) generates thermionic electrons which give rise to an arc discharge in the presence of a plasma: He for α beams; H for proton beams; and D for deuteron beams. The positive ions thus produced, pass into a gaseous canal where negative ions are formed by the process of charge exchange. (The direct

Fig. 2.1

DWBA deuteron angular distributions for $l = 0, 2, 4$
and 5 transfers in the $^{143}\text{Nd}(^3\text{He},d)^{144}\text{Pm}$ reaction. The
optical model parameters employed are given in Table 2.2.

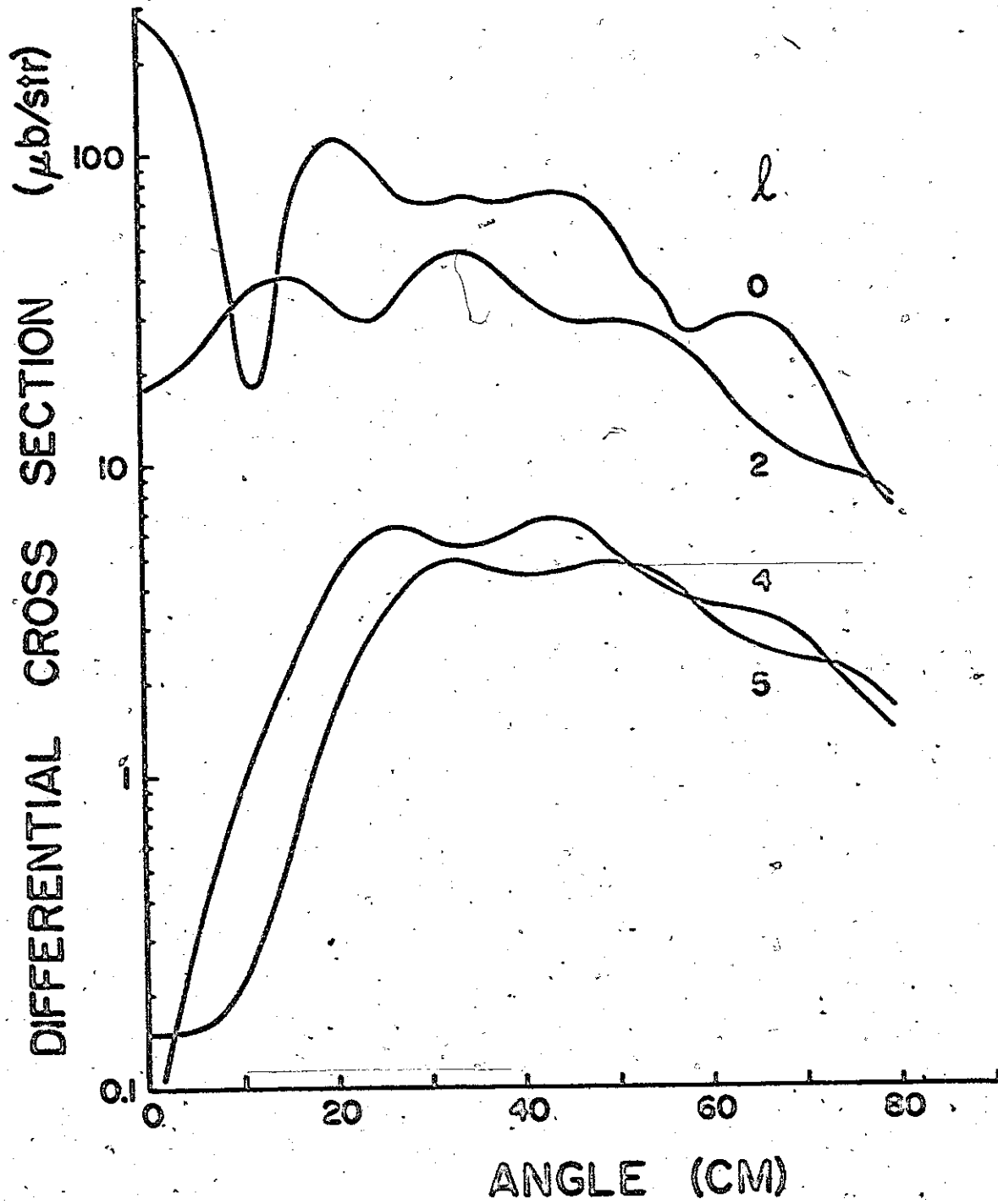
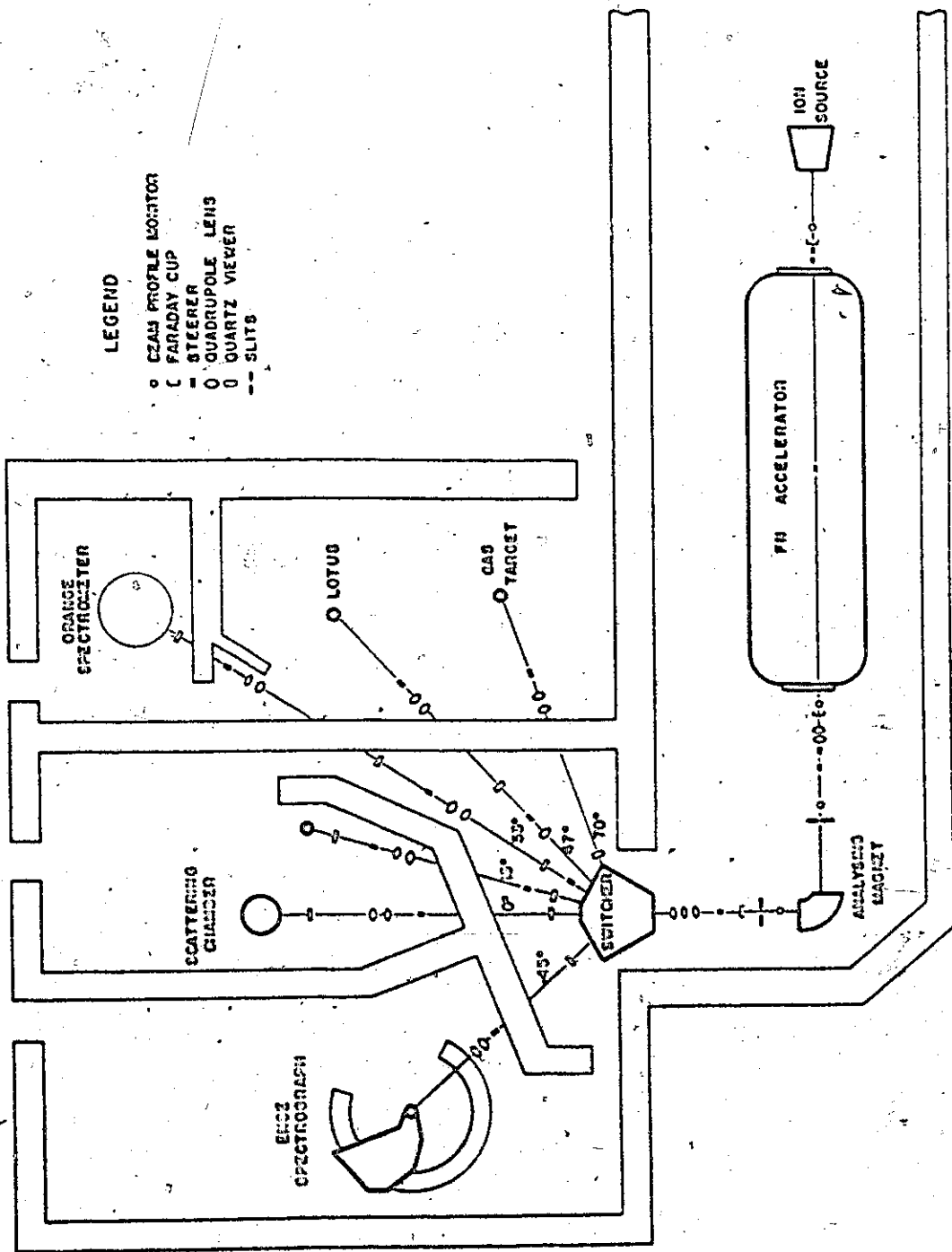


Fig. 2.2

Schematic plan (not to scale) of the FN Tandem Accelerator Laboratory at McMaster showing the location of beam handling elements and shielding walls.



LEGEND

- BEAM PROFILE MONITOR
- ⊂ FARADAY CUP
- STEERER
- QUADRUPOLE LENS
- QUARTZ VIEWER
- SLITS

extraction of negative ions from the plasma would result in a beam of very low intensity.) The negatively charged ions, emerging from the canal, pass through a magnetic field to remove unwanted ions, before accelerating towards the high voltage terminal, located inside a large tank containing pressurized SF_6 gas for electrical insulation. The necessary focussing and steering are provided by quadrupole magnets and electrostatic plates. The terminal can be maintained at a positive potential (≤ 9 MV) by means of a fast moving endless belt, which effectively transports electrons from the terminal to ground potential.

In the terminal, the negative ions are stripped of a number of electrons while passing through a thin ($\sim 20 \mu\text{g}/\text{cm}^2$) carbon foil. After the beam becomes positively charged it experiences an additional acceleration away from the terminal. The total energy of the beam, emerging from the tank, is essentially $(1 + n)V$ electron volts, where n is the charge state of the emerging ion and V is the terminal voltage. For light particles all electrons can be removed from the ion, so that one can produce proton and deuteron beam energies ≤ 18 MeV, and ^3He and α beam energies ≤ 27 MeV.

After further focussing, the beam is defined by a set of object slits and analyzed by a 90° magnet which selects ions of the appropriate momentum and charge, for transmission through a set of image slits. An automatic feedback control mechanism, monitoring the amount of beam hitting these slits, serves to stabilize the terminal voltage. A switching magnet then directs the beam to one of the

experimental areas where it is finally steered and focussed on to the target. For the present studies, beam spot sizes were 1 mm in diameter, and beam stabilities were <3 keV over an extended period (~70 hours).

The available experimental facilities include: an "Orange" beta ray spectrometer for conversion electron studies; a "Lotus" for multi-detector gamma ray angular correlation studies; an Enge split-pole magnetic spectrograph; a general purpose scattering chamber; and a Ge(Li) detector goniometer.

2.2b The Enge Spectrograph

A schematic diagram of the Enge spectrograph, employed in the ($^3\text{He}, d$) and (α, t) investigations, is presented in Fig. 2.3. The instrument has been described in detail by Spencer and Enge (1966). The salient features of this device include a large solid angle of acceptance ($\sim 2\text{msr}$), second order focussing over a large momentum range ($p_{\text{max}}/p_{\text{min}} \approx 2.8$), and the ability to compensate for kinematic broadening. The high resolution which can be obtained was essential for the present studies.

Charged particles, emitted from the target at a given angle, enter the spectrograph and are deflected by the magnetic field. The subsequent path followed by each particle depends on its mass (M), charge (q), and energy (E), as well as the magnetic field (B). Those with the same magnetic rigidity ($\sqrt{\frac{2ME}{q}}$) are focussed to the same position along the focal plane appropriate for the reaction, and are detected by means of photographic emulsions (Kodak NTB photographic

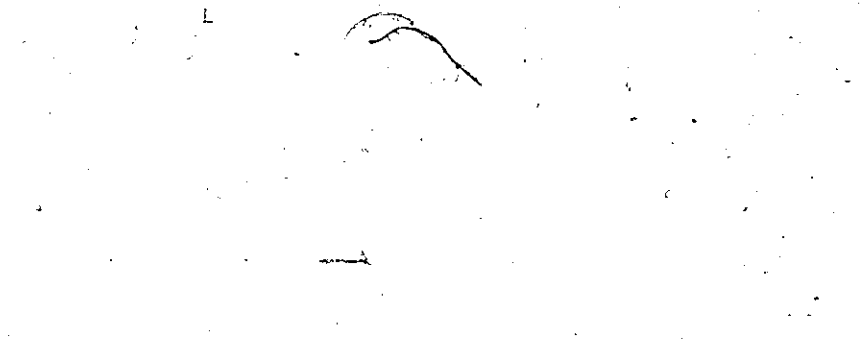

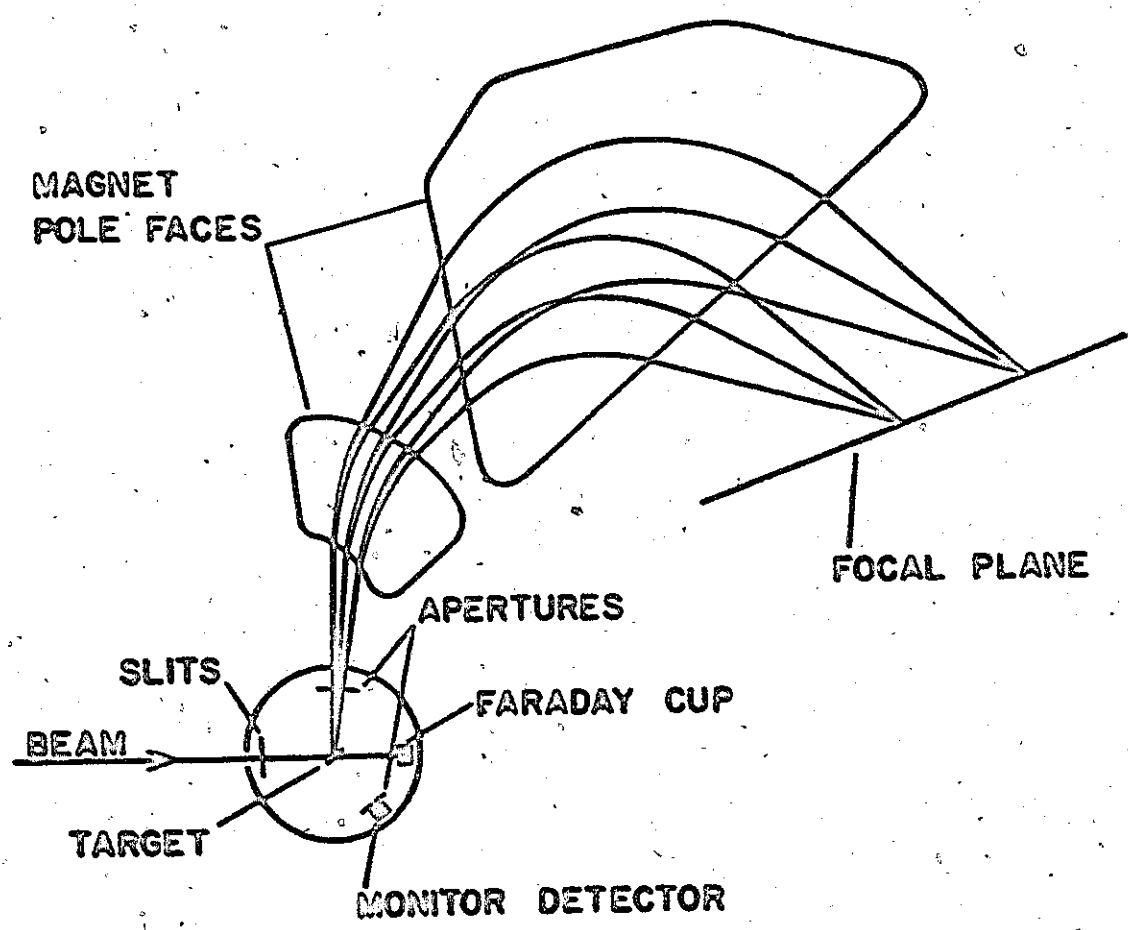


Fig. 2.3

Schematic diagram of the Enge split pole magnetic spectrograph. Several trajectories through the field are shown for particle groups in the focal plane.





emulsions 50 μ m thick were used throughout this work) placed along the focal plane. After development, the plates are scanned in 1/4mm strips with a specially constructed microscope.

2.2c Excitation Energies and Cross Sections

The effective radius of curvature (ρ), describing the particle trajectory, is related to the plate position (s) by the expression

$$\rho = \sum_{i=0}^4 a_i s^i,$$

where the coefficients for $s \leq 50$ cm have the values: $a_0 = 8.92478 \times 10^1$ cm, $a_1 = -4.0732 \times 10^{-1}$, $a_2 = 3.8920 \times 10^{-4}$ cm⁻¹, $a_3 = -9.9143 \times 10^{-6}$ cm⁻² and $a_4 = 9.8126 \times 10^{-8}$ cm⁻³.

The calibration was performed with a radioactive source of α particles (ThC) with well known energies (Burke 1969). Measurements of s for different magnetic field strengths, measured by a NMR fluxmeter, permitted the a_i coefficients to be determined.

It is then possible to calculate the energies of the various particle groups observed in a given reaction, and hence the energies of the states in the residual nuclei. All spectrograph kinematics analyses employed the appropriate relativistic expressions given by Marion and Young (1968). For each state one can also determine the reaction cross section from a knowledge of the peak intensities (n_R). One such approach is to measure the target thickness (M/A), the total integrated beam charge (Q), and the spectrograph solid angle ($\Delta\Omega_R$). Thus n_R is related to the differential cross section, $(\frac{d\sigma}{d\Omega})_R$, by

$$n_R = \left(\frac{Q}{2c}\right) \left(\frac{N_0}{V}\right) \left(\frac{M}{A}\right) \left(\frac{d\sigma}{d\Omega}\right)_R \Delta\Omega_R \quad \text{where } c \text{ is the electronic}$$

charge, N_0 is Avogadro's number, W is atomic weight of target and Z is the charge state of the incident particles. (The centre of mass system of coordinates is considered rather than the laboratory system.) Perhaps the most difficult measurement involves the target thickness. In the course of an experiment the beam may cause the target to deteriorate significantly, so that the target thickness changes during an exposure. Non-uniformities in the target further modify the effective thickness.

The method which was adopted in the present work required the elastically scattered particles to be monitored during the experiment. The monitor spectra, which were obtained with a small Si(Li) surface barrier detector, were stored in a Nuclear Data 1100 analyzer, and typed out at the end of each exposure. The differential cross section and peak intensity for elastic scattering from the target material are also related by the expression

$$n_E = \left(\frac{Q}{Ze}\right) \left(\frac{N_0}{W}\right) \left(\frac{M}{A}\right) \left(\frac{d\sigma}{d\Omega}\right)_E \Delta\Omega_E$$
 where the subscript E refers to the elastic scattering process. Combining this expression with

that for the reaction process one has

$$\left(\frac{n_E}{n_R}\right) = \left(\frac{d\sigma}{d\Omega}\right)_E / \left(\frac{d\sigma}{d\Omega}\right)_R \left(\frac{\Delta\Omega_E}{\Delta\Omega_R}\right),$$

which is independent of the target thickness. The elastic scattering cross section can be determined with sufficient accuracy from DWBA calculations and is essentially the Rutherford cross section for angles $< 30^\circ$ in both the ($^3\text{He}, d$) and (α, t) reactions.

The extraction of peak centroids and areas was facilitated by the computer program SPECTR (O'Neil 1970), which fits all peaks to a

standard shape. After subtracting a specified background, the program performs a non-linear least squares fit, over the spectrum, to a skewed gaussian function. The function has the form

$$I(x) = I(x_0) [e^{-\delta_0(x-x_0)^2} + \gamma e^{-\beta(x-x_1)} (1 - e^{-\delta_1(x-x_0)^2})]$$

where x = plate position,

$I(x)$ = intensity at position x ,

δ_0, δ_1 = gaussian width parameters,

x_0, x_1 = gaussian peak and exponential positions,

β = constant determining the exponential fall-off,

and γ = parameter defining the contribution of the exponential terms.

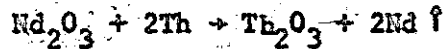
In each spectrum the peak shape parameters are determined for several well resolved peaks, and interpolated (extrapolated) in a linear fashion for the remaining peaks.

2.2d Target Preparation

The several targets, used in the proton transfer experiments, were made from both natural and isotopically enriched oxides of neodymium. The isotopic compositions of the target materials, given in Table 2.1, are those stated by the supplier (Union Carbide Corporation). The most convenient method of preparation was vacuum evaporation of the oxide in the presence of a reducing agent thorium, a technique which has proved successful for many rare earth oxides (Westgaard and Björnsholm 1966). The mixture (15 mgm Nd_2O_3 + 30 mgm Th) was heated in a tantalum crucible by means of an electron gun, to produce the reaction,

Table 2.1

Target	Isotopic Composition (At %)						
	142	143	144	145	146	148	150
¹⁴² Nd	97.55	1.20	0.77	0.17	0.23	0.05	0.04
¹⁴³ Nd	2.41	91.06	4.43	0.39	1.50	0.14	0.09
¹⁴⁴ Nd	0.60	0.57	97.51	0.68	0.47	0.10	0.07
Natural Nd	27.11	12.17	23.85	8.30	17.22	5.73	5.62



The Nd metal condensed onto commercial backings (Yissum Research Development Company) of carbon ($30 \mu\text{g}/\text{cm}^2$ and $50 \mu\text{g}/\text{cm}^2$), on microscope slides, placed ~ 10 cm above the crucible. Sections of the carbon foil were later floated off the slides in distilled water, and mounted on aluminum target frames. The thickness of each target was estimated using an α -scattering device constructed by J.C. Tippett, and was typically $50 \mu\text{g}/\text{cm}^2$.

The study of odd-odd nuclei by proton transfer reactions necessitates targets of high chemical and isotopic purity, since the typical cross sections are smaller than those for reactions on the neighbouring even-even isotopes, which usually constitute the main isotopic impurities. Further, the kinematic shift with angle is insufficient to distinguish reactions on adjacent mass targets with $A \sim 143$. For complete identification of the reaction products, targets of different isotopic compositions are required. Hence targets of ^{142}Nd , ^{144}Nd and natural Nd were also prepared. The compositions of each target used in the present work, was investigated by exposing emulsions to record the elastic scattering of a 24 MeV ^3He beam at a laboratory angle of 30° . The target impurities included carbon, oxygen, silicon and small amounts (typically $< 1\%$) of a heavy mass contaminant, presumably thorium from the reduction process.

2.3 Experimental Results

2.3a The $^{143}\text{Nd}(^3\text{He},d)^{144}\text{Pm}$ Reaction

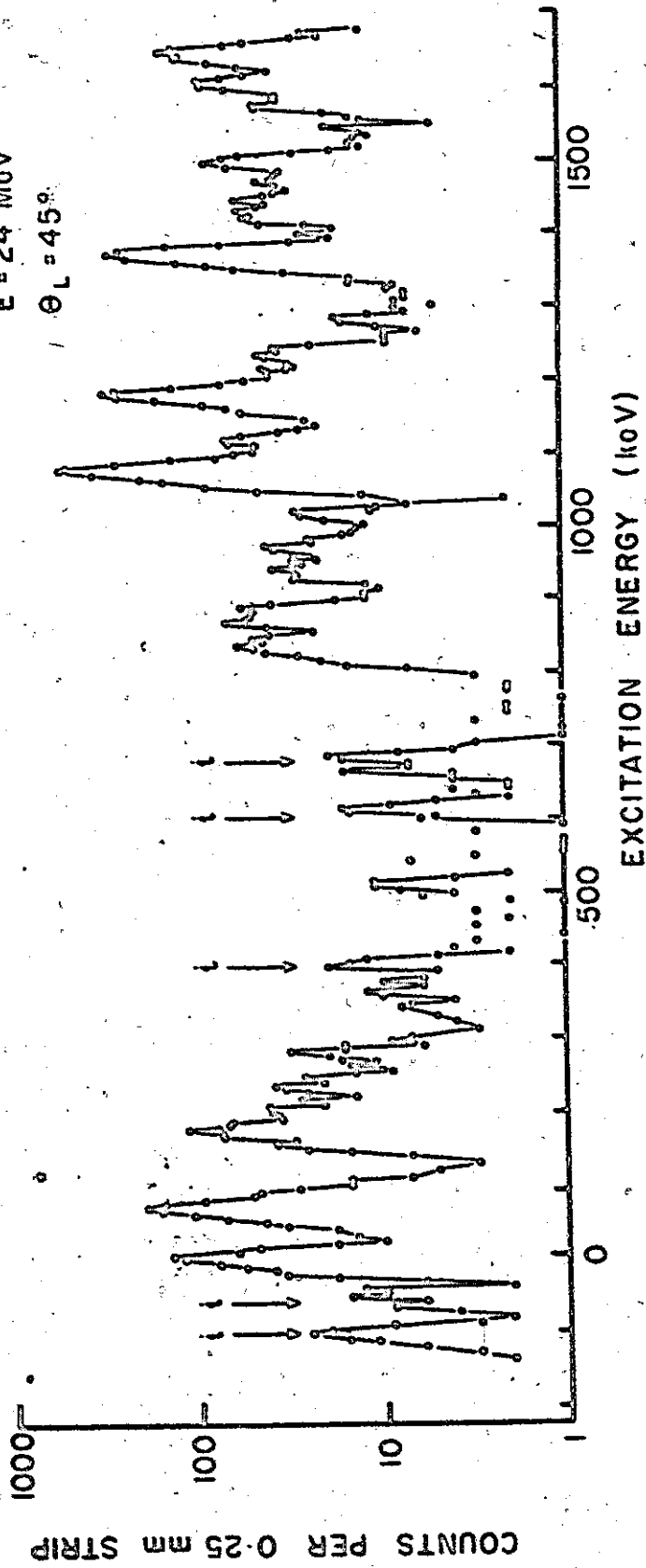
The initial investigation of the $^{143}\text{Nd}(^3\text{He},d)^{144}\text{Pm}$ reaction,

was undertaken to establish the energy levels of ^{144}Pm . The highest available beam energy of 24 MeV was chosen to ensure that both incident and outgoing particles had energies well above their respective Coulomb barriers of ~ 9 MeV and ~ 18 MeV. The reaction Q value was known to be $-0.909(58)$ MeV from Maples et al. (1966), although modified to $-0.830(40)$ MeV, following the most recent atomic mass evaluation (Gove and Wapstra 1972). The outgoing deuterons were detected by photographic plates which were covered with aluminum foil 0.025" thick to prevent particles from other reactions from reaching the emulsion. In particular, triton groups from the competing $^{143}\text{Nd}(^3\text{He},t)^{143}\text{Pm}$ reaction have magnetic rigidities which are comparable to those of the deuterons.

Exposures were made at 30° and 45° , where the $(^3\text{He},d)$ reactions on carbon and oxygen cause no interference, and where DWBA calculations predicted maxima in the angular distributions for $l=2$ and 4 transfers. Both spectra exhibited similar features, the energy resolution being typically 17 keV. The 45° spectrum, shown in Fig. 2.4, was accumulated in 8 hours with a beam current of ~ 0.4 μA . The positions of several peaks, indicated in the figure, are consistent with the $^{144}\text{Nd}(^3\text{He},d)^{145}\text{Pm}$ reaction. An enriched target of ^{144}Nd was used under identical conditions to confirm the assignment. A subsequent exposure with an enriched ^{142}Nd target revealed additional impurity states from the $^{142}\text{Nd}(^3\text{He},d)^{143}\text{Pm}$ reaction. These exposures provided the level schemes of ^{143}Pm and ^{145}Pm (hitherto not well known) and are discussed in Appendix 1.

Fig. 2.4
Deuteron spectrum from the $^{143}\text{Nd}(^3\text{He},d)^{144}\text{Pm}$
reaction. $\dot{\bar{c}}$ denotes peak from impurity reaction.

$^{143}\text{Nd}(^3\text{He},d)^{144}\text{Pm}$
 $E = 24 \text{ MeV}$
 $\theta_L = 45^\circ$



It is evident from Fig. 2.4, that improved energy resolution would be very desirable, especially for the multiplets at ~ 70 keV and ~ 200 keV. Although the $^{143}\text{Nd}(\alpha, t)^{144}\text{Pm}$ reaction, which has a large negative Q value of $-15.150(40)$ MeV, is capable of providing much better energy resolution (~ 10 keV), the cross sections were found to be too small to warrant further study at beam energies of 24 MeV. This can be attributed to the Coulomb barrier which greatly inhibits the outgoing tritons.

2.3b $(^3\text{He}, d)$ Angular Distributions

In order to obtain spectroscopic information about the states in ^{144}Pm , particularly the low lying levels, deuteron angular distributions were measured for the $^{143}\text{Nd}(^3\text{He}, d)^{144}\text{Pm}$ reaction. Spectra were recorded at lab angles ranging from 10° to 60° with a beam energy of 24 MeV. Peak positions and intensities were extracted using SPECTR and checked with hand calculations, to obtain the differential cross sections in the manner already outlined in section 2.2c. The solid angle, subtended by the monitor counter at 30° , was sufficiently small (3.31×10^{-2} mstr) that the elastic peak areas did not require correction for analyzer dead time. The peak areas were, however, corrected for the presence of thorium and the isotopic impurities since the monitor resolution was not sufficient to distinguish their elastic peaks.

The observed angular distributions were compared with those obtained from DWBA calculations using DWUCK. The appropriate optical model parameters, listed in Table 2.2, are taken from the work of Iohimatsu et al. (1969) who measured angular distributions in the

Table 2.2
Optical Model Parameters for the $^{143}\text{Nd}(^3\text{He},d)^{144}\text{Pm}$ Reaction

Particle	V (MeV)	r_{oc} (fm)	r_o (fm)	a (fm)	W_S (MeV)	W_D (MeV)	r'_o (fm)	a' (fm)	V_{SO} factor	Non-local Correction Parameter
^3He	-172.0	1.40	1.14	0.70	-16.0	0	1.54	0.80	0	0.25
d	-101.4	1.30	1.085	0.857	0	61.0	1.29	0.788	0	0.54
p	Adjusted to reproduce separation energy	1.20	1.20	0.65	0	0	0	0	8.0	0.85

$U(r) = U_c(r) + V(e^{x'} + 1)^{-1} + iW_S(e^{x'} + 1)^{-1} + iW_D \frac{d}{dx'} (e^{x'} + 1)^{-1}$, where

$x = (r - r_o \Lambda^{1/3})/a$ and $x' = (r - r'_o \Lambda^{1/3})/a'$. $U_c(x)$ corresponds to the potential due

to a uniformly charged sphere, radius $r_{oc} \Lambda^{1/3}$, charge $Z_A e$.

Finite range correction parameter = 0.770.

No radial cut-off was employed.

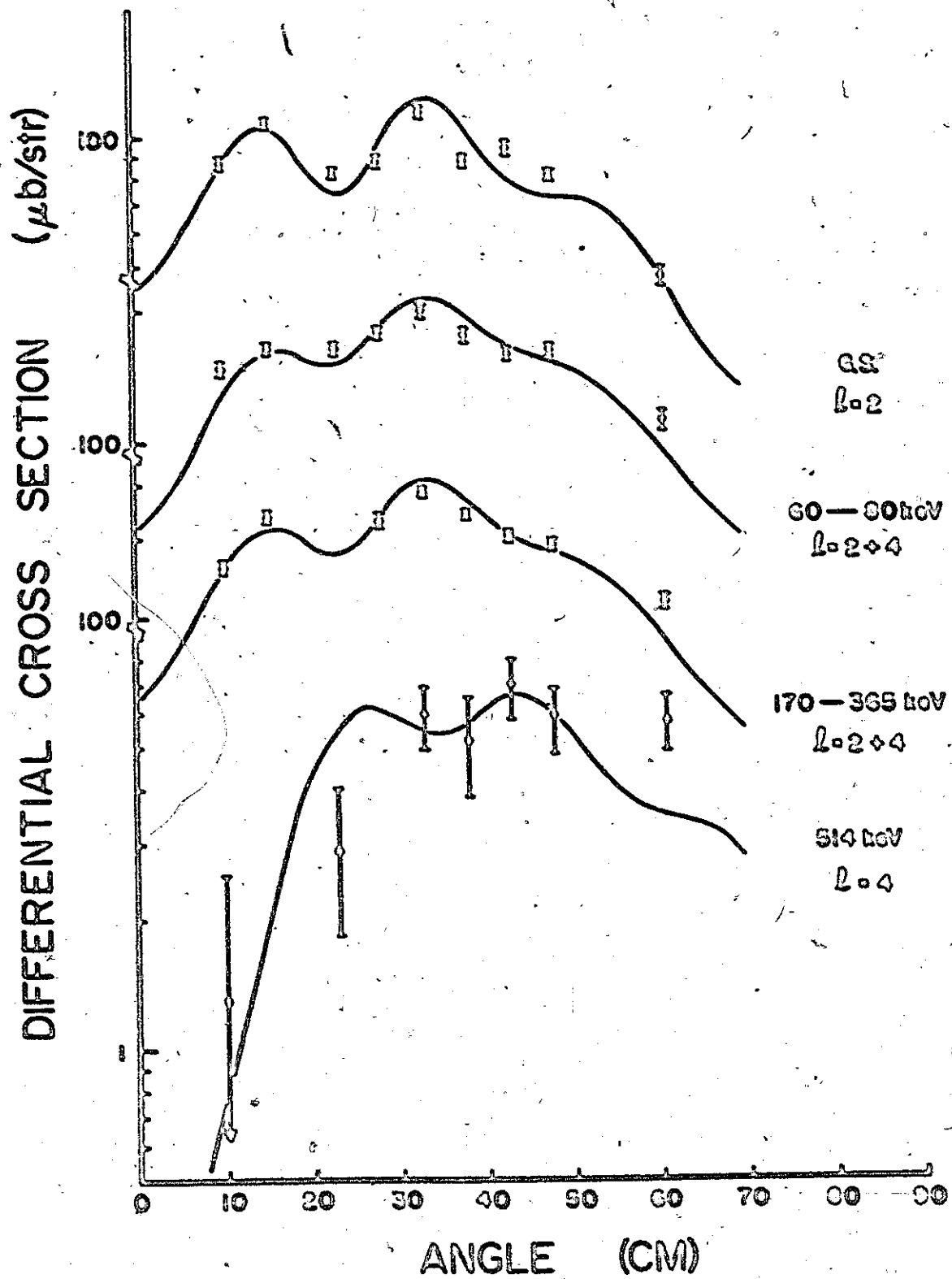
$^3\text{He}, d$ reactions on ^{140}Ce and ^{142}Nd , at a beam energy of 27.3 MeV.

Since several levels were not adequately resolved, angular distributions are given in Fig. 2.5 for groups of levels, as well as individual levels. The identification of the contributing l values, and determination of the relative intensities should be straightforward because of the characteristic shape differences of the $l=2$ and $l=4$ stripping patterns. However, the identification is complicated by the fact that the predicted single particle cross sections for $l=2$ are typically 9 times those for $l=4$. Hence for mixed $l=2$ and 4 transfers, even a small $l=2$ admixture would dominate the angular distribution. This is evident from the figure, where states from 172 keV to 280 keV are best fitted by a 40% $l=2$ component and a 60% $l=4$ component, but the angular distribution has essentially the same shape as that for the ground state which is consistent with pure $l=2$. Angular distributions, fitted by mixed $l=2$ and 4 transfers, could probably be fitted equally well with pure $l=2$ transfers, calculated with a slightly different choice of optical model parameters.

Since the angular distributions for the low lying $5/2^+$ and $7/2^+$ states in ^{143}Pm and ^{145}Pm should be populated by pure $l=2$ and 4 transfers respectively, one approach would involve an accurate measurement of the cross sections and angular distributions of these states, at the same beam energy, which could be used instead of those calculated from DWBA theory. The shapes of the angular distributions could also be interpolated (extrapolated) to account for the Q value

Fig. 2.5

Experimental deuteron angular distributions from the $^{143}\text{Nd}(^3\text{He},d)^{144}\text{Pm}$ reaction. The solid curves given by DWBA calculations, represent pure ℓ transfers and mixed ℓ transfers least-squares-fitted to the data.



dependence. Such an approach would be very time consuming and would minimise only some of the problems.

In the case of the higher excited states of ^{144}Pm , ($^3\text{He},d$) angular distributions were measured for multiplets of levels. At forward angles ($<20^\circ$), however, their small cross sections could not be reliably extracted from troublesome background. The angular distributions at larger angles indicated the presence of l values other than 2 and 4. The most satisfactory approach to study the observed states in ^{144}Pm was found from a combined study of the $^{143}\text{Nd}(^3\text{He},d)^{144}\text{Pm}$ and $^{143}\text{Nd}(\alpha,t)^{144}\text{Pm}$ reactions, discussed in the following sections.

2.3c. The $^{143}\text{Nd}(\alpha,t)^{144}\text{Pm}$ Reaction

Although the $^{143}\text{Nd}(\alpha,t)^{144}\text{Pm}$ reaction was not feasible at a beam energy of 24 MeV, subsequent modifications to the accelerator (installation of a more powerful belt drive motor and an increase in SF_6 pressure) enabled terminal voltages up to 9 MV to be attained. It was felt that the reaction cross section would be significantly greater at 27 MeV since the outgoing tritons would have energies in excess of the Coulomb barrier. Thus, exposures were made at spectrograph angles of 30° and 50° . The photographic emulsions were covered with 0.004" aluminum foil which stopped the elastically scattered α particles. A beam current of $\sim 1.5 \mu\text{A}$ was maintained for more than 13 hours to give the 50° spectrum shown in Fig. 2.6.

The much improved energy resolution (~ 10 keV FWHM) revealed states in both exposures which were previously unresolved in the $^{143}\text{Nd}(^3\text{He},d)^{144}\text{Pm}$ reaction. By exposing targets of natural Nd, and

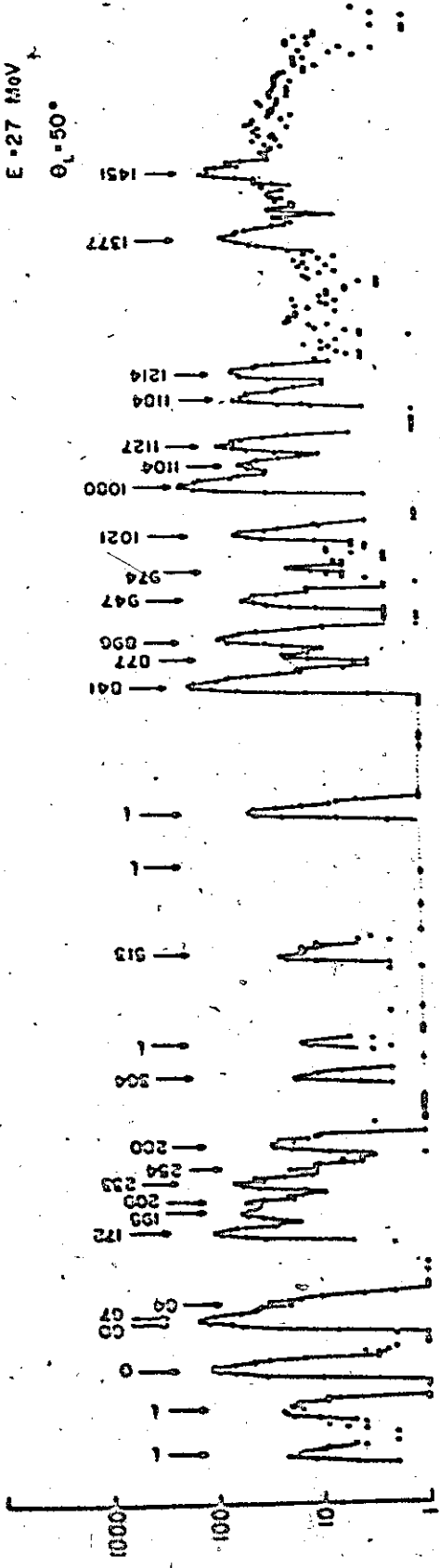
Fig. 2.6

Triton and deuteron spectra from the (α, t) and $({}^3\text{He}, d)$ reactions are shown for comparison.

$^{143}\text{Nd}(\alpha, n)^{142}\text{Pm}$

$E = 27 \text{ MeV}$

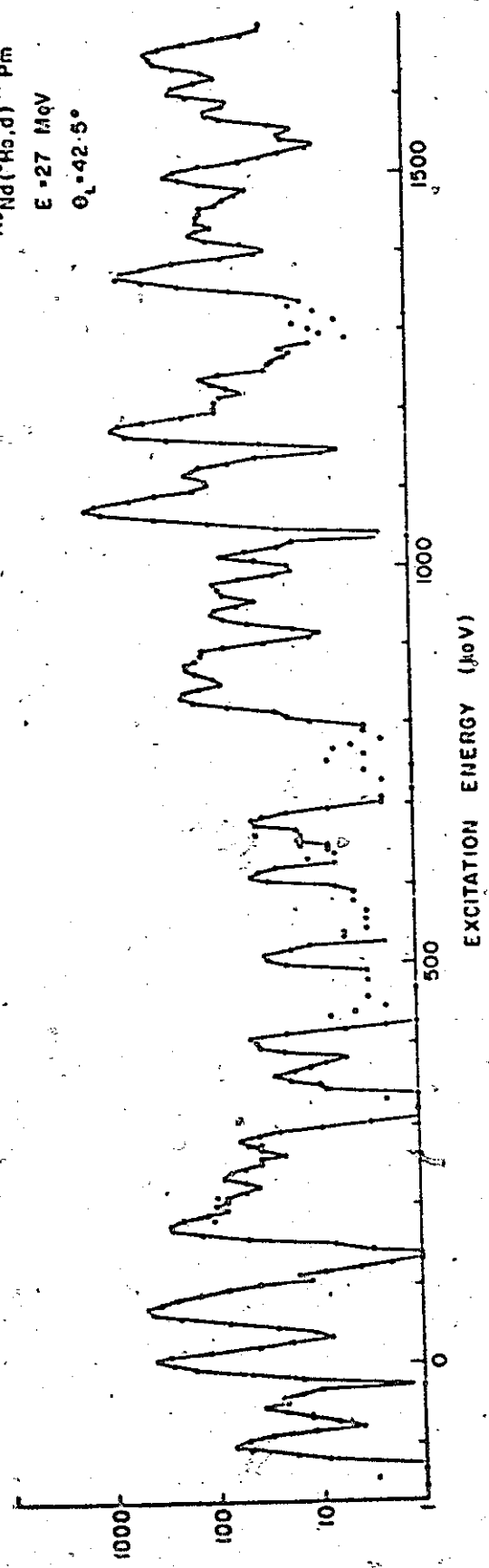
$\theta_L = 50^\circ$



$^{143}\text{Nd}(\text{He}, n)^{142}\text{Pm}$

$E = 27 \text{ MeV}$

$\theta_L = 42.5^\circ$



COUNTS PER 0.25 M STRIP

EXCITATION ENERGY (μeV)

enriched ^{142}Nd and ^{144}Nd , it was confirmed that they corresponded to levels in ^{144}Pm . Due to the small reaction cross section, (α, t) angular distributions were not measured. Furthermore, since the angular distributions are expected to be very similar in absolute magnitude and shape for many different l values, they would not prove very fruitful. In Table 2.3 the (α, t) cross sections are compared with the $(^3\text{He}, d)$ cross sections, which were also measured at 27 MeV. The $(^3\text{He}, d)$ energies represent the average values from the four best resolution exposures at 24 and 27 MeV, while the (α, t) energies are taken from one of the 27 MeV^a exposures with good statistics. The quoted errors, which are somewhat greater than those predicted by SPECTR, account for possible systematic errors ($\sim 1/2$ scan), arising in the plate scanning, and produce consistency among the energies from different exposures. Although the error due to the spectrograph calibration was not included the level energies given in Table 2.3 are in good agreement with those deduced from the γ ray studies described in Chapter III.

2.3d $(^3\text{He}, d)/(\alpha, t)$ Cross Section Ratios

For each l transfer, the $(^3\text{He}, d)/(\alpha, t)$ cross section ratio depends on the reaction Q value, for a given choice of beam energies and angles. Since this ratio should be predicted by DWBA theory, the $(^3\text{He}, d)$ and (α, t) cross sections for different l values were calculated for a series of Q values in the range of interest. Although

^a An elastic exposure taken at the end of the (α, t) runs showed that the beam energy was actually 27.13 MeV.

Table 2.3

Energies and cross sections for levels observed in the

 $^{143}\text{Nd}(^3\text{He},d)^{144}\text{Pm}$ and $^{143}\text{Nd}(\alpha,t)^{144}\text{Pm}$ reactions

Excitation Energy (keV)		Differential Cross Section ($\mu\text{b}/\text{str}$)	
$(^3\text{He},d)$	(α,t)	$(^3\text{He},d)$ $\theta_L = 42.5^\circ$	(α,t) $\theta_L = 50.0^\circ$
0	0	150(9)	24(1)
64(2)	{ 60(2) 67(2)	198(10)	{ 15(4) 18(4)
81(4)	84(3)	50(7)	5.2(6)
172(2)	172(1)	118(6)	20(1)
191(5)	195(1)	21(5)	11(1)
206(3)	209(1)	29(4)	7.8(8)
235(3)	233(1)	30(2)	12(1)
253(4)	252(2)	11(2)	2.5(4)
280(3)	280(1)	22(2)	6.5(5)
364(3)	364(1)	11(1)	2.6(4)
516(3)	513(1)	14(1)	5.4(5)
845(3)	841(1)	90(4)	33(1)
878(3)	877(1)	71(6)	3.5(4)
898(3)	896(1)	47(6)	16(1)
949(3)	947(2)	19(3)	6(2)
982(3)	974(3)	41(3)	1.3(6)
1024(4)	1021(1)	21(4)	10(1)
1085(3)	1080(1)	561(60)	38(1)
	1104(1)		10(1)
1128(3)	1127(1)	75(10)	15(1)
1184(2)	1184(1)	296(30)	11(1)
1217(4)	1214(1)	29(7)	13(1)
1278(4)	1275(2)	7(1)	3.2(6)

Table 2.3 (continued)

Excitation Energy (keV)		Differential Cross Section ($\mu\text{b}/\text{str}$)	
$(^3\text{He},d)$	(α,t)	$(^3\text{He},d)$ $\theta_L = 42.5^\circ$	(α,t) $\theta_L = 50.0^\circ$
1377(2)		293(15)	Cross sections not extracted due to high background.
1428(3)		54(7)	
1451(6)		40(20)	
1471(6)		26(20)	
1502(2)		99(6)	
1543(6)		6(2)	
1609(3)		85(7)	
1645(3)		147(30)	

Statistical errors only are quoted for the differential cross sections.

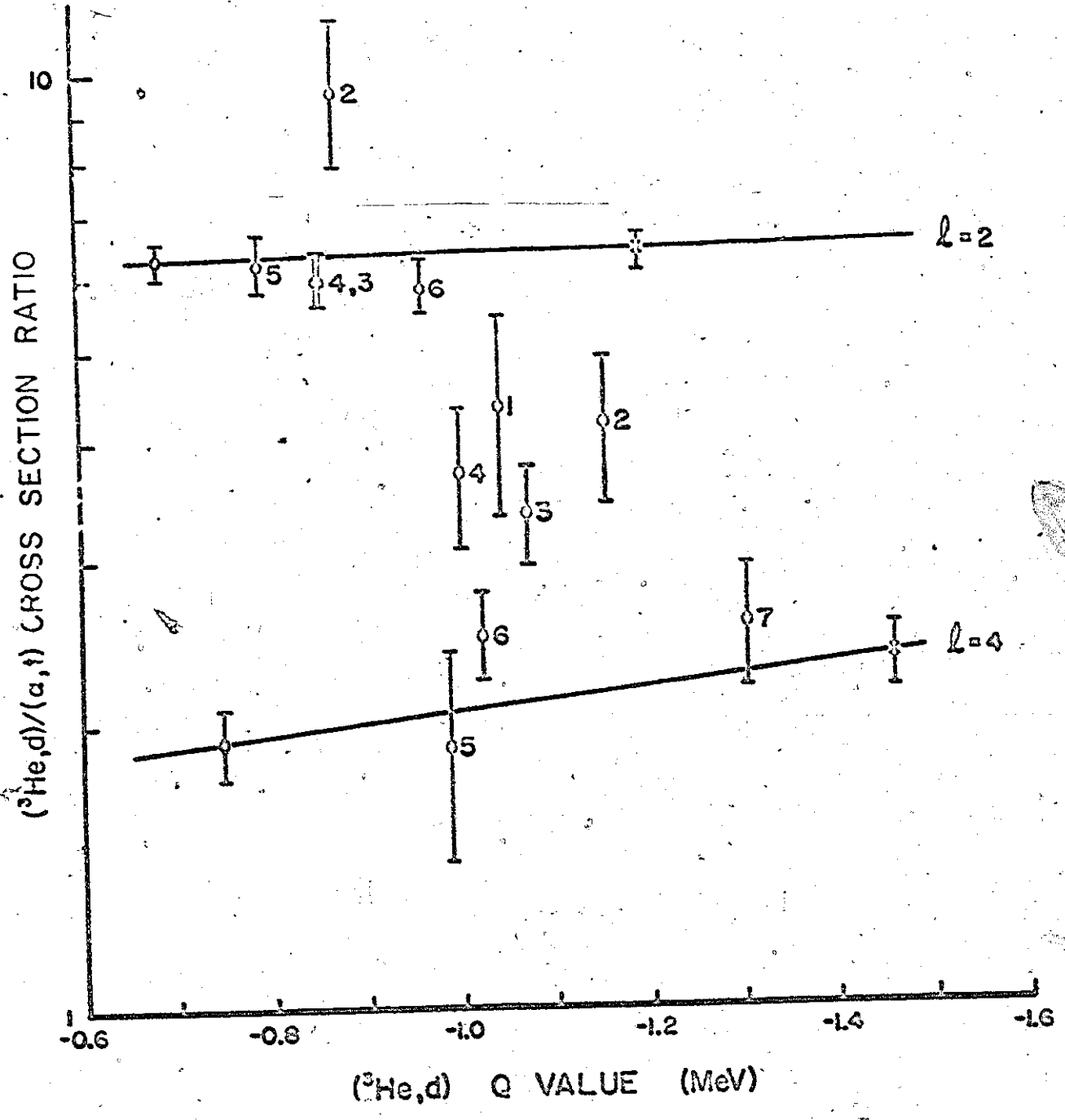
Systematic errors, estimated to be 10%, are thus not included.

the parameters of Ishimatsu et al. (1969) are suitable for the ($^3\text{He},d$) reaction, the choice of (α,t) parameters is less obvious, due to the lack of appropriate experimental data. Calculations were performed using combinations of α parameters from McFadden and Satchler (1966), and Lu and Alford (1971), together with triton parameters from Hafele et al. (1967), Flynn et al. (1969), and Lu and Alford (1971). The computed cross sections showed considerable variations for different sets of parameters, the absolute magnitudes differing by more than a factor of 2.

To overcome this difficulty, the ratios of the ($^3\text{He},d$) and (α,t) cross sections were measured experimentally for the $5/2^+$ and $7/2^+$ low lying levels in ^{143}Pm and ^{145}Pm . In ^{143}Pm these states contain essentially all the $2d_{5/2}$ and $1g_{7/2}$ proton transfer strength (Wildenthal 1971). It is assumed that the $5/2^+$ ground state and $7/2^+$ first excited state at 61 keV in ^{145}Pm are also populated by all the available $2d_{5/2}$ and $1g_{7/2}$ strength. (From Appendix 1, the other states which are strongly populated in ^{145}Pm occur at excitations >700 keV.) Enriched targets of ^{142}Nd and ^{144}Nd were exposed under the same experimental conditions employed for the proton transfer reactions to ^{144}Pm . In this way, the cross sections measured for different reactions are self-consistent, although subject to an absolute uncertainty which is estimated to be approximately 10%. The cross section ratios are shown in Fig. 2.7. The states in ^{144}Pm up to 514 keV are included since they are conveniently enclosed by the $d_{5/2}$ and $g_{7/2}$ configurations in ^{143}Pm and ^{145}Pm . It is evident that most of the states in ^{144}Pm are populated by mixed l values.

Fig. 2.7

$(^3\text{He},d)/(\alpha,t)$ cross section ratios for states in ^{144}Pm plotted as a function of $(^3\text{He},d)$ Q value. The X's and O's indicate the $5/2^+$ ground state and $7/2^+$ first excited states of ^{143}Pm and ^{145}Pm respectively. Lines have been drawn to approximate the dependence for pure ℓ transfers. The error bars denote statistical errors only. The spins of the levels, deduced from the γ ray work of Chapter III, are also given.



2.3e Extraction of Spectroscopic Factors

In section 2.1 the differential cross section for a stripping reaction, involving several l transfers, is given by

$$\left(\frac{d\sigma}{d\Omega}\right)^{\text{exp}} = \sum_i \left(\frac{d\sigma}{d\Omega}\right)^{\text{exp}}_{(nlj)_i} = N \frac{(2J_B+1)}{(2J_A+1)} \sum_i S(nlj)_i \left(\frac{d\sigma}{d\Omega}\right)^{\text{DWBA}}_{(nlj)_i}$$

Assuming that the low lying levels of ^{144}Pm arise from only the $2d_{5/2}$ and $1g_{7/2}$ proton configuration and the $2f_{7/2}$ neutron configuration, then this expression becomes

$$\left(\frac{d\sigma}{d\Omega}\right)^{\text{exp}}_{J_B} = N \frac{(2J_B+1)}{8} \left[\alpha_{J_B}^2 \left(\frac{d\sigma}{d\Omega}\right)^{\text{DWBA}}_{2d_{5/2}} + \beta_{J_B}^2 \left(\frac{d\sigma}{d\Omega}\right)^{\text{DWBA}}_{1g_{7/2}} \right] \quad 2.2$$

where $\alpha_{2d_{5/2}}^2 + \beta_{1g_{7/2}}^2 = 1$ from normalization requirements. For the $5/2^+$ and $7/2^+$ states in ^{143}Pm and ^{145}Pm one assumes

$$\left(\frac{d\sigma}{d\Omega}\right)^{\text{exp}}_{5/2^+} = 6 N \left(\frac{d\sigma}{d\Omega}\right)^{\text{DWBA}}_{2d_{5/2}}, \text{ and}$$

$$\left(\frac{d\sigma}{d\Omega}\right)^{\text{exp}}_{7/2^+} = 8 N \left(\frac{d\sigma}{d\Omega}\right)^{\text{DWBA}}_{1g_{7/2}}$$

If the reaction parameters, such as beam energy and laboratory angle, are the same for the reactions to ^{143}Pm , ^{144}Pm and ^{145}Pm , the DWBA cross sections are dependent on the reaction Q value only. Over a relatively small range of Q values (~ 1 MeV) DWBA calculations indicate that the functional form of the dependence is approximately exponential, so that

$$\left(\frac{d\sigma}{d\Omega}\right)^{\text{exp}}_{nlj} = e^{(a_{nlj}Q + b_{nlj})}, \text{ where } a_{nlj} \text{ and } b_{nlj} \text{ are con-}$$

stands over the Q value range. For the $^{143}\text{Nd}(^3\text{He},d)^{144}\text{Pm}$ reaction equation 2.2 becomes

$$\left(\frac{d\sigma}{d\Omega}\right)^{\text{exp}} = \frac{(2J_B+1)}{8} \left[\frac{1}{6} \alpha_{2d_{5/2}}^2 e^{(a_{2d_{5/2}} Q + b_{2d_{5/2}})} + \frac{1}{8} \beta_{1g_{7/2}}^2 e^{(a_{1g_{7/2}} Q + b_{1g_{7/2}})} \right]. \quad 2.3$$

Similarly for the $^{143}\text{Nd}(\alpha,t)^{144}\text{Pm}$ reaction using primed quantities,

$$\left(\frac{d\sigma}{d\Omega}\right)^{\text{exp}} = \frac{(2J_B+1)}{8} \left[\frac{1}{6} \alpha_{2d_{5/2}}^{\prime 2} e^{(a_{2d_{5/2}}^{\prime} Q + b_{2d_{5/2}}^{\prime})} + \frac{1}{8} \beta_{1g_{7/2}}^{\prime 2} e^{(a_{1g_{7/2}}^{\prime} Q + b_{1g_{7/2}}^{\prime})} \right]. \quad 2.4$$

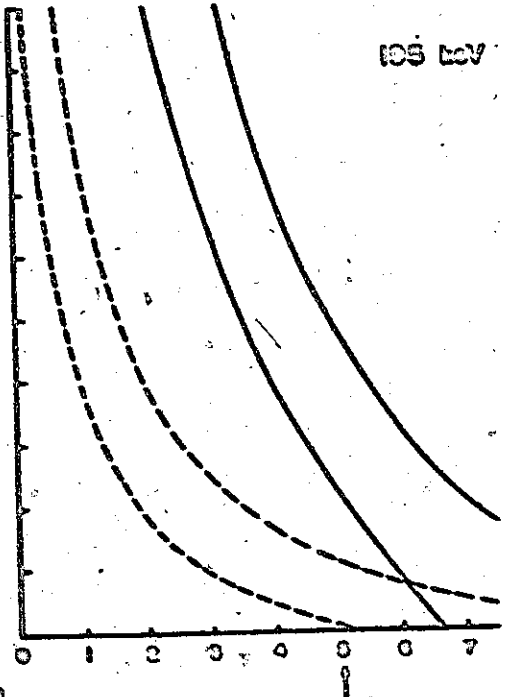
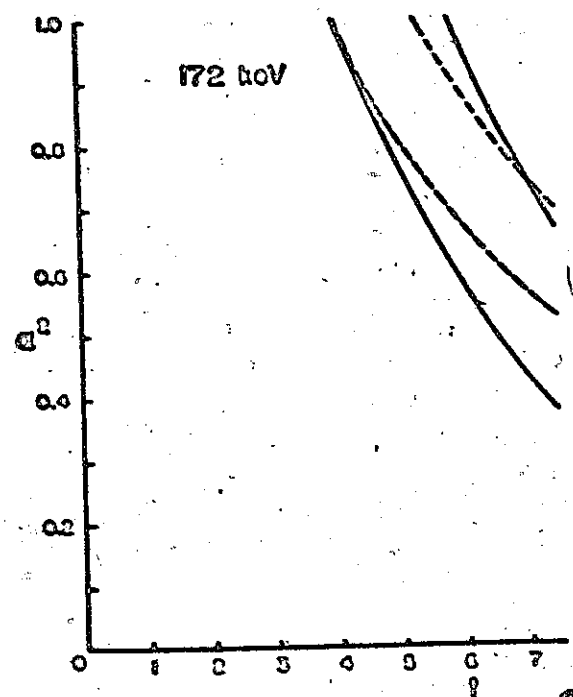
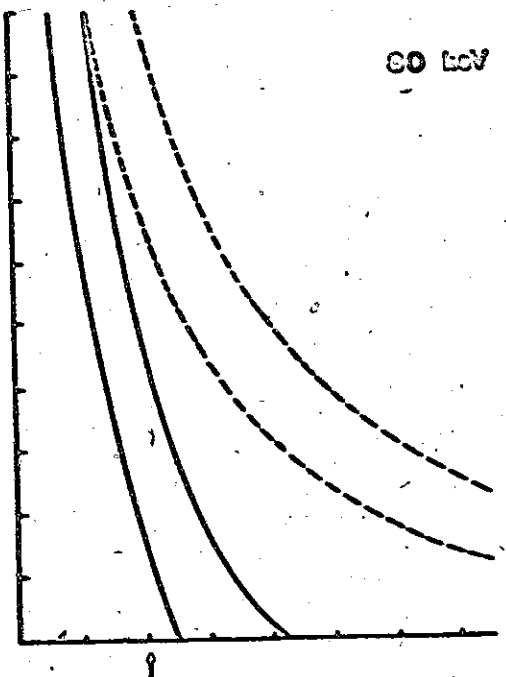
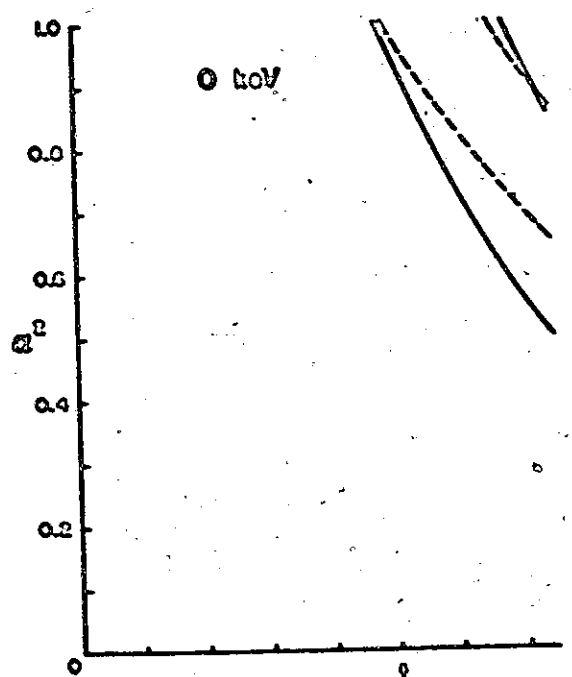
The a, b constants were determined experimentally from the $(^3\text{He},d)$ and (α,t) reactions, leading to ^{143}Pm and ^{145}Pm . Taking the measured $(^3\text{He},d)$ and (α,t) cross sections for ^{144}Pm , equations 2.3 and 2.4 become soluble for J_B and the spectroscopic factors $\alpha_{2d_{5/2}}^2$ and $\beta_{1g_{7/2}}^2$ (set equal to $1 - \alpha_{2d_{5/2}}^2$). For states in ^{144}Pm , the allowed values of the spectroscopic factors, corresponding to different values of J_B , are plotted for the $(^3\text{He},d)$ and (α,t) reactions, as shown in Fig. 2.8. By including the uncertainties in the experimentally measured quantities, one can restrict the values of J_B and the associated spectroscopic factors for each state. The latter are presented in Table 2.4.

This method, which has not previously been employed to extract spins and spectroscopic factors independently, is a useful qualitative approach which is not limited by the uncertainties associated with

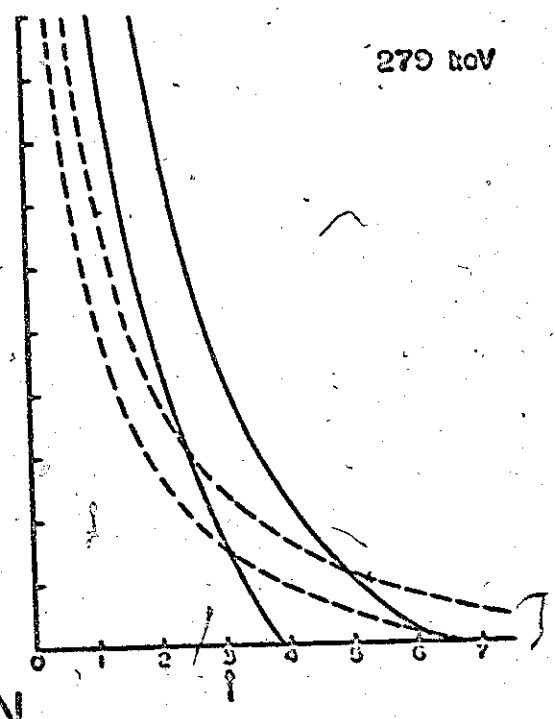
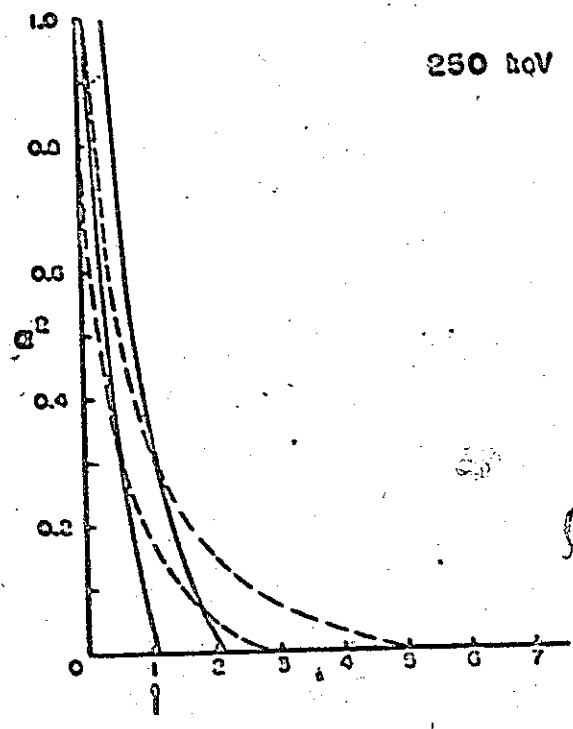
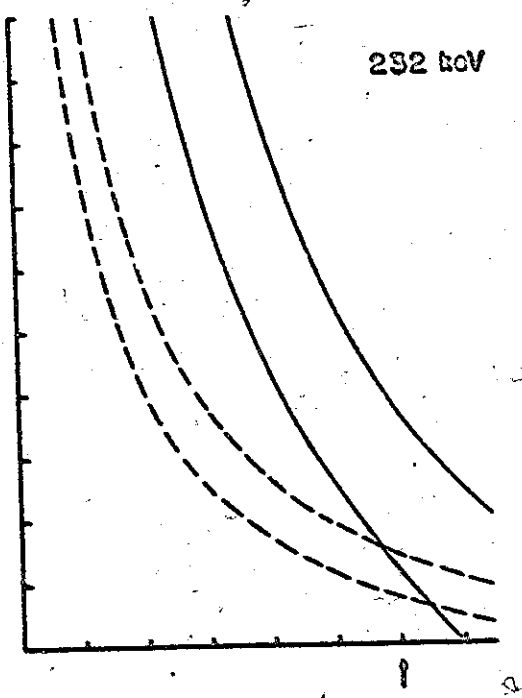
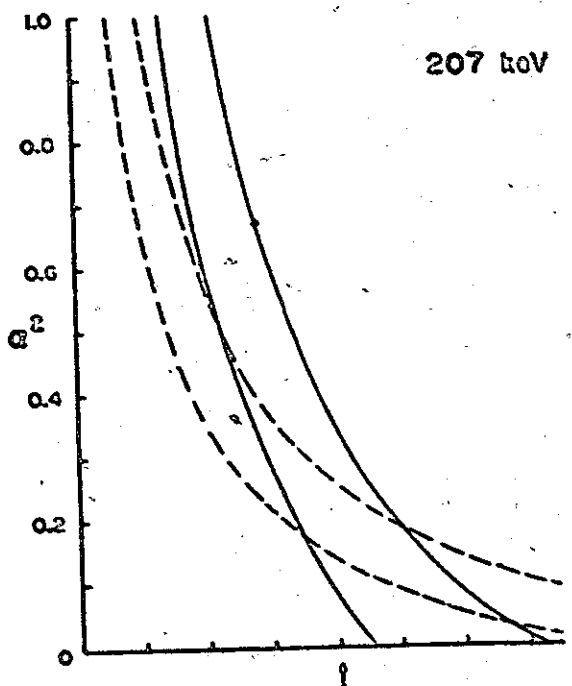
Fig. 2.8

Allowed spectroscopic factors and spins for levels populated in the ($^3\text{He},d$) reaction (dashed curves) and in the (α,t) reaction (solid curves). The pair of lines for each reaction represents extreme solutions, consistent with the experimental uncertainties. Solutions exist where curves overlap. Arrows indicate the spin values deduced from the γ ray studies.

3



SPIN



SPIN

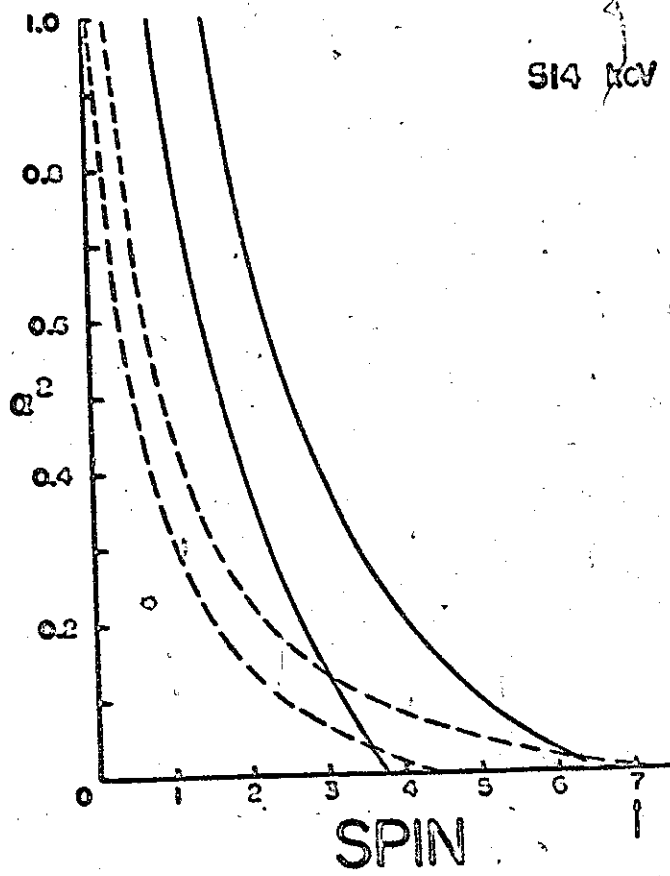
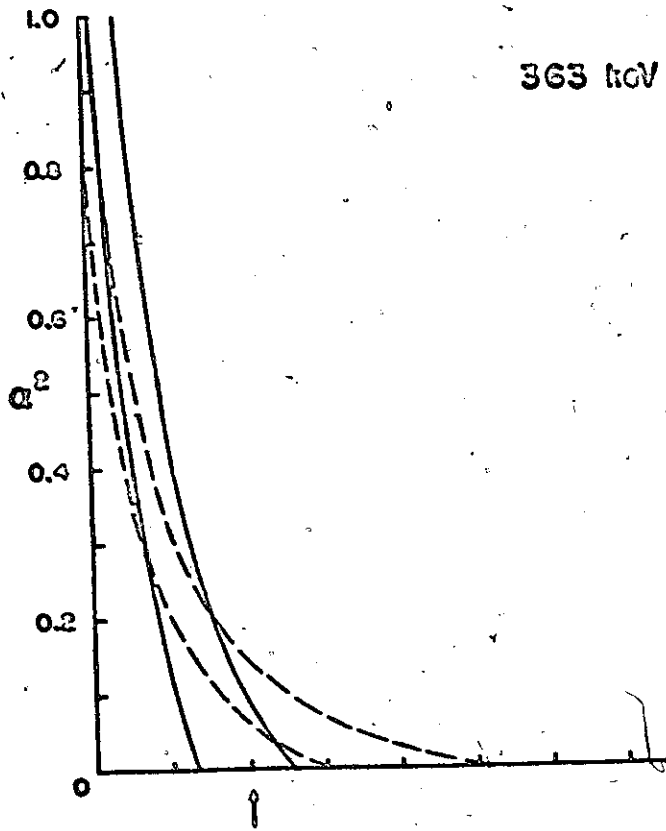


Table 2.4

Spectroscopic Factors for the $^{143}\text{Nd}(^3\text{He},d)^{144}\text{Pm}$ and
 $^{143}\text{Nd}(\alpha,t)^{144}\text{Pm}$ reactions

Energy (keV)	Spin	(Spectroscopic Factor) ^{1/2}	
		a	B
0	5	1.0(1)	0.0(3)
60.7	4	>0.84	<0.55
66.6	3	>0.84	<0.55
80.0	2	>0.84	<0.55
171.8	6	0.87(8)	0.50(13)
195.4	5	0.39(14)	0.92(5)
207.4	4	0.45(11)	0.89(5)
232.4	6	0.36(12)	0.93(5)
249.9	1	0.50(10)	0.87(6)
279.3	3	0.47(10)	0.88(6)
363.3	2	0.26(11)	0.97(3)
514.4	7	<0.22	>0.97

* Extracted from (α,t) reaction assuming spins of these levels.

Energies and spins have been adopted from γ ray studies.

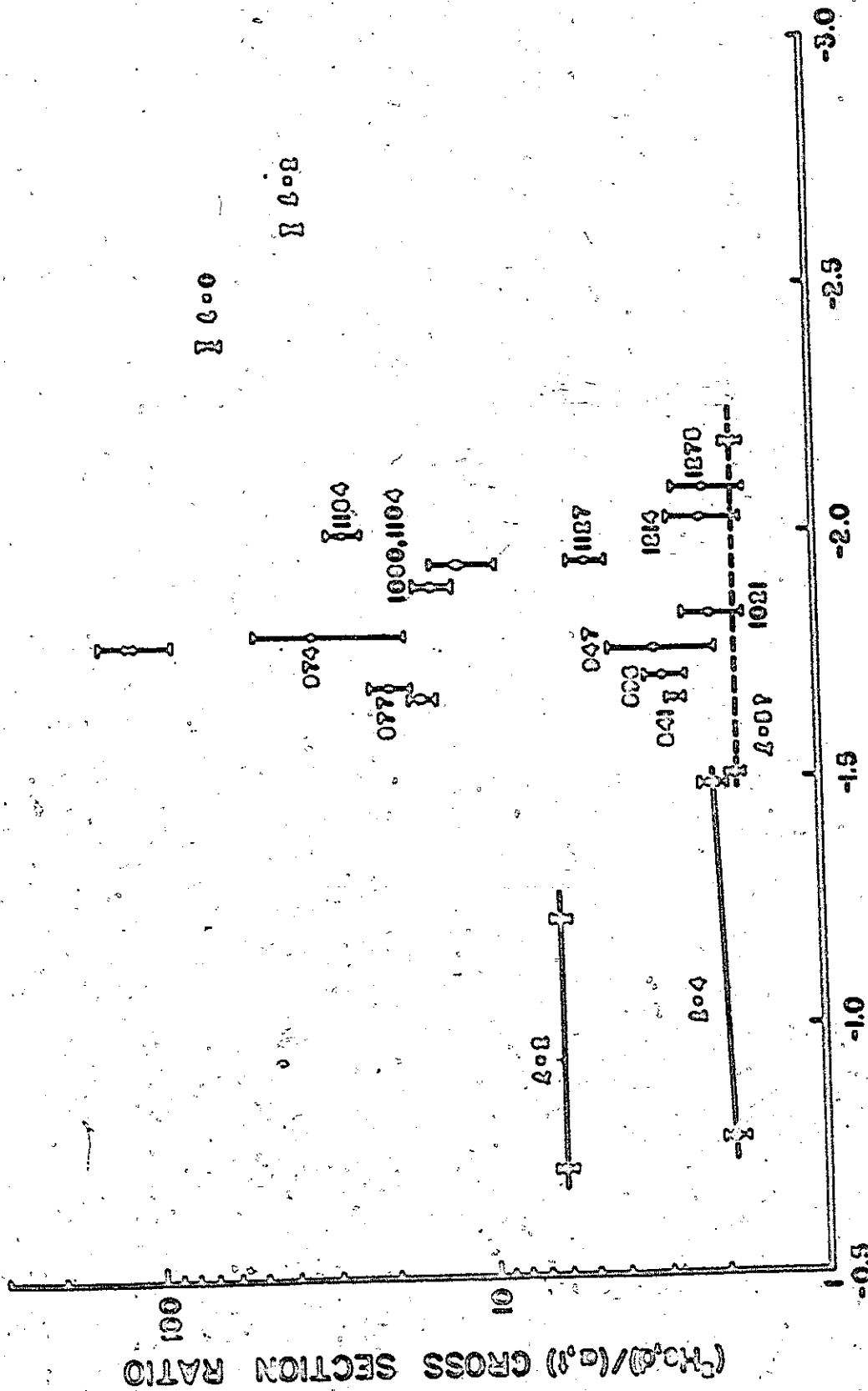
optical model parameters. The approach may thus prove useful in the analysis of both proton and neutron transfer reactions in other regions of the periodic table, especially if combined with angular distribution studies.

Information about the higher excited states has also been extracted from the ($^3\text{He},d$) and (α,t) reactions. The cross section ratios for these levels are shown in Fig. 2.9. Levels beyond 1400 keV could not be identified in the (α,t) reaction on account of the very low cross sections, resulting from Coulomb barrier effects on the outgoing tritons. The experimental cross section ratios for states in ^{143}Pm , and their assigned l values deduced by Wildenthal et al. (1971), are shown for comparison. Also included are the ratios for some of the single particle states in ^{145}Pm , for which l values are given. (The level schemes of ^{143}Pm and ^{145}Pm will be discussed in more detail in Appendix 1.) Although it was not possible to deduce the l and Q value dependences for the ratios in the high energy scheme, it is apparent that the states have both small (<2) and large (>5) l values. Assuming that the ratio for a given l value does not depend strongly on the Q value over this energy range, one may assign $l=4$ or 5 to the states at 841, 896, 947, 1021, 1214 and 1275 keV. For the states at 877, 974, 1080, 1104 and 1184, small l values are favoured. l Values of 5, 2 and 0 would be consistent with those expected from the $1h_{11/2}$, $2d_{3/2}$ and $3s_{1/2}$ shell model orbitals. Since many configurations are present in the high energy scheme it has not been possible to extract l admixtures for these states.

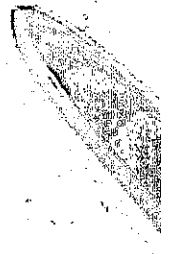
Fig. 2.9

Cross section ratios for high energy levels in ^{144}Pm .

(Excitation energies are given with data. The ratios for states in $^{143}\text{Pm}(X)$ and $^{145}\text{Pm}(0)$ are also shown.



$({}^2\text{Ho},d)$ Q VALUE (MeV)



Chapter III

GAMMA RAY STUDIES

3.1 Introduction

Direct reactions are very selective and this feature is both an asset and a disadvantage in the study of nuclear structure. For example, the ($^3\text{He},d$) reaction leading to ^{144}Pm can only populate states in which the neutron configuration is $2f_{7/2}$, and among them it favours low l values. If one wishes to see the other excited states a different approach is necessary. Compound nucleus reactions, for example, are much less selective and so they are more apt to reveal all the nuclear excited states. By combining the information from a variety of experiments the most complete understanding of a nucleus will be obtained.

Thus, a number of experiments were carried out to investigate the γ rays emitted by the excited states of ^{144}Pm . The $^{141}\text{Pr}(\alpha,n)^{144}\text{Pm}$ and $^{144}\text{Nd}(p,n)^{144}\text{Pm}$ reactions were studied in singles experiments at several different bombarding energies, and also in coincident experiments. These investigations, described in subsequent sections, shed considerable light on the level scheme of ^{144}Pm . The appropriate theoretical aspects of γ ray transitions in nuclei are briefly discussed in the following section.

3.2 Electromagnetic Transitions in Nuclei

The electromagnetic properties of the atomic nucleus arise from the charge and current distributions of the constituent nucleons. The

mathematical details of the theory of radiative transitions have been well documented (eg. de Shalit and Talmi 1963, Yoshida and Zammick 1972), so that only the relevant results are given here.

The transition probability for emission of a photon of energy $\hbar\omega$, multipolarity λ and of electric ($a=E$), or magnetic ($a=M$) character, from the state $|i\rangle$ to state $|f\rangle$, is

$$T_{if}(\lambda, a) = \frac{8\pi(\lambda+1)}{\lambda[(2\lambda+1)!!]^2} \frac{1}{\hbar} \left(\frac{\omega}{c}\right)^{2\lambda+1} |\langle f | \Omega_{\lambda\mu} | i \rangle|^2,$$

in the limit when (c/ω) is much greater than the nuclear dimensions. Here $\Omega_{\lambda\mu}$ stands for the electric ($Q_{\lambda\mu}$), or magnetic ($M_{\lambda\mu}$) multipole operator. Since the orientation of the initial and final states are usually not known, a sum is performed over the magnetic quantum numbers (M_f) of the final states, and an average taken over the magnetic quantum numbers (M_i) of the initial state.

The so-called reduced transition probability is then defined

$$B_{if}(a, \lambda) = \frac{1}{(2J_i+1)} \sum_{M_i, M_f, \mu} |\langle J_f M_f | \Omega_{\lambda\mu} | J_i M_i \rangle|^2.$$

Using the Wigner-Eckhart theorem to write

$$\langle J_f M_f | \Omega_{\lambda\mu} | J_i M_i \rangle = \langle J_f M_f | \Omega_{\lambda\mu} | J_f M_f \rangle \langle J_f || \Omega_{\lambda} || J_i \rangle \quad 3.1$$

gives
$$B_{if}(a, \lambda) = \frac{2J_f+1}{2J_i+1} |\langle J_f || \Omega_{\lambda} || J_i \rangle|^2,$$

where $\langle J_f || \Omega_{\lambda} || J_i \rangle$ is a reduced matrix element which does not depend on the magnetic substates involved. It is this factor which contains the details of the structure of the initial and final states. The transition probability becomes

$$T_{if}(\lambda, a) = \frac{8\pi(\lambda+1)}{\lambda[(2\lambda+1)!!]^2} \frac{1}{\hbar} \left(\frac{\omega}{c}\right)^{2\lambda+1} B(a, \lambda).$$

A transition between an initial state J_i , and final state J_f , can involve several electric and magnetic multipoles, which satisfy the relations

$$|J_i - J_f| \leq \lambda \leq |J_i + J_f|, \text{ and also}$$

$$u = M_f - M_i.$$

(These selection rules are contained in the Clebsch Gordan coefficient occurring in equation 3.1.) Conservation of parity imposes additional selection rules viz. $\pi_i \pi_f = \begin{cases} (-1)^\lambda & \text{for electric transitions} \\ (-1)^{\lambda+1} & \text{for magnetic transitions} \end{cases}$. In most cases, only the lowest allowed multipole of each type has to be considered.

Using the electromagnetic operators $Q_{\lambda\mu}$ and $M_{\lambda\mu}$, the reduced matrix elements for given transitions may be calculated within the framework of a given model. A comparison of the theoretical and experimental transition rates, or related branching ratios, thus serves as a sensitive test of the model wavefunctions. In evaluating the reduced matrix elements, model dependent selection rules may also arise to impose further restrictions on the allowed transitions. For example, the ground states and first excited states of the N=82 odd proton nuclei have been classified as $1g_{7/2}$ and $2d_{5/2}$ in terms of the shell model. The expected M1 transitions between these states are of the Δl -forbidden type, and experimentally are greatly retarded (Backlin and Malmskog 1967). In the odd-odd N=83 nuclei however, because the states involve a mixture of these two configurations, M1 transitions

are no longer forbidden. By making order of magnitude assumptions to evaluate the reduced matrix elements $B_{if}(a, \lambda)$, one can obtain Weisskopf or "single particle" estimates for the M1 and the competing E2 transition rates. For γ ray transitions of less than 1 MeV the M1 transition rate is >500 times the E2 transition rate, and so M1 transitions are expected to be the dominant mode of decay.

3.3 Gamma Ray Singles Studies

3.3a Experimental Outline

To investigate the γ decay properties of the excited states of ^{144}Pm , $^{141}\text{Pr}(\alpha, n)^{144}\text{Pm}$ and $^{144}\text{Nd}(p, n)^{144}\text{Pm}$ experiments were undertaken using Ge(Li) detectors. Pulses from the detectors were shaped and amplified by Ortec preamplifiers coupled to Tennelec TC203 main amplifiers and base line restorers. The pulse height analysis and data storage were accomplished with Nuclear Data analogue-to-digital convertors (ADC's), interfaced to a Nuclear Data 3300 analyzer. The resultant 4096 Channel spectra were recorded on magnetic tape, and subsequently analyzed by means of the computer program JAGSPOT (Williams and McPherson 1968). The program performs a least squares fit to the data using a function of the form

$$I(x) = a + bx + \sum_{j=1}^N \gamma_j \int_{-\infty}^{x-p_j} e^{-(y-x-p_j)} e^{-\delta(x-y)^2} dy,$$

where x = channel number

$I(x)$ = number of counts in channel x

N = number of peaks in region being considered (<6)

$a + bx$ = linear background term

γ_j = intensity of peak located at x_{pj}

δ, ϵ = width and skewness parameters of peak.

To measure γ ray energies the Ge(Li) detectors were placed at 90° to the beam direction, thus minimising the effects of Doppler broadening. The standard sources used for the energy calibrations are listed in Table 3.1. On the other hand, the relative intensities were measured at 125° to the beam direction so that angular distribution effects could be safely ignored. Detector efficiencies, as a function of γ ray energy, were determined at the end of each experiment, in the reaction geometry, using a set of absolutely calibrated IAEA sources, supplemented by sources of ^{182}Ta (White 1970) and ^{152}Eu (Aubin 1969), which have many lines of well known relative intensities. The sources were placed in the target chamber at the same location as the beam spot on the target, thus maintaining the same γ ray absorption in the walls of the target chamber, and in the Mo-Cu absorbers, used with the detectors to absorb low energy radiation. The γ ray intensities measured in the (α, n) and (p, n) experiments were corrected for absorption in the targets as outlined in Appendix 3.

3.3b γ Ray Singles Experiments

The singles experiments were carried out using 16.5 MeV α beam incident on thick targets of Pr (chemical purity $\geq 99.5\%$). At this bombarding energy even the high spin states of interest are expected to be populated relatively strongly. The targets were mounted on an aluminum holder in a target chamber consisting of a

Table 3.1
 γ Ray Energy Standards

Source	Energy (keV)	Error in Energy (eV)	
^{241}Am	59.537	1	} Greenwood et al. 1970
^{182}Ta	100.105	1	
^{57}Co	122.061	10	
^{57}Co	136.471	10	
^{141}Ce	145.440	3	
^{182}Ta	152.434	2	
^{182}Ta	156.387	2	
^{182}Ta	179.393	3	
^{182}Ta	222.110	3	
^{182}Ta	229.322	6	
^{182}Ta	264.072	6	
^{203}Hg	279.188	6	
^{192}Ir	308.445	7	
^{192}Ir	316.497	7	
^{207}Bi	569.630	13	} Helmer et al. 1971
^{137}Cs	661.638	19	
^{54}Mn	834.827	21	
^{88}Y	898.021	19	
^{207}Bi	1063.580	24	
^{60}Co	1173.208	25	} Gunnink et al. 1968
^{60}Co	1332.505	25	
^{207}Bi	1770.060	70	} Brahmavar and Hamilton 1969

0.43" diameter pyrex tube with 0.060" thick walls. A description of this apparatus is given elsewhere (Dohan 1972). Such a chamber minimised the absorption of low energy γ rays from the reaction and also allowed the Ge(Li) detectors to be placed close to the target. A study of the $^{144}\text{Nd}(p,n)^{144}\text{Pm}$ reaction was also undertaken at a bombarding energy of 10 MeV, to lend further support to the assignment of γ rays. The targets for the (p,n) experiments consisted of enriched $^{144}\text{Nd}_2\text{O}_3$ powder, mounted on a carbon holder with a glue prepared from benzene and polystyrene. The enriched oxide had the same isotopic composition as that used for the particle studies (Table 2.1). The beam energies were chosen so as to maximise the yields from the (α,n) and (p,n) reactions, and avoid interference from the $(\alpha,2n)$ and (p,2n) reactions, which have respective Q values of -16.8 MeV and -9.8 MeV.

Although the first (α,n) and (p,n) experiments, performed with a 37 cm^3 (4.4 keV FWHM at 1.33 MeV) Ge(Li) detector, revealed many lines in common, the energies of some of the strong low energy lines were not in agreement. Since it was therefore desirable to obtain γ spectra with high energy resolution both the (α,n) and (p,n) reactions were further studied following the acquisition of high quality 0.9 cm^3 and 50 cm^3 detectors. The smaller detector was especially useful for the low energy region (<400 keV) on account of its excellent resolution (650 eV at 122 keV). For the high energy region (>400 keV) the efficiency of this detector decreased very rapidly and consequently the much more efficient 50 cm^3 detector was used although its resolution was poorer (3.0 keV at 1.33 MeV). To avoid overloading the detectors with X rays from the targets, Mo-Cu

absorbers were used, although they were later removed when the X-ray region was investigated. With beam currents of 10nA for the (α,n) reaction and 30nA for the (p,n) reaction spectra were accumulated for 10 hours. Count rates of $\sim 10^4 \text{ sec}^{-1}$ could be tolerated, using amplifier time constants of 1 μsec, without noticeable loss of resolution. Examples of spectra from both reactions, obtained with the smaller detector, are shown in Fig. 3.1, and show many multiplets. In particular the doublets seen at 170 and 281 keV account for earlier discrepancies in γ ray energies. The spectra obtained with the 50 cm³ detector are shown in Fig. 3.2.

It was important to identify the lines arising from other reactions since the γ rays associated with ¹⁴⁴Pm had not previously been studied. The (α,α') reaction on the target produced several lines which were known from previous studies of ¹⁴¹Pr (Daniels and Felsteiner 1968, Dave et al. 1970). Lines were observed from ¹⁹F, ²³Na and ^{16,17,18}O impurities, probably introduced on the target surface during the target preparation, and during the experiment, but other likely impurities were not identified. Also present were lines from Fe (beam pipe), Ta (slits), Pb (shielding) and Au (conducting electrodes of Ge(Li) detector).

Although the isotopic enrichment of ¹⁴⁴Nd in the (p,n) target was >97%, a similarly prepared target of natural Nd₂O₃ was also exposed to the 10 MeV proton beam. From energy and intensity considerations, it was thus possible to identify reactions on other isotopes. In particular, lines at 72.0 keV and 61.25 keV, arising from the (p,p') and (p,n) reactions on ¹⁴⁵Nd would be too weak to be

Fig. 3.1

Ge(Li) spectra (0.9 cm^3) from the (α, n)
and (p,n) reactions

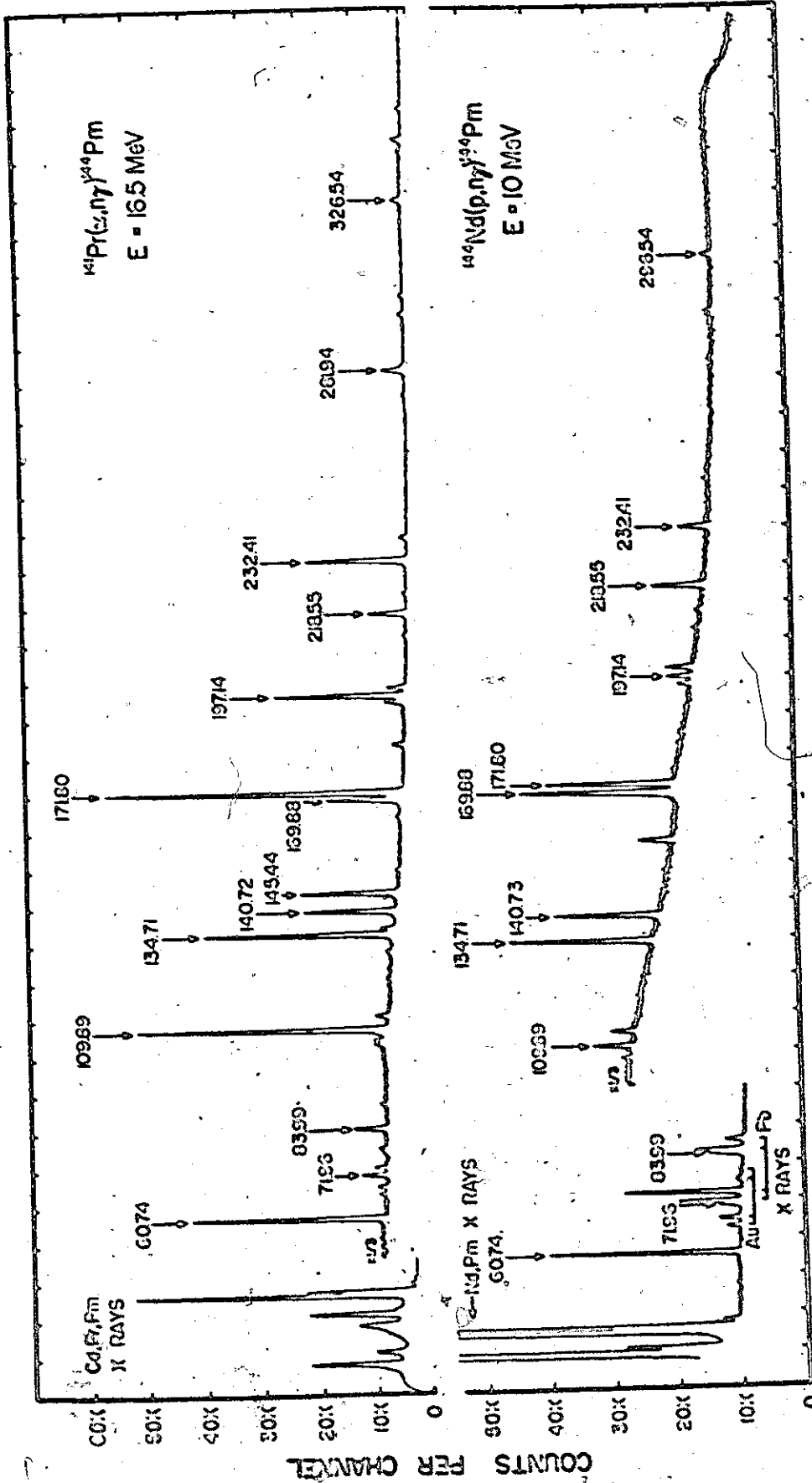
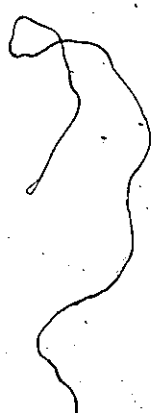
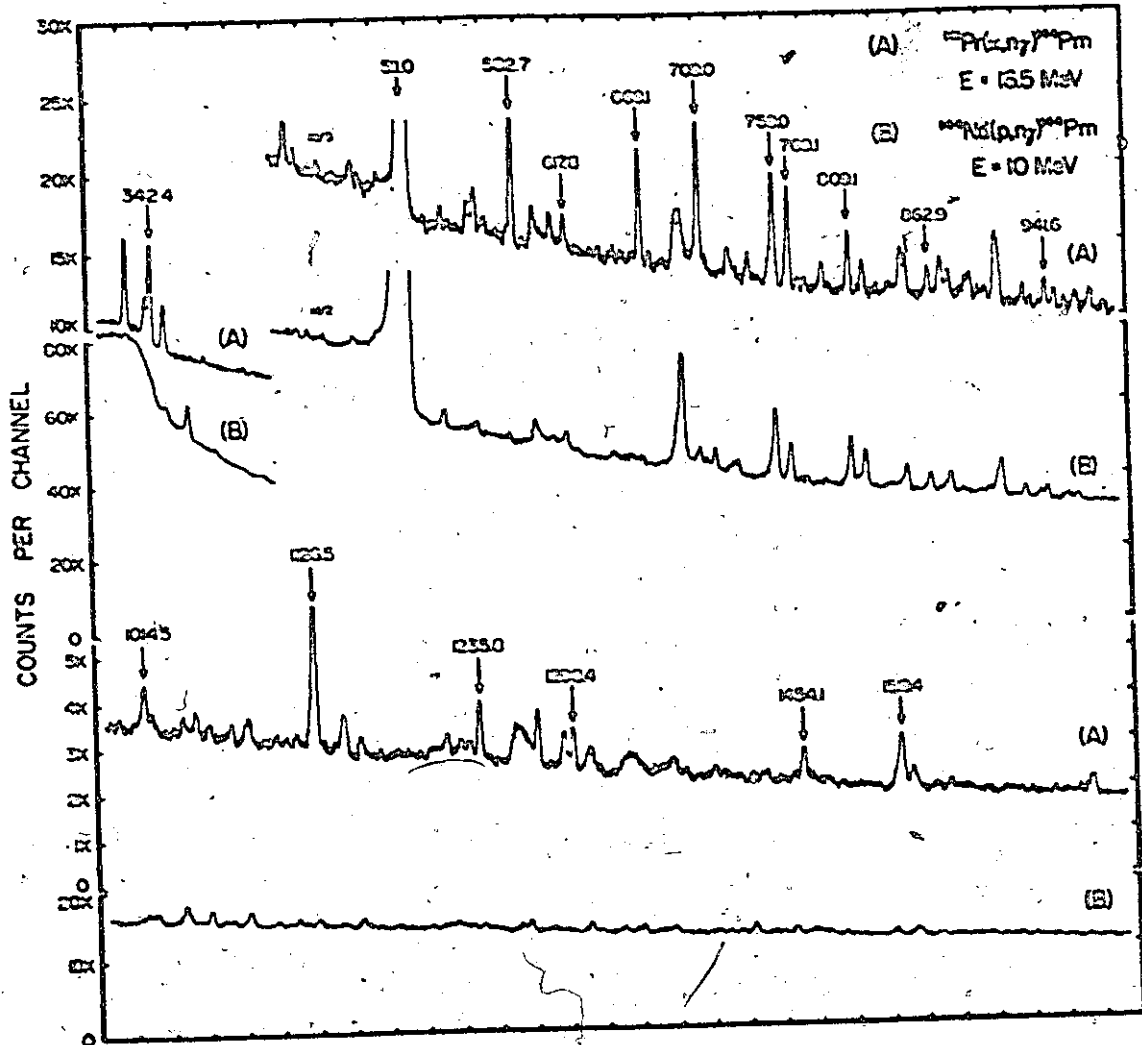


Fig. 3.3

Ge(Li) spectra (50 cm^3) from the (α, n)
and (p, n) reactions



seen in the enriched oxide exposure, although present in the spectra from the natural oxide exposure. The residual activity from the $^{144}\text{Nd}(p,n)^{144}\text{Pm}$ and $^{141}\text{Pr}(\alpha,n)^{144}\text{Pm}$ runs was dominated by the decay lines of ^{144}Pm and is discussed in Appendix 4.

Since it was felt that an accurate determination of the γ ray energies would be invaluable in the subsequent construction of the ^{144}Pm level scheme, the (α,n) reaction was studied concurrently with standard energy sources (Table 3.1). Steady beam currents of ~ 20 nA were maintained for ~ 15 hours for the 0.9cm^3 spectra, and ~ 8 hours for the 50cm^3 spectra. The positions of the sources were chosen so that the calibration peaks were approximately the same intensity as the neighbouring strong peaks from the target. Once the energies of the strong peaks were determined, they were used as internal standards for weaker peaks in spectra of the (α,n) activity only. Using JAGSPOT, calibration curves for the energy dependent shape parameters, δ and ϵ , were found for the strong peaks in each spectrum, thus allowing the positions and intensities of the weaker and poorly resolved peaks to be determined more reliably. The peak energies were fitted by a quadratic function of peak position within the range of the calibration sources, and by a linear function outside the range. The quadratic terms, used to correct for minor non-linearities in the system, were very small, in fact the quadratic and linear fits predicted essentially the same energies.

The errors in the energies, computed by JAGSPOT, arise from the statistical uncertainties in the least squares fit and in the peak positions. By locating the sources in front of the $\text{Ge}(\text{Li})$

detector, the effects due to source orientation (Gunnink 1968) were minimised, thus contributing negligible error in the energy calibration. Corrections for nuclear recoil, estimated to be <1 eV, were ignored.

3.3c ($\alpha, n\gamma$) and (p, n γ) Excitation Functions

In order to identify those γ rays from the $^{141}\text{Pr}(\alpha, n)$ and $^{144}\text{Nd}(\text{p}, n)$ reactions, spectra were recorded with α beams of 11.4, 14.0, 16.5 and 20.0 MeV, and proton beams of 3.6, 4.15, 4.5 and 5.2 MeV incident on thick targets. The respective thresholds are 10.8 and 3.2 MeV. Excitation functions for the strongest lines are given in Fig. 3.3 for the (α, n) reaction, and Fig. 3.4 for the (p, n) reaction. Weaker lines observed with α energies of 16.5 MeV and 20 MeV, but absent at lower energies, are not shown. In the 20 MeV α run some additional lines which were present have been identified with the ($\alpha, 2n$) reaction which has a threshold of 16.8 MeV.

The spectrum from the natural Nd_2O_3 target was also studied with a 4 MeV proton beam since lines, already mentioned, from the isotopic impurities in the enriched target could have contributed significantly at the low beam energies. The threshold for the $^{145}\text{Nd}(\text{p}, n)^{145}\text{Pm}$ reaction is only 0.9 MeV.

It is evident from Figs. 3.3 and 3.4 that most of the lines exhibit similar excitation functions consistent with the (α, n) and (p, n) reactions. γ rays not ascribed to ^{144}Pr were rejected for one or more of the following reasons:

- 1) excitation functions not consistent with the (α, n) and

Fig. 3.3

γ ray excitation functions for the $^{141}\text{Pr}(\alpha, n)^{144}\text{Pm}$ reaction. The observed γ ray intensities have been normalised with respect to the beam charge, but have not been corrected for detector efficiency and absorption in the target.

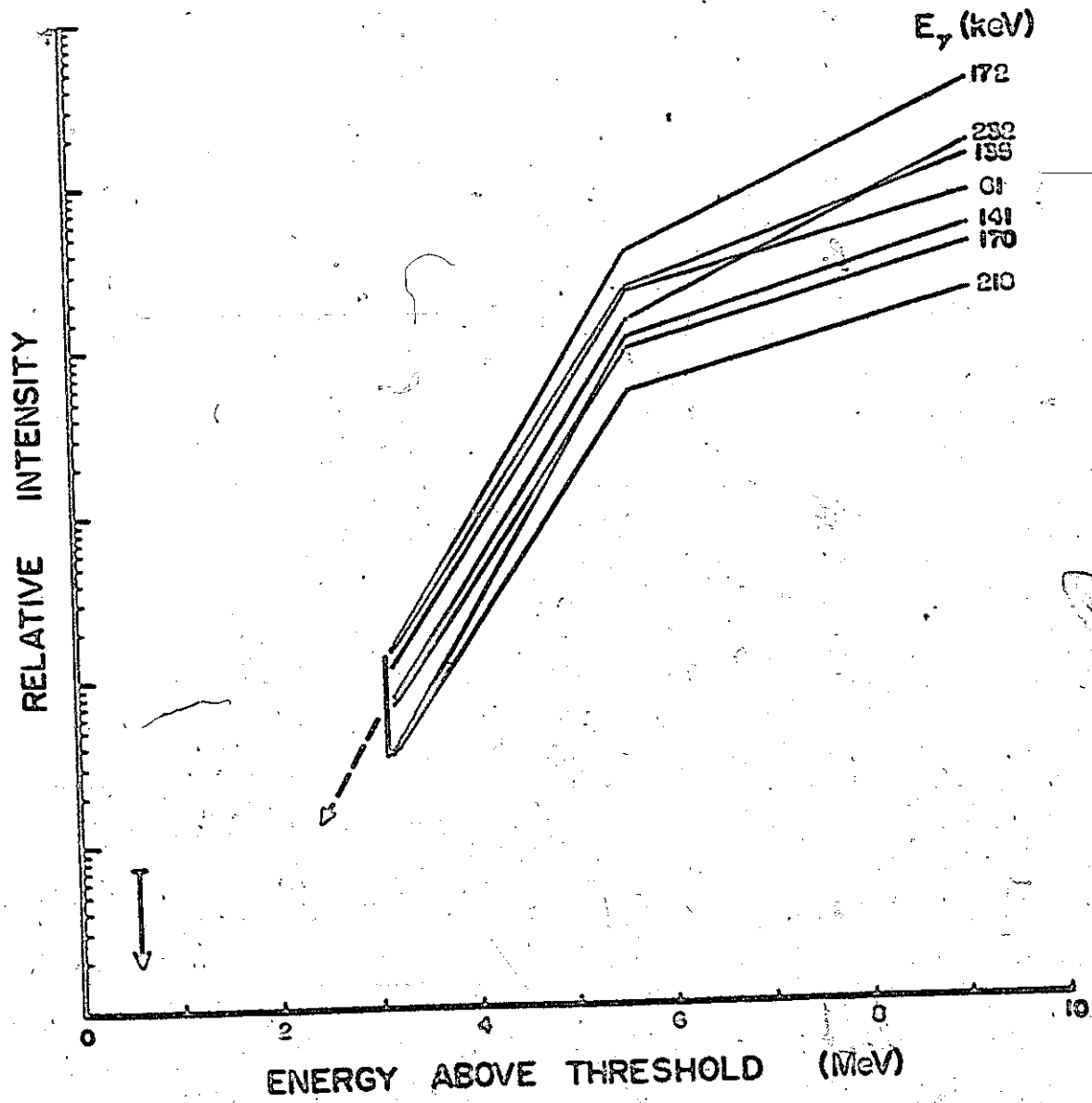
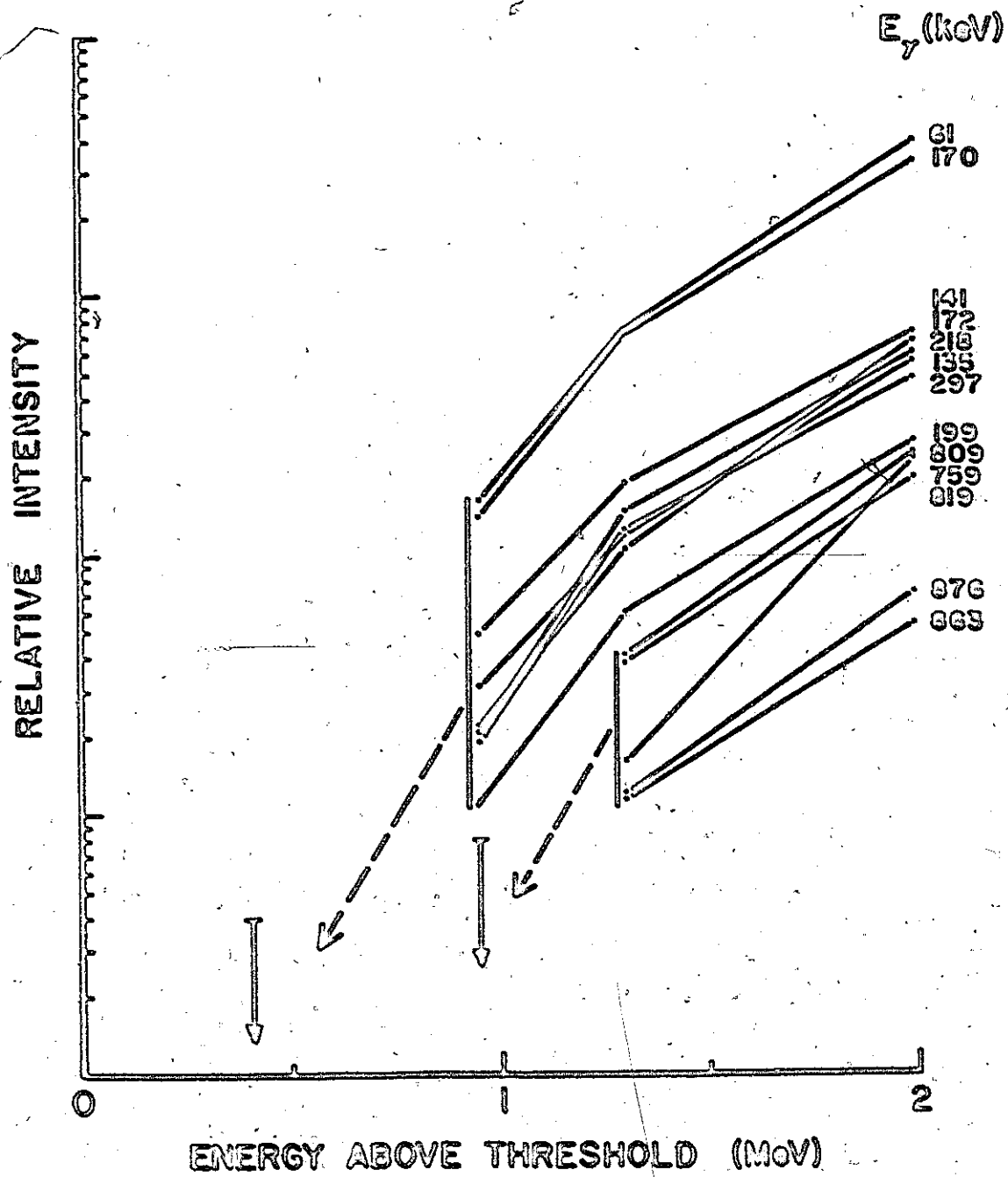


Fig. 3.4

γ ray excitation functions for the $^{144}\text{Nd}(p,n)^{144}\text{Pm}$ reaction. The observed γ ray intensities have been normalised with respect to the beam charge, but have not been corrected for detector efficiencies and absorption in the target.



(p,n) reactions

- 2) energy the same as that expected from a reaction in the known target impurities, slits, beam line or from a competing reaction in the target
- 3) inconsistent intensity in different exposures at the same beam energy
- 4) energy the same as a γ ray observed with beam off.

The γ rays which have been assigned to ^{144}Pm are given in Table 3.2. It should be noted, however, that some of the weakest lines have been observed in only (α,n) or (p,n) spectra with the best statistics, and hence their assignment to ^{144}Pm must be considered tentative. Those from impurities and competing reactions are presented in Table 3.3.

The probable errors in the quoted relative intensities include: statistical error in measuring peak area, $\sim 5\%$ error in measuring relative efficiencies of detectors, and the error in calculating γ ray absorption in the target (Appendix 3). An estimated 5% error, which may arise from angular distribution effects, is not included.

3.3d X Ray Region in the (α,n) Reaction

By removing the Mo-Cu graded absorbers from the small windowless Ge(Li) detector, to minimise the effects due to absorption, it was possible to look for very low energy γ rays (<100 keV) involving the low lying states found in the particle transfer studies. (Such an investigation also served the purpose of analyzing the purity of the target.) An example of such a spectrum, from the (α,n) reaction at 16.5 MeV, is shown in Fig. 3.5.

Table 3.2

γ Ray Energies and Intensities from the
 $^{141}\text{Pr}(\alpha, n)^{144}\text{Pm}$ and $^{144}\text{Nd}(p, n)^{144}\text{Pm}$ Reactions

Energy (keV)	Error in Energy (keV)	$(\alpha, n) E_{\alpha}=16.5 \text{ MeV}$		$(p, n) E_p=10 \text{ MeV}$	
		Intensity	Error in Intensity	Intensity	Error in Intensity
55.469	0.053	1.10	0.25	<3	
60.737	0.021	52.4	4.3	152	18
71.960	0.030	4.21	0.36	13.0	1.8
78.840	0.060	0.86	0.10	1.88	0.29
83.985	0.030	4.62	0.26	17.8	2.2
90.371	0.092	0.57	0.13	<0.5	
105.940	0.050	1.15	0.10	<0.5	
107.064	0.040	1.40	0.12	2.28	0.18
108.571	0.038	1.36	0.11	1.14	0.13
113.349	0.020	1.89	0.10	8.10	0.48
130.193	0.087	0.75	0.10	<0.5	
134.707	0.014	39.0	1.6	67.9	3.9
140.726	0.014	20.5	0.9	50.9	2.9
151.521	0.095	0.90	0.12	<0.5	
157.996	0.080	<0.5		1.63	0.21
169.879	0.010	24.8	1.1	132.6	7.5
171.798	0.010	100.0	4.2	100.0	5.7
184.270	0.030	4.48	0.26	3.06	0.40
195.417	0.016	8.74	0.41	14.1	0.9
199.252	0.014	8.49	0.41	30.0	1.7
212.624	0.050	1.69	0.19	6.49	0.44
218.564	0.015	23.1	0.9	82.6	3.5
223.715	0.071	1.92	0.23	<1	
232.412	0.024	72.9	3.0	47.0	2.1
281.938	0.045	28.3	1.2	9.4	0.7
283.155	0.094	4.03	0.33	16.8	1.0

(continued)

Energy (keV)	Error in Energy (keV)	$(\alpha, n) E_{\alpha}=16.5 \text{ MeV}$		$(p, n) E_p=10 \text{ MeV}$	
		Intensity	Error in Intensity	Intensity	Error in Intensity
296.544	0.037	7.21	0.46	34.5	1.6
326.537	0.045	15.3	0.9	3.17	0.73
342.376	0.025	18.9	0.9	<7	(a)
432.87	0.12	4.06	0.31	<1	
446.30	0.50	<1		2.19	0.52
453.46	0.31	1.61	0.27	<1	
456.80	0.50	<1		1.46	0.46
535.20	0.30	1.56	0.45	11.5	1.0
553.67	0.17	4.15	0.34	2.88	0.70
563.67	0.34	2.36	0.34	<1	
578.80	0.70	2.09	0.90	2.18	0.65
608.66	0.12	3.57	0.37	2.68	0.62
669.07	0.12	16.0	0.9	4.18	0.77
675.30	0.50	1.78	0.32	<2	
707.97	0.41	<2		8.52	0.90
718.60	0.20	<2		9.6	1.0
731.20	0.30	<2		8.22	0.95
733.60	0.30	<2		9.9	1.1
741.69	0.21	4.85	0.48	<2	
756.17	0.45	2.80	0.46	3.4	1.1
759.03	0.10	20.7	1.1	61.9	3.3
769.10	0.10	17.1	0.8	35.2	1.6
775.8	1.0	1.90	0.40	3.80	0.70
780.0	1.0	2.30	0.40	6.4	0.9
791.03	0.21	5.67	0.38	5.0	1.0
809.10	0.10	11.4	0.7	43.5	2.0
815.0	1.0	<2		5.40	0.63
819.21	0.15	6.31	0.51	32.4	1.6
862.89	0.23	5.56	0.42	17.9	0.9
876.40	0.17	5.79	0.57	20.5	1.1
887.23	0.47	2.68	0.59	<2	
896.0	1.0	<2		3.74	0.90
908.42	0.17	12.2	0.8	8.6	1.0
910.93	0.20	10.6	0.8	37.2	1.8

(continued)

Energy (keV)	Error in Energy (keV)	(α, n) $E_{\alpha}=16.5$ MeV		(p, n) $E_p=10$ MeV	
		Intensity	Error in Intensity	Intensity	Error in Intensity
926.42	0.26	4.38	0.48	12.8	0.8
931.17	0.50	2.25	0.45	<2	
936.90	0.40	1.60	0.55	7.31	0.85
941.58	0.18	6.34	0.54	13.5	0.8
948.15	0.23	5.06	0.53	<2	
962.23	0.21	4.35	0.78	7.8	1.1
1019.02	0.23	4.09	0.53	10.0	1.6
1048.46	0.18	5.0	1.1	<2	
1058.12	0.35	4.25	0.71	17.0	1.1
1071.32	0.29	4.85	0.49	7.2	1.3
1079.95	0.73	2.65	0.63	2.49	0.74
1083.08	0.23	5.80	0.67	16.1	0.9
1114.50	0.40	2.67	0.68	4.90	0.96
1128.00	0.30	<2		9.5	1.0
1144.60	0.74	6.1	1.2	3.8	1.0
1157.57	0.30	4.47	0.75	12.0	1.2
1214.56	0.21	5.05	0.88	<3	
1220.63	0.47	4.8	1.0	7.3	1.1
1230.05	0.23	5.14	0.84	4.2	0.9
1309.0 (b)	1.0	12.7	1.4	14.3	1.5
1331.2	1.0	<3		8.6	1.3
1335.0 (b)	2.0	21.0	2.0	<3	
1342.0	1.0	<3		15.4	1.6
1421.38	0.47	4.15	0.70	14.0	1.6
1448.00	0.80	1.46	0.65	10.0	1.4
1514.40	0.50	<3		11.6	1.6
1545.0	1.0	<3		11.3	1.5

(a) Peak on rapidly varying Compton background

(b) Broad

Table 3.3
 γ Ray Energies and Intensities
 from Impurity Reactions

Energy (keV)	Error in Energy (keV)	$(\alpha, n) E_{\alpha} = 16.5 \text{ MeV}$		$(p, n) E_p = 10 \text{ MeV}$		Comments
		Intensity	Error in Intensity	Intensity	Error in Intensity	
53.474	0.090	2.86	0.82	7.2	1.2	(a)
73.850	0.030	2.05	0.22			(b)
109.891	0.010	36.5	1.8	7.83	0.52	(c)
136.30	0.15	1.69	0.20			(d)
145.441	0.013	23.4	1.2			(e)
165.32	0.22	0.79	0.15			(d)
197.141	0.010	62.2	3.2	14.4	1.0	(c)
208.465	0.080			4.46	0.41	(f)
238.319	0.036	5.34	0.33			(g)
275.35	0.13	2.57	0.40			(g)
301.51	0.21	4.10	0.30			(d)
339.45	0.10	7.80	0.10			(h)
350.543	0.069	9.62	0.86			(i)
438.73	0.30	1.33	0.27	3.55	0.54	(j)
476.90	0.53	1.80	0.40	3.78	0.70	(k)
511.01	0.20					(l)
558.03	0.10	6.82	0.53	8.21	0.73	(m)
582.73	0.10	18.1	1.5			(b)
596.90	0.50					(n)
617.90	0.52	4.11	0.33	8.79	0.86	(k)
650.76	0.50			6.42	0.83	(o)
693.80	0.55					(p)
696.60	0.48	4.1	1.2			(k)
708.96	0.15	22.0	1.3			(o)
728.52	0.23	7.0	1.0	4.34	0.68	(o)
836.0	1.0	1.72	0.32			(o)
842.80	0.34	7.76	0.43	3.39	0.64	(q)
846.60	0.13	7.42	0.42	23.7	1.1	(r)
871.24	0.21	7.93	0.63	2.61	0.70	(s)

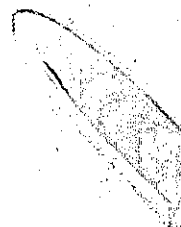
(continued)

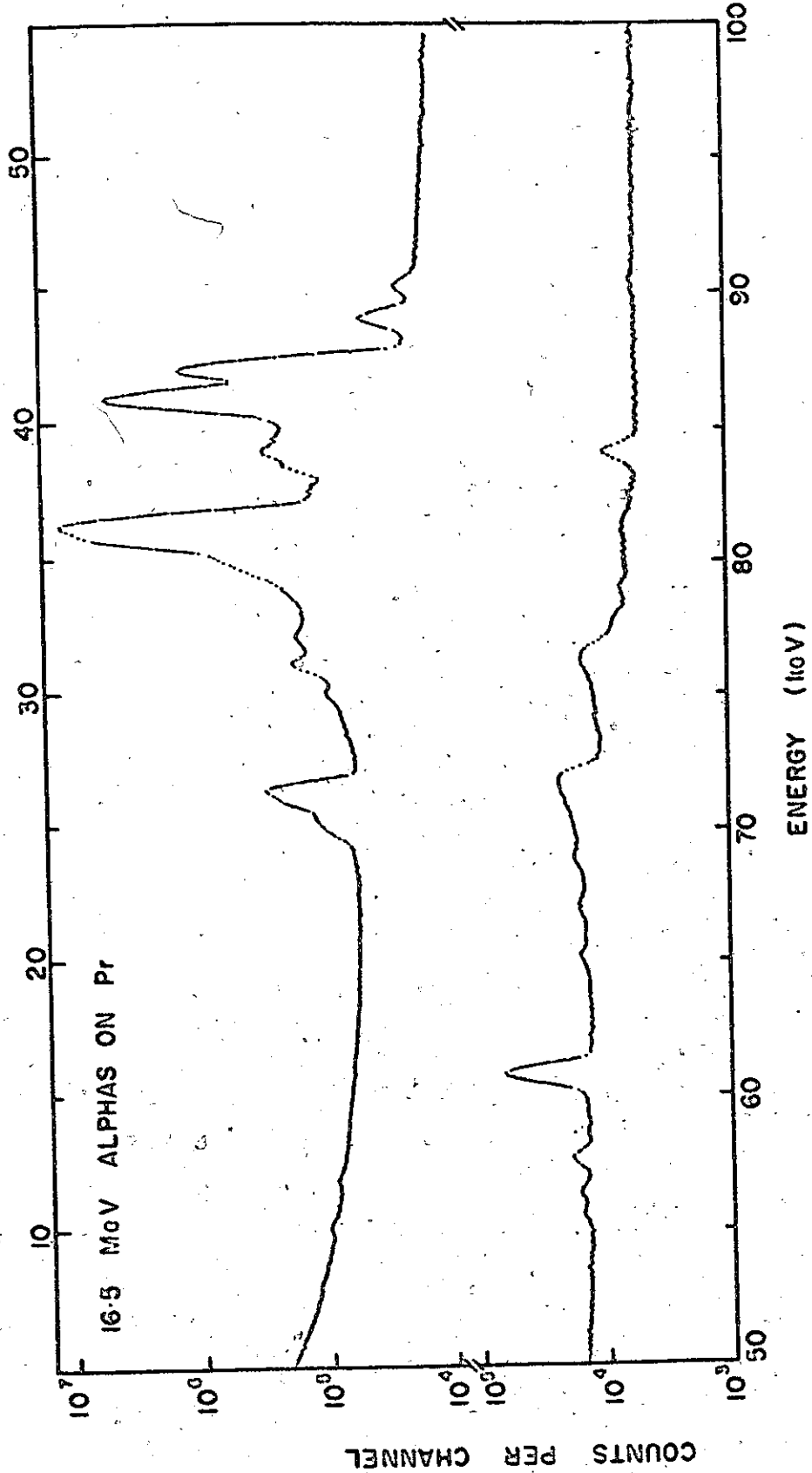
Energy (keV)	Error in Energy (keV)	$(\alpha, n) E_{\alpha} = 16.5 \text{ MeV}$		$(p, n) E_p = 10 \text{ MeV}$		Comments
		Intensity	Error in Intensity	Intensity	Error in Intensity	
890.08	0.32	4.55	0.58			(b)
955.31	0.53	3.30	0.51	7.5	1.2	(o)
972.54	0.68	5.12	0.50			(e)
981.91	0.42	2.85	0.52			(e)
1014.50	0.40	11.5	1.0	13.3	1.7	(q)
1040.51	0.54	3.51	0.89	21.9	1.9	(t)
1126.50	0.20	41.3	3.2			(e)
1146.87	0.32	8.1	1.2	4.1	1.0	(o)
1235.89	0.22	17.3	1.1	5.67	0.89	(c)
1262.0	1.0	36.1	4.5	7.8	0.90	(o)
1274.35	0.10	18.8	1.0			(f)
1292.43	0.12	12.3	1.3			(e)
1298.41	0.12	12.4	1.3			(e)
1366.0	1.0	11.2	1.8	7.3	1.2	(t)
1430.0	1.0	4.43	0.56			(t)
1454.10	0.50	12.5	1.4			(t)
1519.40	0.50	34.2	2.9			(t)
1528.50	0.37	13.6	1.6			(t)
1530.0	1.0			19.8	1.9	(t)
1545.0	1.0			11.3	1.5	(t)

- (a) $^{73}\text{Ge}(n, n')^{73}\text{Ge}$?
 (b) $^{19}\text{F}(\alpha, n)^{22}\text{Na}$
 (c) $^{19}\text{F}(\alpha, \alpha')^{19}\text{F}$, $^{19}\text{F}(p, p')^{19}\text{F}$
 (d) $^{181}\text{Ta}(\alpha, \alpha')^{181}\text{Ta}$
 (e) $^{141}\text{Pr}(\alpha, \alpha')^{141}\text{Pr}$
 (f) Nd isotopic impurity
 (g) $^{16}\text{O}(\alpha, n)^{19}\text{Ne}$
 (h) $^{57}\text{Fe}(\alpha, \alpha')^{57}\text{Fe}$
 (i) $^{19}\text{F}(\alpha, p)^{21}\text{Ne}$ and/or $^{18}\text{O}(\alpha, n)^{21}\text{Ne}$
 (j) $^{23}\text{Na}(\alpha, \alpha')^{23}\text{Na}$, $^{23}\text{Na}(p, p')^{23}\text{Na}$
 (k) $^{144}\text{Nd}(p, p')^{144}\text{Nd}$ and/or $^{144}\text{Pm}(e.c.)^{144}\text{Nd}$
 (l) Annihilation Radiation
 (m) $^{114}\text{Cd}(n, n')^{114}\text{Cd}$?
 (n) $^{74}\text{Ge}(n, n')^{74}\text{Ge}$
 (o) Intensity varies erratically in different runs at the same bombarding energy
 (p) $^{72}\text{Ge}(n, n')^{72}\text{Ge}$
 (q) $^{27}\text{Al}(n, n')^{27}\text{Al}$
 (r) $^{56}\text{Fe}(\alpha, \alpha')^{56}\text{Fe}$, $^{56}\text{Fe}(p, p')^{56}\text{Fe}$ and $^{56}\text{Co}(\beta^+)^{56}\text{Fe}$ background activity
 (s) $^{17}\text{O}(\alpha, \alpha')^{17}\text{O}$, $^{17}\text{O}(p, p')^{17}\text{O}$
 (t) Observed below threshold for the production of this energy γ ray energy in ^{144}Pm .

Fig. 3.5

Low Energy Spectrum from the (α, n) Reaction





As expected, the K_{α} and K_{β} X rays from the ^{141}Pr target dominate at 36 and 42 keV, also giving rise to broad sum peaks at 72 and 78 keV. The identification of the X rays is made relatively easy by the fact that the K_{α} and K_{β} lines usually form a characteristic intensity pattern. Although many strong additional lines are present they can be attributed to X rays from Pm, Ta and Au and their associated Ge X ray escape peaks. The latter arise when the Ge X rays which follow the production of a K-shell photoelectron escape from the crystal. This escape is more probable for very low energy γ rays because they interact near the surface of the crystal. (The energy deposited in the crystal is the X ray energy less the Ge X ray energy.) The presence of the Ge X rays indicates that the scattered γ ray sometimes escapes from the crystal, leaving only the Ge X ray.

Levels in ^{144}Pm which de-excite by internal conversion, give rise to the K_{β} lines at 43.8 and 45.0 keV as well as the K_{α} lines which are partly obscured by the target X rays. The analysis of the X ray region is summarised in Table 3.4. In most cases, only the strongest X ray, expected at a given energy, is quoted. The analysis has been made on the basis of the line energies and to some extent on their relative intensities. The latter could not be measured reliably due to the difficulties in obtaining an efficiency calibration at such low energies. The relatively weak lines attributed to Nd, Ce and La reflect the purity of the target material (their presence was confirmed by a study of the activity produced after irradiating the target material with thermal neutrons from the McMaster Nuclear Reactor). The X ray spectrum does not reveal any low energy lines which could

Table 3.4

Low Energy Lines Observed in the
 $^{141}\text{Pr}(\alpha, n)^{144}\text{Pm}$ Experiment

Observed Energy (keV)	Assignment
	The X ray nomenclature, energies and intensities are quoted from Lederer et al. (1968)
9.9(2)	Ge(K _α) 9.86 (50%); 9.89 (100%)
11.6(2)	Background activity
24.6(1)	Pr(K _{α2})-Ge(K _β) 24.55
25.1(1)	Pr(K _{α1})-Ge(K _β) 25.03
25.7(1)	Pr(K _{α2})-Ge(K _α) 25.67
26.2(1)	Pr(K _{α1})-Ge(K _α) 26.15
29.7(1)	Pr(K _{β1})-Ge(K _β) 29.7
30.8(1)	Pr(K _{β2})-Ge(K _β) 30.8
31.8(1)	Pr(K _{β2})-Ge(K _α) 31.9
33.0-35.0	La(K _{α2}) 33.03; La(K _{α1}) 33.44; Ce(K _{α2}) 34.28; Ce(K _{α1}) 34.72?
35.5(1)	Pr(K _{α2}) 35.55
35.97(5)	Pr(K _{α1}) 36.03
37.3(2)	Nd(K _{α1}) 37.36
38.2(1)	Pm(K _{α2}) 38.17
38.7(1)	Pm(K _{α1}) 38.72
39.3(1)	Ce(K _{β1}) 39.2
40.67(5)	Pr(K _{β1}) 40.7
41.72(5)	Pr(K _{β2}) 41.8
43.80(5)	Pm(K _{β1}) 43.8
45.00(5)	Pm(K _{β2}) 44.9
55.47(5)	
56.27(5)	Ta(K _{α2}) 56.28
57.54(5)	Ta(K _{α1}) 57.54
60.73(2)	
65.14(5)	Ta(K _{β1}) 65.2
67.03(5)	Au(K _{α2}) 66.99; Ta(K _{β2}) 67.0

(continued)

Observed Energy (keV)	Assignment The X ray nomenclature, energies and intensities are quoted from Lederer et al. (1968)
68.82(5)	Au(K _{α1}) 68.81
70.0-73.0	Pr(K _{α2}) + Pr(K _{α1}) 71.10; Pr(K _α) + Pr(K _{α2}) 71.58;
	Pr(K _{α1}) + Pr(K _{α1}) 72.06
73.9(2)	¹⁹ F(α,n) ²² Na
74.5-77.5	Pr(K _{α2}) + Pr(K _{β1}) 76.25; Pr(K _{α1}) + Pr(K _{β1}) 76.73;
	Pr(K _{α2}) + Pr(K _{β2}) 77.35
77.8(2)	Pr(K _{α1}) + Pr(K _{β2}) 77.83; Au(K _{β1}) 77.9
78.9(2)	
81.2(2)	Pr(K _{β1}) + Pr(K _{β1}) 81.4
83.98(4)	
90.4(3)	

be attributed to ^{144}Pm , except those already given in Table 3.2.

3.4 γ - γ Coincidence Studies

3.4a Experimental Outline

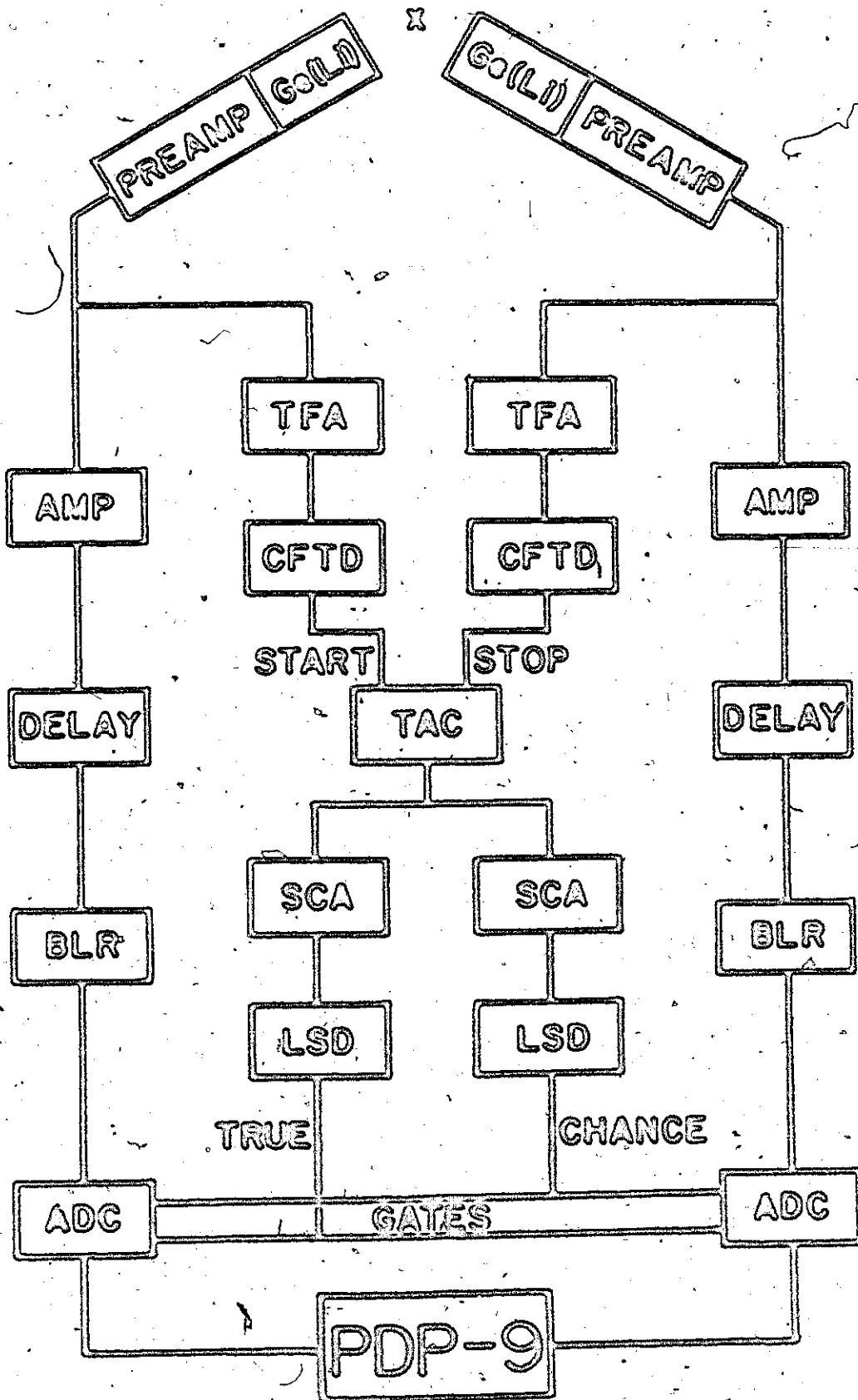
Although the information obtained from the measurement of γ ray energies and intensities can lead to the construction of a nuclear level scheme on the basis of yield functions and energy fits for cascading γ rays, such an approach frequently does not result in a unique level scheme. Additional information gained from γ - γ coincidence experiments resolves many of the ambiguities, and greatly increases one's confidence in a proposed scheme.

Gamma gamma coincidence experiments were undertaken with 12 cm³ and 40 cm³ Ge(Li) detectors using both the (a,n) and (p,n) reactions to produce ^{144}Pm in its excited states. Event by event data recording on magnetic tape was employed with a subsequent off line analysis. This method maximises the information that can be obtained in the experimental time available, and enables one to detect and correct for gain changes relatively easily. The block diagram of a typical γ - γ coincidence system is shown in Fig. 3.6.

The pulses from each detector were shaped by timing filter amplifiers and constant fraction timing discriminators, thus producing pulses compensated for variations in both amplitude and rise time. This method of timing, developed by Chase (1968), is particularly suited for Ge(Li) detectors. The pulses are then fed into a time-to-amplitude converter (TAC), one detector providing the "start" pulses, the other "stop" pulses. The spectrum of TAC pulses

Fig. 3.6°

Block diagram of γ - γ coincidence system for two detectors. AMP: Amplifier. BLR: Base Line Restorer. SCA: Single Channel Analyzer. TAC: Time-to-Amplitude Converter. TFA: Timing Filter Amplifier. CTD: Constant Fraction Timing Discriminator. ADC: Analog-to-Digital Converter. LSD: Logic Shaper and Delay.



contains one peak on a continuous background, the former produced by true coincident events, the latter by chance coincidences. The width of the peak is a measure of the time resolution of the system.

The linear pulses from the detectors were also shaped by Tennelec amplifiers and baseline restorers, and digitized by ADC's (conversion gain 4K) interfaced to a PDP-9 computer. The ADC's were gated by logic pulses from two SCA's set on the TAC output, one defining the peak region corresponding to true plus chance events, and the other defining an adjacent background region, corresponding to chance events only.

In addition to controlling the ADC's and the tape drive, the computer was used for buffer storage of the coincidence data which consisted of pairs of 18 bit words. Each word defined the "address" (channel number) of the detected γ ray, the ADC and the gating SCA. One bit was used as a time sequence bit, having the same value (0 or 1) for both words of a given pair and a different value for adjacent pairs. The storage was accomplished by two 1K buffers, which were alternately filled and dumped on magnetic tape. The computer program, written by L. Hughes, allowed the γ ray spectra from both ADC's and both time windows to be displayed for monitoring purposes during the experiment. The true plus chance and chance events each defined in effect a 3 dimensional surface, where the number of events per digital location is measured along the Z axis, the X and Y axes comprising the address of the γ rays detected in the respective detectors.

The data tapes were sorted in the following manner on the McMaster CDC6400 computer with the aid of a program written by

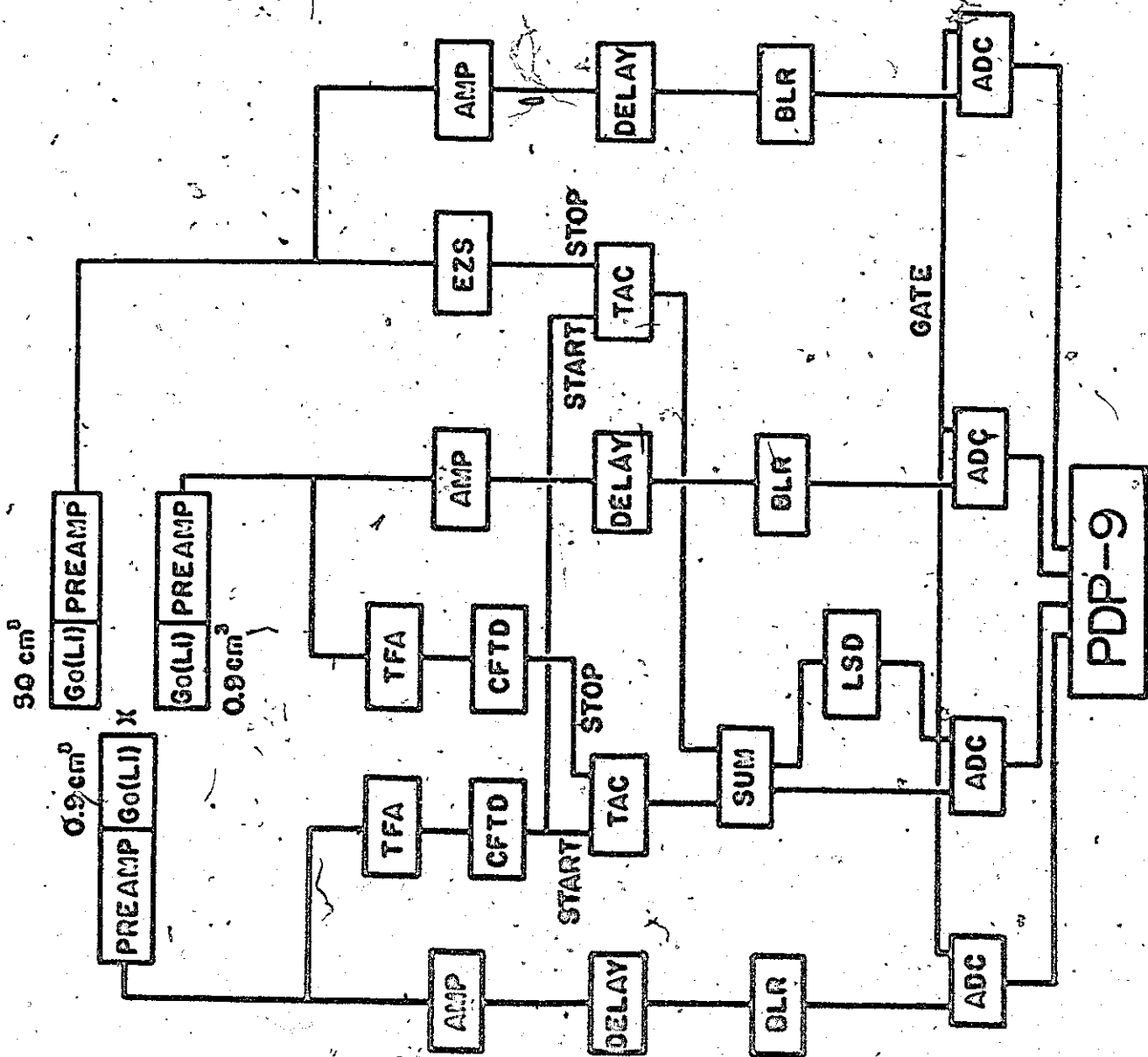
B. Cook. For each γ ray energy three windows were set on the γ ray photopeak, on a lower background region and on an upper background region. The combined width of the background windows was set equal to that of the photopeak window. Two spectra were obtained for each window, one containing true plus chance events, the other chance events. By appropriate subtraction of the chance spectra and the Compton background spectra, it was possible to obtain a resultant spectrum of γ rays in true coincidence with the desired photopeak. The spectra were compressed to 1024 channels to allow more windows to be sorted in the time available.

In a further (α, n) experiment, involving two $0.9 \text{ cm}^3 \text{ Ge(Li)}$ detectors and a $50 \text{ cm}^3 \text{ Ge(Li)}$ detector, the coincidence circuit was modified as shown in Fig. 3.7 to record coincident events between the two small detectors, and between one small detector and the large detector. The TAC outputs were summed, digitized, and recorded on magnetic tape together with the γ ray addresses, using a program written by D. T. Kelly. The word structure, used for storage, was similar to that mentioned earlier, except for the gating SCA bit which was not required since the time windows were set in the off-line analysis performed on a PDP-15 computer.

Since different timing pulses give rise to variations in the position and shape of the resultant time peak, a general sorting program, originally written by D. T. Kelly, was modified so that the time spectrum associated with each energy window could be obtained for both pairs of detectors. By setting time windows appropriate for the energy window, the resolving time could be effectively re-

Fig. 3.7

Block diagram of γ - γ coincidence system for three detectors. AMP: Amplifier. BLR: Base-Line Restorer. EZS: Extrapolated Zero Strobe. TFA: Timing Filter Amplifier. CFTD: Constant Fraction Timing Discriminator. TAC: Time-to-Amplitude Converter. ADC: Analog-to-Digital Converter. LSD: Logic Shaper and Delay.



duced thus improving the ratio of true to accidental events. The coincident events were then sorted in the manner already outlined.

3.4b γ - γ Coincidence Results

The $^{141}\text{Pr}(\alpha, n\gamma\gamma)^{144}\text{Pm}$ reaction was studied initially with 12 cm³ and 40 cm³ Ge(Li) detectors. During a period of 72 hours events were accumulated on three 2400 foot magnetic tapes. The time resolution was ~ 100 nsec (FWHM) with a true-to-chance ratio greater than 10:1. The detectors, placed on either side at 45° to the beam direction, were shielded from each other by several cm of Pb and Cd to minimize the detection of backscatter coincidences. Such events would otherwise occur if a γ ray were Compton scattered out of one detector into the other. Analysis of the data revealed many coincidences between lines in the energy range 100-400 keV, but very few outside this range. The absence of lower energy lines is partly attributed to the presence of absorbing materials on the detectors. The later singles spectra obtained with a 0.9 cm³ Ge(Li) detector warranted a further investigation of the $(\alpha, n\gamma\gamma)$ reaction since many of the coincident events involved the previously unresolved doublets at 171 and 282 keV.

In the subsequent experiment, using a 50 cm³ and two 0.9 cm³ Ge(Li) detectors, a total of seven 2400 foot magnetic tapes were obtained during 96 hours. Since the detectors subtended relatively small solid angles, the use of shielding was especially important. Compton scattered events would otherwise give rise to spurious peaks in the spectra, and could be difficult to distinguish from events of

interest. The tapes were sorted in the manner already outlined in the previous section. The resolving times were typically <15 nsec.

The $^{144}\text{Nd}(p,n\gamma)^{144}\text{Pm}$ was also briefly studied with 0.9 cm^3 and 50 cm^3 Ge(Li) detectors with comparable resolving times. The results were consistent with those obtained from the $(\alpha,n\gamma)$ experiment. A selection of spectra from the $(\alpha,n\gamma)$ and $(p,n\gamma)$ coincidence experiments is presented in Fig. 3.8, except for those windows producing no interesting features. The results of the coincidence experiments are summarized in Table 3.5.

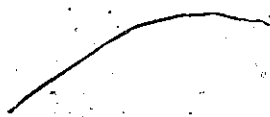
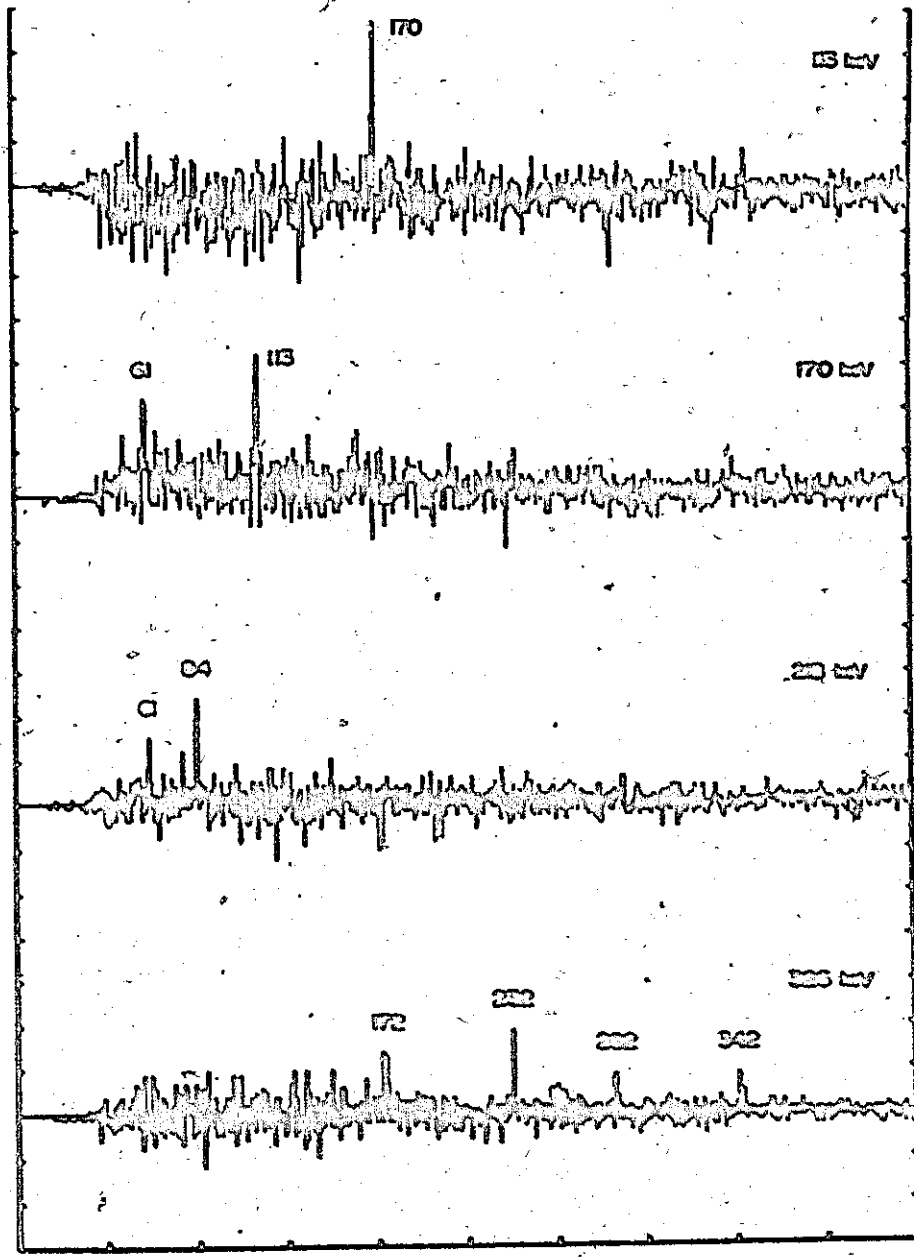
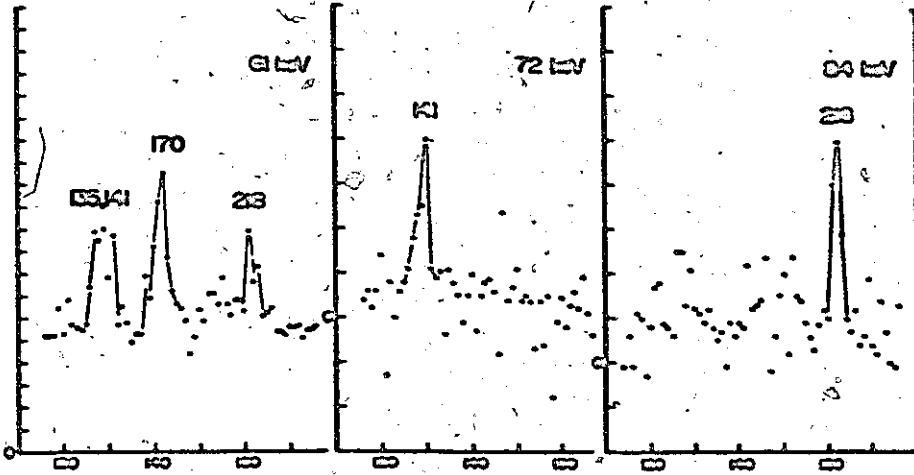


Fig. 3.8.

Ge(Li)-Ge(Li) coincidence spectra. The 40 cm^3 Ge(Li) spectra for the 61, 72, and 84 keV gates were obtained in the (p,n) experiment. The other gates, correspond to 0.9 cm^3 , 40 cm^3 and 50 cm^3 spectra from the (α ,n) reaction. One division on the ordinate is 10 counts per channel and on the abscissa 100 channels, unless otherwise shown.



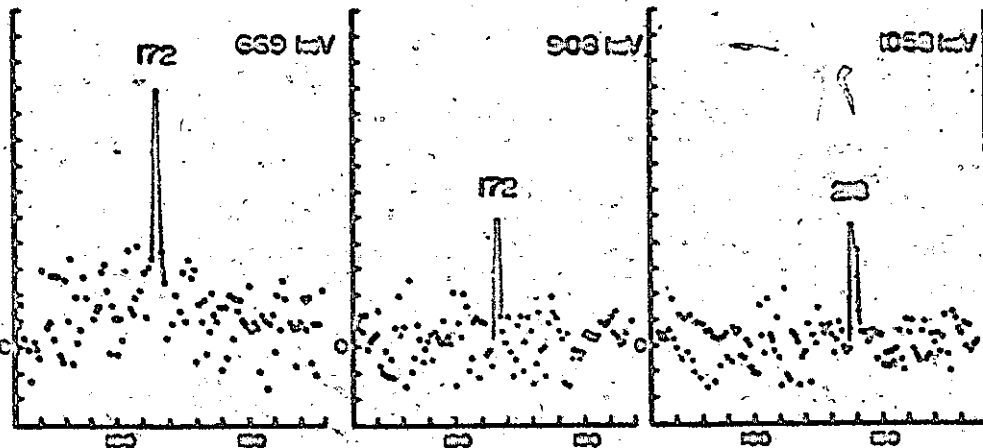
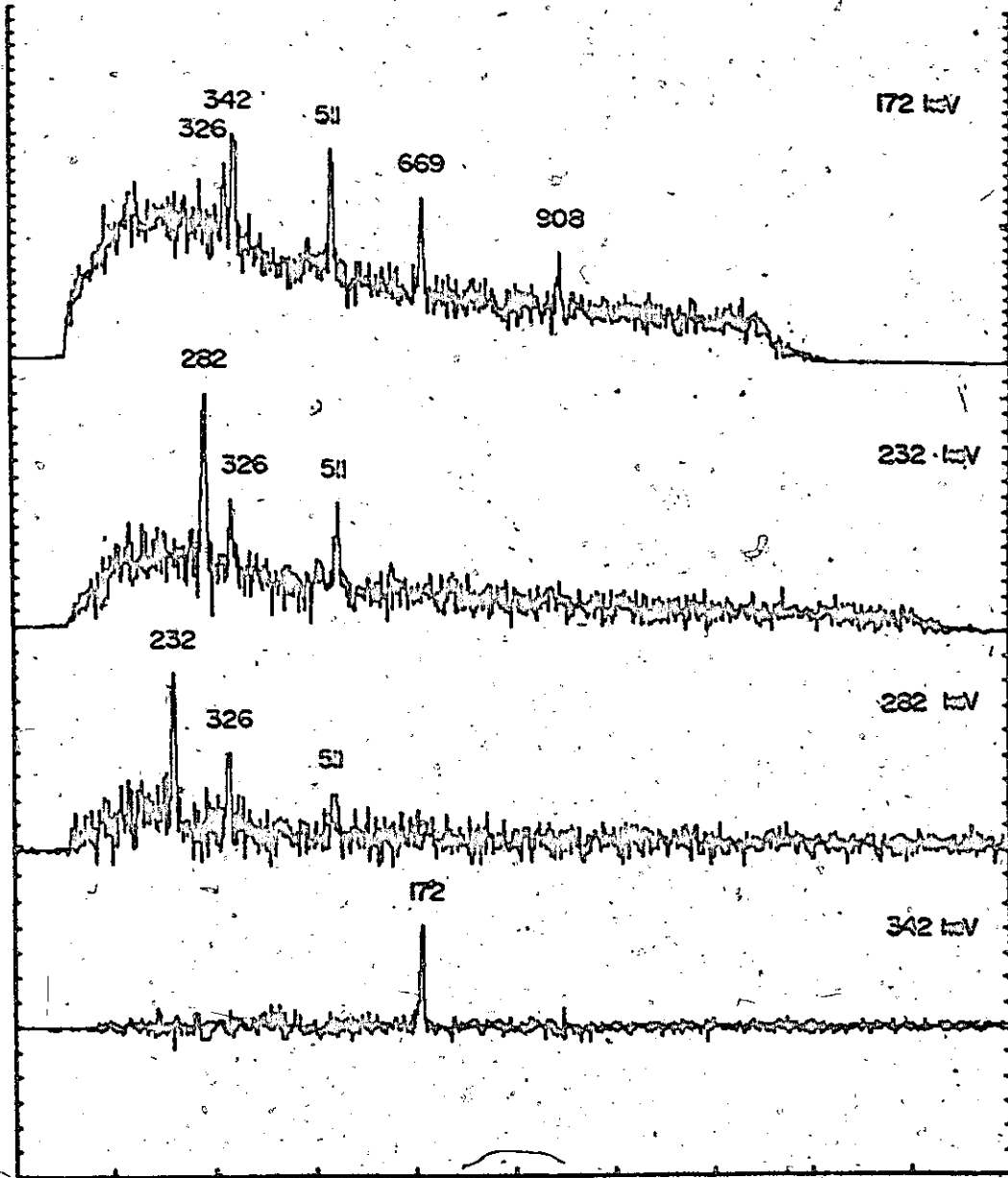


Table 3.5

Results of Coincidence Experiments

Gate (keV)	Coincident Lines (keV)
60.74	134.71, 140.73, 169.88, 218.56
71.96	140.73
83.99	218.56
113.35	169.88
169.88	60.74, 113.35
171.80	326.54, 342.38, 669.1, 908.4
218.56	60.74, 83.99
232.41	281.94, 326.54
281.94	232.41, 326.54
326.54	171.80, 232.41, 281.94, 342.38
342.38	171.80
669.1	171.80
908.4	171.80
1058.1	218.56

Chapter IV
LEVEL SCHEME OF ^{144}Pm

4.1 Introduction

As discussed in chapter 1, the main features of the N=83 odd-odd nuclei should be well described by the shell model. This is apparently the case for ^{140}La and ^{142}Pr in addition to the odd-even nuclei from ^{133}Sb to ^{145}Eu . The active protons are filling the $2d_{5/2}$, $1g_{7/2}$, $1h_{11/2}$, $2d_{3/2}$ and $3s_{1/2}$ orbits, while the odd neutron occupies the $2f_{7/2}$ or $3p_{3/2}$ orbits. The lowest states should be characterized by the $2d_{5/2}$ and $1g_{7/2}$ proton states while the neutron may confidently be assigned to the $2f_{7/2}$ state. At somewhat higher energies the remaining neutron and proton orbits should dominate, although vibrational states may also be present. (In ^{142}Nd the one phonon state lies at ~ 1.6 MeV.) It will thus be convenient to consider separately, the low lying levels and the higher excited states of ^{144}Pm .

4.2 Energy Levels Below 600 keV

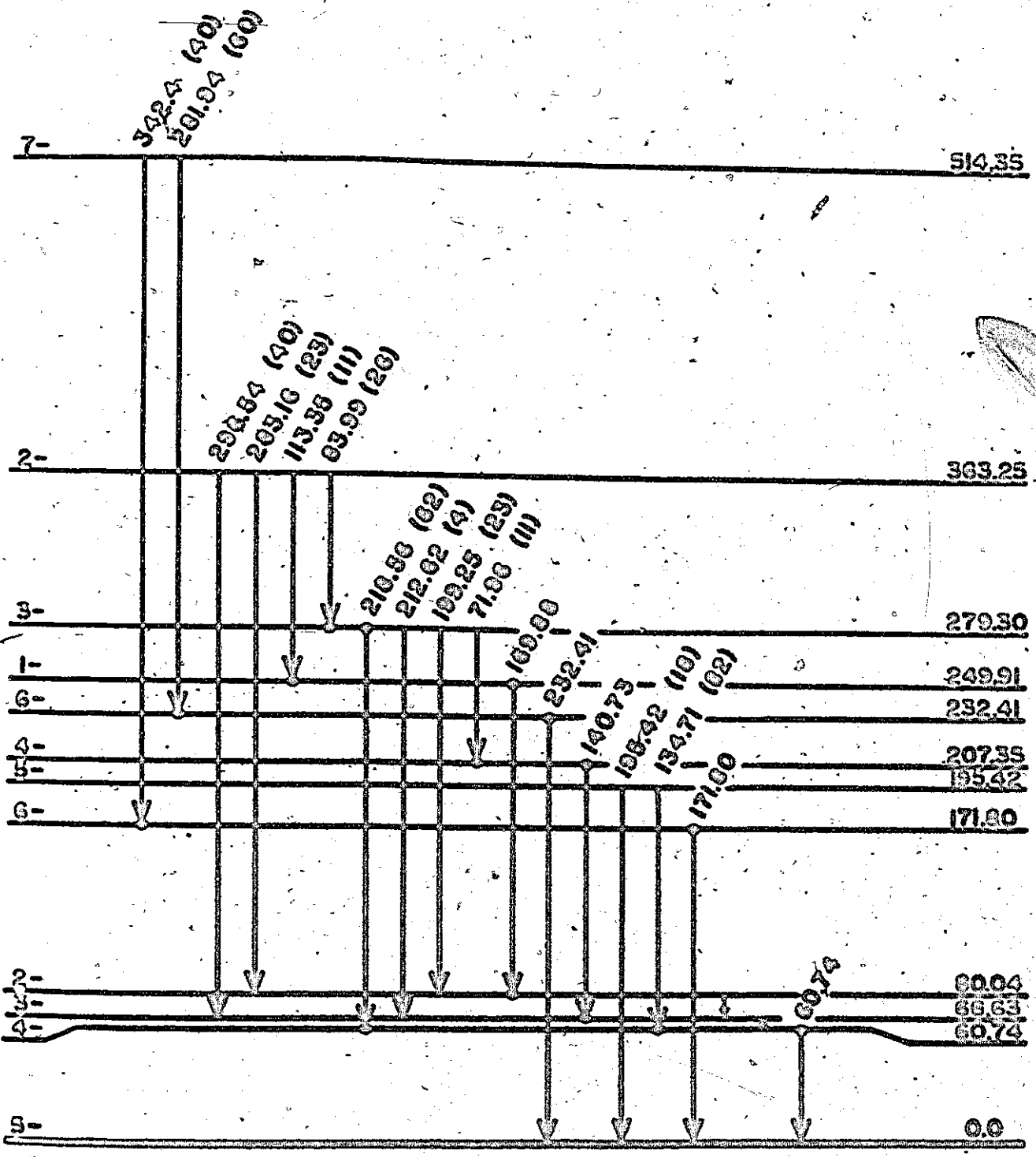
4.2a Construction of Low Energy Scheme

The low lying level scheme for ^{144}Pm , constructed on the basis of the experimental work described in chapters II and III, is shown in Fig. 4.1. The most obvious feature of the scheme is the group of 12 levels up to an excitation of 514 keV, beyond which there is a gap of more than 320 keV in which no levels are observed. A similar feature is also present in the level scheme of ^{142}Pr . The strongest γ transitions between these states have been placed by the

Fig. 4.1

Proposed level scheme of ^{144}Pm (<600 keV).

The notation of Nuclear Data Sheets applies.



144 Pm

coincidence experiments using the (α, n) and (p, n) reactions. Weaker γ rays, not seen in the coincidence spectra, have been assigned on the basis of energy fits. The line at 342.38 keV may actually be a doublet since its position in the level scheme is confirmed by the coincidence data but does not give a good fit on the basis of energy. The level energies, computed from the γ ray energies, are in good agreement with those obtained from the proton transfer experiments. The spin-parity assignments were deduced by applying the simple shell model for these states, to explain both the particle and γ ray results, as discussed in the following sections.

4.2b Parity Assignments

The low lying levels in ^{144}Pr are populated in the $(^3\text{He}, d)$ and (α, t) reactions by proton transfers which are consistent with mixed l values of 2 and 4. From general shell model considerations, odd l values of 1 and 3 should not contribute, although $l=5$ due to the $h_{11/2}$ state could be present. It is clear from Fig. 2.7 that none of the states have the latter assignment. It follows that the states have the same parity as the target ground state viz negative parity.

4.2c Spin Assignments

According to the simple shell model discussed in section 1.3, the state vectors should have the form

$$\begin{aligned}
 |JM\rangle_1 &= c_1 | \pi 2d_{5/2} \nu 2f_{7/2}; JM \rangle + \beta_1 | \pi 1g_{7/2} \nu 2f_{7/2}; JM \rangle \\
 |JM\rangle_2 &= c_2 | \pi 2d_{5/2} \nu 2f_{7/2}; JM \rangle + \beta_2 | \pi 1g_{7/2} \nu 2f_{7/2}; JM \rangle
 \end{aligned}
 \tag{4.1}$$

The resultant states include 6 pairs of levels with spins from 1 to 6 as well as a spin 0 and a spin 7 state, all having negative parity. The dominant mode of decay for all these states, except perhaps the lowest lying, should be transitions involving at least some M1 admixture, since they will be very much faster than the other allowed multipoles. This is also suggested by the experimental studies of ^{138}Cs (Monnard et al. 1972), ^{140}La (Burde et al. 1965) and ^{146}Eu (Antman et al. 1970). It is then possible to assign a unique spin to each of the levels on the basis of the following assumptions:

- 1) The levels are described by the wave vectors given by equation 4.1.
- 2) All observed γ transitions have some M1 admixture, so that $\Delta J=0, \pm 1$.

As a result, the maximum number of allowed transitions, involving a given state with spin J , is five for $J=2, 3, 4$ and 5 ; four for $J=1$ and 6 ; and two for $J=0$ and 7 . The spin and parity of the ground state has been measured by Arya et al. (1971) and found to be 5^- .

The state at 279 keV, which is fed by the 363 keV state decays to four states, thus involving the maximum number of transitions allowed by the model. The spin of the level is therefore restricted to 2, 3, 4 or 5. If its spin were 4 or 5, however, one of the allowed transitions would be to the ground state. Since this is not the case, its spin must be 2 or 3. The 218 keV γ ray, which de-excites the 279 keV state, and the 61 keV γ ray to the ground state are in prompt coincidence. Since the latter transition cannot be pure E2 from lifetime considerations, the 61 keV state has $J=4, 5$ or 6 . To account

for the 218 keV γ transition, the 279 and 61 keV states must have spins which differ by at most one unit. Hence $J=3$ for the 279 keV state and $J=4$ for the 61 keV state.

It follows that the other four states which feed or are fed by the 279 keV state (363, 207, 80 and 67 keV) have $J=2, 3$ and 4 , while the remaining low lying states must have $J=0, 1, 5, 6$ or 7 . It will be convenient to consider the states in the latter group first.

The 195 keV state decays to both the 61 keV state ($J=4$) and the ground state ($J=5$). Hence $J=5$ is the only possibility for this state such that $\Delta J \leq 1$. Also in this group, both the 172 and 232 keV states decay to the ground state, and must therefore be the two $J=6$ states ($J=5$ can be ruled out since the model allows only two such states). Similarly the 514 keV state which decays to the 172 and 232 keV states must be the $J=7$ state. The only remaining state belonging to this group is at 250 keV and must be $J=0$ or 1 since the $J=5, 6$ and 7 states have been identified. The $J=1$ assignment is the only possibility, however, since the 250 keV state is fed by the 363 keV state which belongs to the other group of states for which J is at least 2 . It follows immediately that the 363 keV state must have $J=2$ for the $\Delta J \leq 1$ condition to hold.

The states for which no spins have been assigned are at 67, 80 and 207 keV and are in the group with $J=2, 3$, and 4 . On the basis of the model, one must have $J=2$, one $J=3$, and the other $J=4$, since the other $J=2, 3, 4$ states have been identified.

The 80 and 67 keV states must have $J=2$ or 3 since the 363 keV state ($J=2$) decays to both. The 80 keV state is fed by the 250 keV state ($J=1$), so its spin is 2 . It follows that the 67 and 207 keV states have $J=3$ and 4 respectively.

Thus it is possible to satisfy the model and have every observed transition correspond to $\Delta J=0$ or $+1$. Furthermore, these constraints result in a unique set of spins as just explained. It is true that there are additional M1 transitions which are not observed, but nearly all of these would be quite low in energy (for example, the $J=4$ state at 207 keV could decay to the $J=5$ state at 195 keV), and so it is not unreasonable that they would escape detection. The possibility of a weak transition between the 232 and 172 keV states (both $J=6$) cannot be excluded because the transition energy is essentially the same as the strong 60.74 keV γ ray. (Coincidence data indicate that such a branch would be $<1\%$). Other transitions that should be allowed, but are not seen, are between the 207 keV state ($J=4$) and the ground ($J=5$) and first excited ($J=4$) states. With the wave vectors calculated in section 4.2g these transitions are predicted to be very, very weak.

4.2d Proton Transfer Reactions

The spins deduced on the basis of the γ ray work are in good overall agreement with those allowed by the proton transfer experiments. A comparison is given in Fig. 2.8. The agreement is poorest for states which are not well resolved, and thus may be a consequence of the peak fitting procedure. An examination of Fig. 2.7 indicates

a general pattern. If a state lies close to the $l=2$ curve, then the other state with the same spin lies close to the $l=4$ curve. Also the spin 7 level is consistent with pure $l=4$. These observations are to be expected from our model assumptions.

The spectroscopic factors extracted from the proton transfer experiments give some indication of the consistency of the simple shell model of the low lying levels. The sum rules, discussed in 2.1b give

$\sum_J \alpha^2 = \sum_J \beta^2 = 1$, for states with the same spin, except for $J=0$ and 7 where

$$\alpha^2 = 0 \text{ and } \beta^2 = 1$$

Table 4.1 shows the measured values of $\sum_J \alpha^2$, which are of course equal to $\sum_J \beta^2$. Although the spectroscopic factors could not be extracted exactly for each state, there is satisfactory agreement for the adopted spin assignments.

4.2c γ Ray Intensity Ratios

A study of Table 3.3 and Fig. 4.2 reveals that γ ray intensity ratios, measured from the (p,n) and (a,n) reactions, vary by almost an order of magnitude, the (p,n)/(a,n) ratio being smallest for γ rays de-exciting high spin states and largest for γ rays de-exciting low spin states. This is consistent with the general features of (a,n) and (p,n) reactions. The (p,n) reaction is expected to favour the population of relatively low spin states, whereas the (a,n) reaction should produce all spin states of interest fairly easily. (The target spins are 0^+ and $5/2^+$ respectively.)

Table 4.1

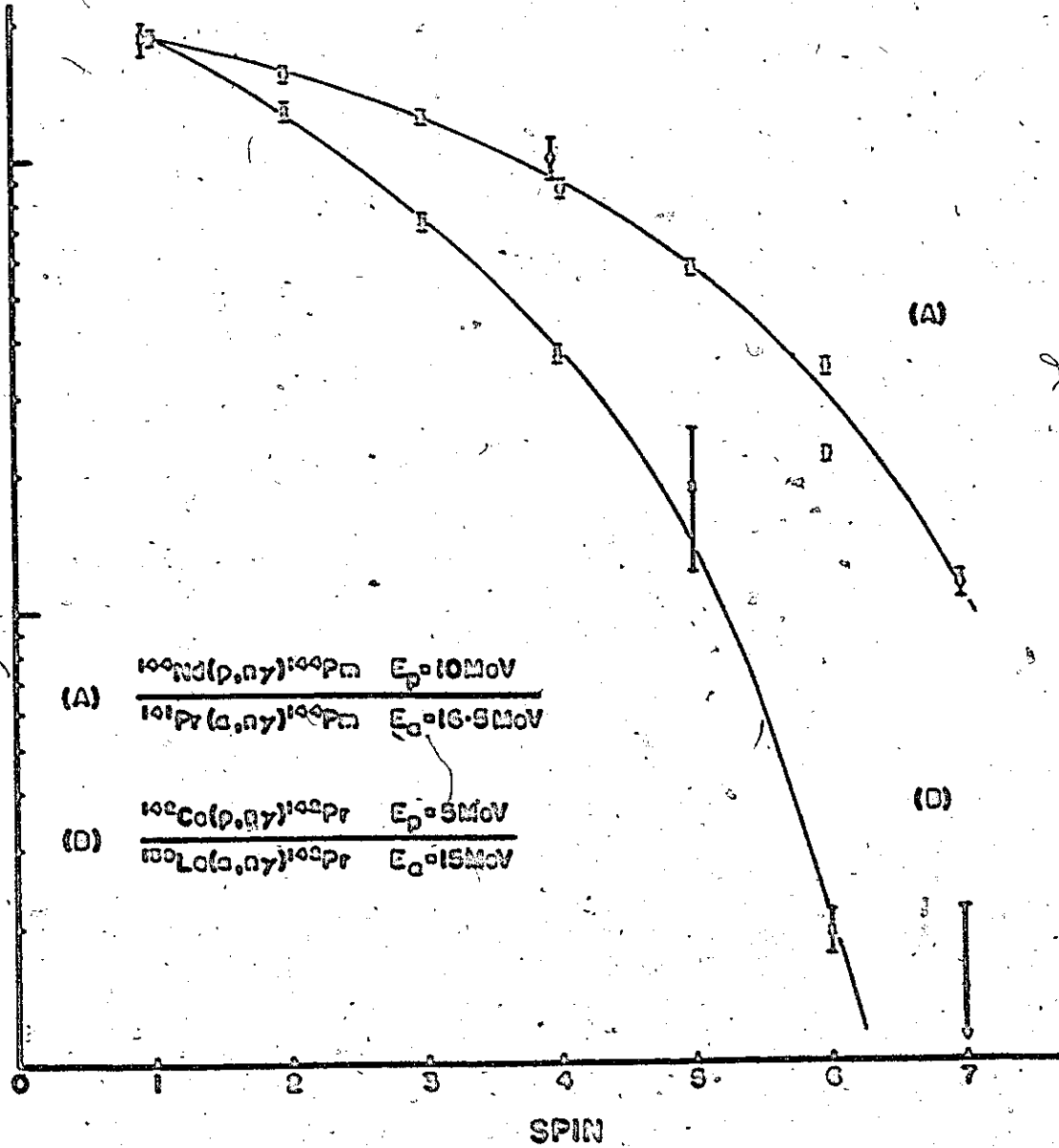
Summed spectroscopic factors from proton transfer reactions to ^{144}Pm

Spin	Energy (keV)	$\sum_J \alpha_{2d_{5/2}}^2$
1	249.9	>0.25
2	{ 80.0 363.3	>0.77
3	{ 66.6 279.3	>0.92
4	{ 60.7 207.4	>0.90
5	{ 0 195.4	1.15(20)
6	{ 171.8 232.4	0.88(24)
7	514.4	<0.05

Fig. 4.2

γ ray intensity ratios for the low lying states in ^{144}Pm
and ^{142}Pr , populated in the (α,n) and (p,n) reactions.

GAMMA RAY INTENSITY RATIO



A similar dependence is also found from the $^{139}\text{La}(\alpha, n)^{142}\text{Pr}$ and $^{142}\text{Ce}(p, n)^{142}\text{Pr}$ experiments carried out at beam energies of 15 MeV and 5 MeV respectively. The similarity is encouraging since the spins of the low lying levels in ^{142}Pr are those found from the (d,p) and (n, γ) work of Kern et al. (1968). The curve, however, falls off more rapidly for increasing spin values on account of the lower proton beam energy.

The γ ray intensity ratios from the $^{141}\text{Pr}(\alpha, n)^{144}\text{Pr}$ reactions at 16.5 and 20 MeV reveal a quite different, but expected, variation as shown in Fig. 4.3. The curve shows a shallow minimum between spins 2 and 3 which can be fed by the transfer of zero orbital angular momentum to the $5/2^+$ target state, and are thus strongly populated at both energies. For other spins, the reaction at 20 MeV is capable of transferring more angular momentum than at 16.5 MeV, thus accounting for the general shape of the curve.

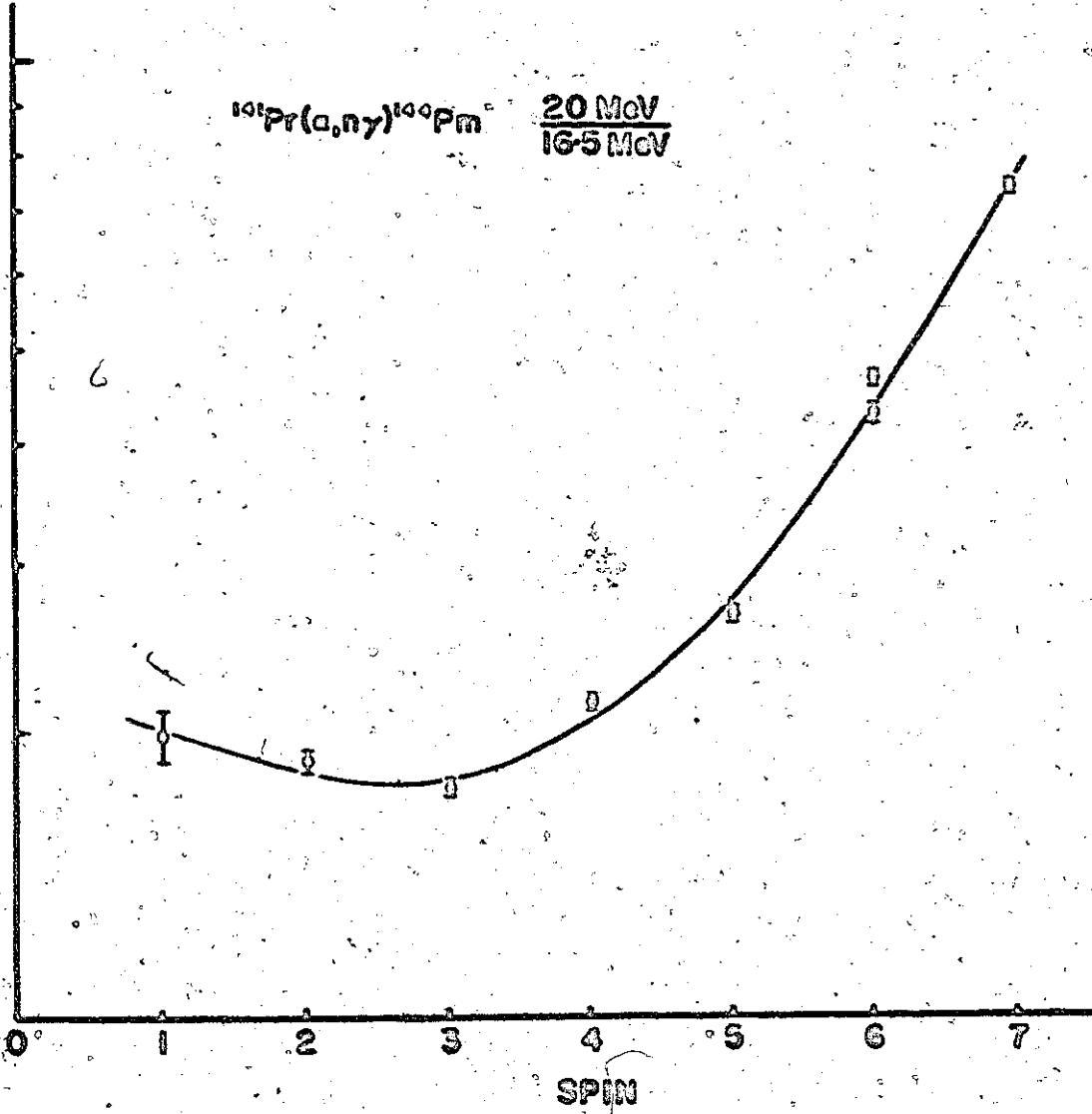
This could be a very useful approach in determining nuclear spins on account of its simplicity. One requires γ ray intensities from two reactions, which produce the states of interest, or one reaction at different bombarding energies. In most cases the γ ray ratio dependence on spin may be deduced empirically from a knowledge of the general features of the reactions, or constructed from similar reactions to neighbouring nuclei where the spins are known. The shape of the curve must depend strongly on the transmission coefficients of the incident and outgoing particles, and of course the target spin. The level densities of the compound and residual nuclei must also play some role, since the observed γ rays arise from states which can

Fig. 4.3

γ ray intensity ratios for the low lying states in ^{144}Pm , populated in the (α, n) reaction.

GAMMA RAY INTENSITY RATIO

$^{101}\text{Pr}(\alpha, n\gamma)^{140}\text{Pm}$ $\frac{20 \text{ MeV}}{16.5 \text{ MeV}}$



be populated directly by neutron emission from compound states, or indirectly by the decay of higher states in the residual nucleus. The decay properties of the latter states would thus be an additional consideration. In the present experiments the shapes of the curves do not exhibit appreciable fluctuations and would suggest that a detailed knowledge of the nuclear level densities and their decay modes (a formidable undertaking) is not required. A statistical description should be sufficient in cases where many compound and residual nuclear states are populated. (In the present experiments, using thick targets, states up to an excitation of ~ 6 MeV were accessible.)

It would be interesting to examine the feasibility of the method for extracting spins of levels, especially in regions of high level densities where the states are isolated only by γ ray experiments. The approach, however, would not be appropriate in cases where a reaction is sensitive to the detailed structure of the compound and residual nuclei. For example, resonance phenomena observed particularly in the study of light nuclei under certain experimental conditions could give rise to large fluctuations in the dependence of γ ray ratio on spin.

4.2f Lifetimes

From the γ - γ coincidence experiments it is possible to set upper limits on the lifetimes of most states, since time spectra were measured for each γ ray window. With the exception of the 195 and 363 keV states, for which the coincidence data were insufficient, all states have lifetimes which are < 10 nsec, the typical FWHM of the

tine spectra, and are probably much smaller than this limit.

The M1 Weisskopf estimate for the 61 keV γ ray (the lowest energy line observed in the coincidence experiments) gives a γ ray lifetime of $\sim 10^{-13}$ sec. For higher energy γ rays the estimated lifetimes will be smaller. The 80 and 67 keV states are assumed to decay via fast low energy transitions which have not been observed directly. Lifetime estimates for the lowest energy transition, between the 67 and 61 keV states, give an M1 γ decay lifetime of $\sim 10^{-8}$ sec. By including electron conversion, the estimated lifetime of the 67 keV state would be $\sim 10^{-10}$ sec. A similar lifetime is predicted for the decay of the 80 keV state to the 67 keV state. (The E2 transition from the 80 keV state to the 61 keV state would have a lifetime of $\sim 10^{-5}$ sec.) No supporting evidence has been found in the present work to confirm the existence of a 60 day activity in ^{144}Pm , suggested by Pagden et al. (1963). The experimental details are given in Appendix 4.

4.2g Branching Ratios

An important test of a given level scheme is the consistency of the branching ratios determined from different reactions. In the case of the $^{141}\text{Pr}(\alpha, n)^{144}\text{Pm}$ and $^{144}\text{Nd}(p, n)^{144}\text{Pm}$ reactions the γ ray intensities were measured using the same experimental set up. By taking the ratios of the observed intensities of each γ ray branching from a given level one can make a more sensitive test of the level scheme, since detector efficiencies need not be known. Corrections, however, must be made for γ ray absorption in the targets. The con-

puted intensity ratios for the different levels, presented in Table 4.2, are generally consistent except perhaps for the lowest energy lines at 72 and 84 keV. The small discrepancy, however, is probably not significant since the calculation of γ ray absorption in the target, employed in the (p,n) reaction, ignored irregularities in the structure of the oxide target as well as the presence of both carbon and oxygen in both target material and glue. The respective attenuations of 30% and 23% calculated for the 72 keV and 84 keV lines should therefore be increased.

The experimental branching ratios also provide a sensitive test of the model for the low energy levels, since the presence of relatively small admixtures in the wave-functions can appreciably modify their decay properties and would not be detected in the proton transfer experiments. Assuming that the state vectors have the form given already in section 1.3, the expression for the M1 transition rates between states depends on the amplitudes a and b , the relative phases in the wave function, and the values of the gyromagnetic ratios. The latter can be deduced from the magnetic moment data for the ground states of ^{139}La , ^{141}Pr and ^{141}Ce , and are given in Table 4.3. The ^{139}La and ^{141}Ce values are those employed by Kern et al. (1968) and Jurney et al. (1970), while the ^{141}Pr value has been taken from the work of Lew (1970).

Assuming the transitions to be pure M1, the amplitudes and phases were varied to best fit the experimental branching ratios. Since the phases are only relative they were chosen so that δ for the ground state and all c_i were positive. The criterion for goodness of fit, χ^2 ,

Table 4.2

(p,n)/(α ,n) γ ray intensity ratios

Level (keV)	Branching γ Ray (keV)	$\frac{(p,n)}{(\alpha,n)}$ Intensity Ratio
514.4	281.94	0.332(21)
	342.38	<0.37
363.3	83.99	3.85(43)
	113.35	4.29(24)
	283.16	4.17(34)
	296.54	4.79(26)
279.3	71.96	3.09(36)
	199.25	3.53(17)
	212.62	3.84(45)
	218.56	3.58(64)
195.4	134.71	1.74(7)
	195.42	1.61(8)

Table 4.3

Gyromagnetic ratios used in branching ratio analysis

Nucleus	Shell	Effective Gyromagnetic Ratio
^{139}La	$g_{7/2}$	0.794
^{141}Pr	$d_{5/2}$	1.65
^{141}Ce	$f_{7/2}$	-0.28

is defined as

$$\chi^2 = \frac{1}{N-1} \sum_{i=1}^N \left(\frac{R_{oi} - R_{ti}}{\Delta R_{oi}} \right)^2 \quad 4.2$$

where N is the number of ratios considered. R_{oi} and R_{ti} are the observed and theoretical branching ratios for the i^{th} γ ray, while ΔR_{oi} is the error associated with R_{oi} .

The experimental branching ratios, employed in the analysis, were those measured in the (α, n) reaction at 16.5 MeV, since they are the more precise and less dependent on the target absorption corrections than those from the (p, n) reaction. The experimental error in each branching ratio was determined using the relation

$$\left(\frac{\Delta R_{oj}}{R_{oj}} \right)^2 = \sum_i (\delta_{ij} - R_{oi})^2 \left(\frac{\Delta I_i}{I_i} \right)^2, \text{ where } \Delta I_i \text{ is the uncertainty in the}$$

intensity I_i (after correction for target absorption and efficiency) of the i^{th} branching γ ray. The summation extends over all branches of the j^{th} level.

In order to find minima for χ^2 , the initial search procedure was simplified by considering the branching of each level one at a time. The wave vector amplitudes of a given level, and those to which it decayed, were varied to minimise χ^2 . All possible M1 transitions were considered in the calculation except those very low energy lines at 6, 12, 14 and 37 keV which could not readily be detected. Upper limits were estimated for the 146 and 207 keV lines branching from the 207 keV state and for the 60 keV branch from the 232 keV state. For these states solutions consistent with the limits were sought.

In several cases it was convenient to consider only some of

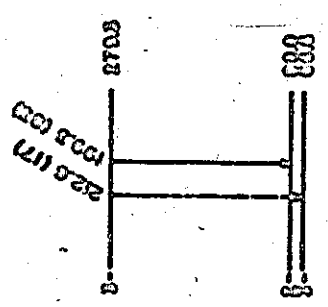
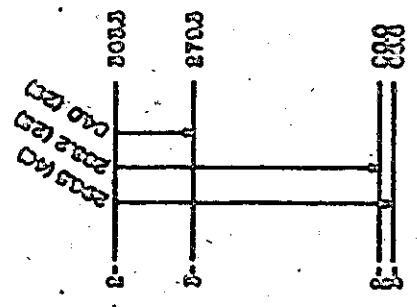
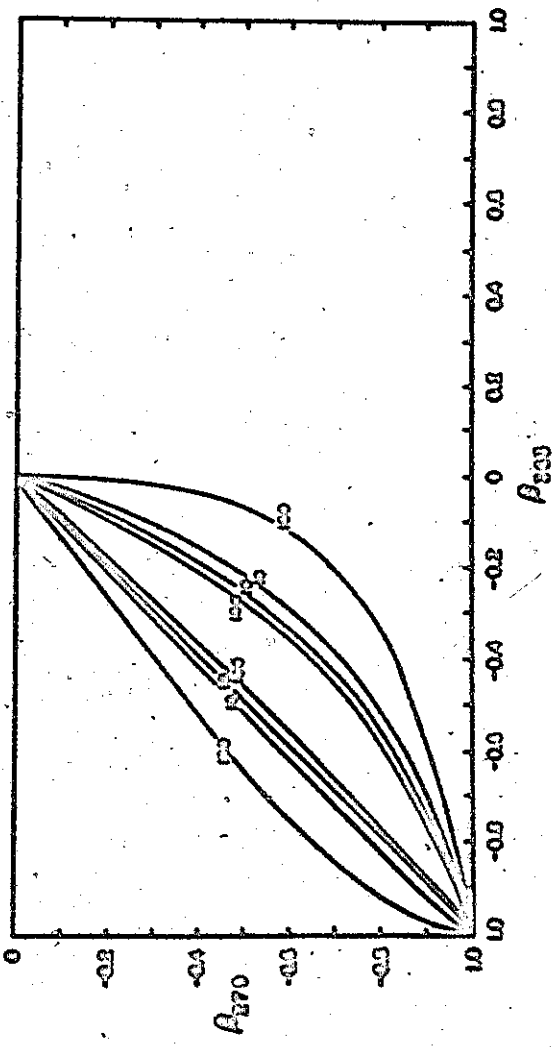
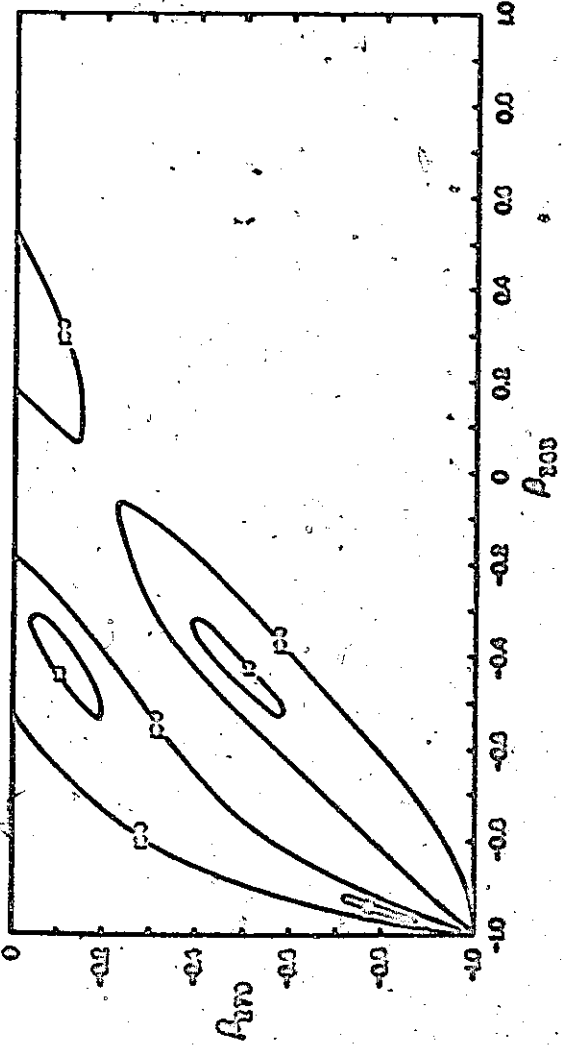
the branching γ rays, so that the initial level, and those to which it branched, involved only two different spin values. (The branching ratios were appropriately scaled.) In such a case only two variables had to be considered on account of normalization and orthogonality requirements. Values of χ^2 for each combination considered were found by varying the amplitudes over the allowed range. The χ^2 dependences are shown in Fig. 4.4.

The approximate wave vectors found from Fig. 4.4 for each of the states were then employed as initial estimates in a final search in which all wave vectors were varied simultaneously to minimize χ^2 for all branching ratios. In the case of unobserved branches, their contributions to χ^2 were found by assuming the intensities to be zero and taking upper limits as the uncertainties. The 1^- state at 250 keV, however, was not initially considered in the search since it imposes no constraint on the wave vectors of the other states. Once the five amplitudes (for $J=2, 3, 4, 5$ and 6) were determined from the ten experimental ratios, the 113 keV γ ray branch to the 250 keV state was included in a search in which the wave vector of this state alone was varied.

Two sets of amplitudes, given in Table 4.4, were found to give approximately the same value of χ^2 . These solutions correspond most closely to the wave vectors extracted from the proton transfer experiments. Other solutions may also exist for appreciably different amplitudes for some of the states. For example, one can obtain an equally good fit to the experimental branching ratios by taking $|\alpha| = 0.99$ and $|\beta| = 0.17$ for the 250 keV state, without modifying

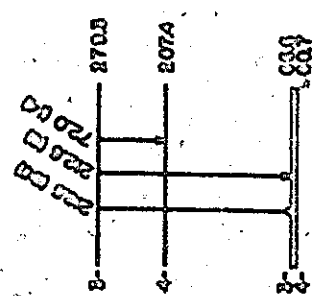
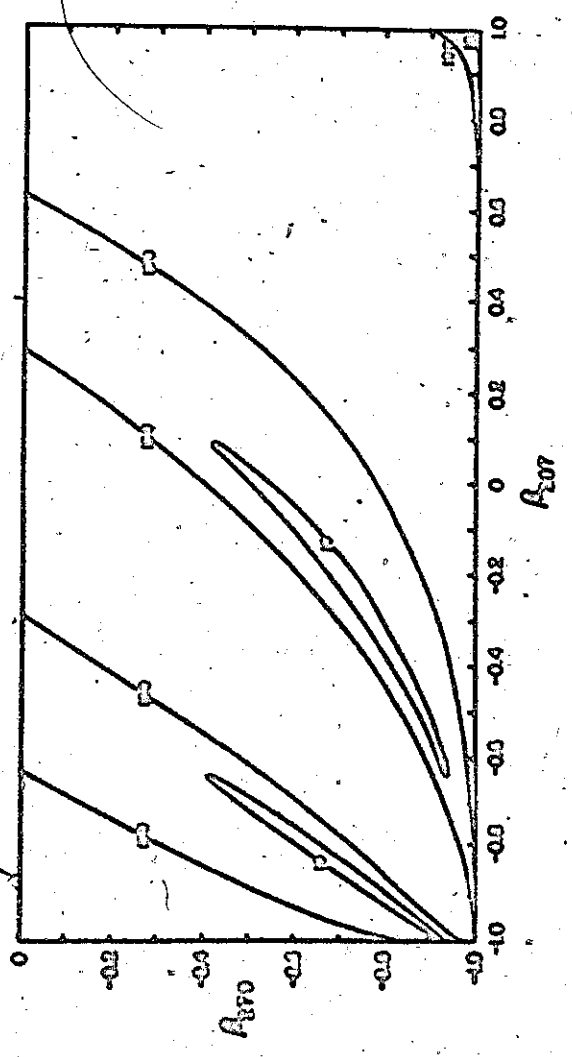
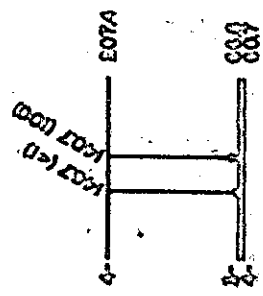
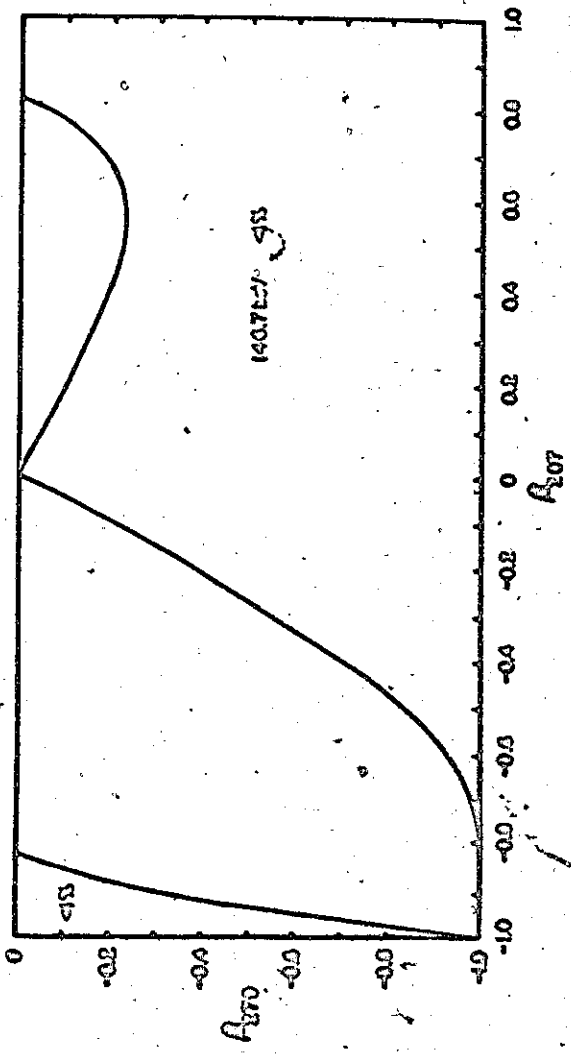
Fig. 4.4

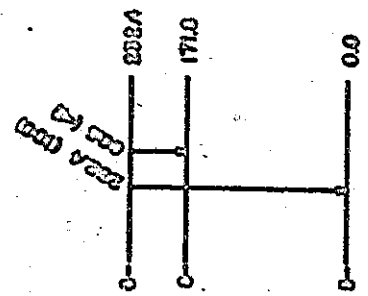
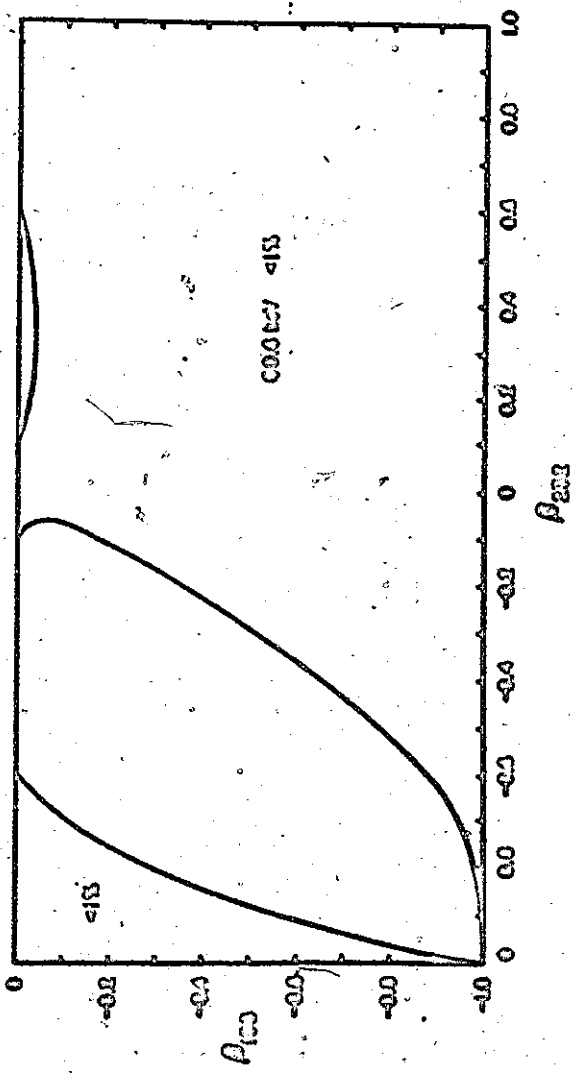
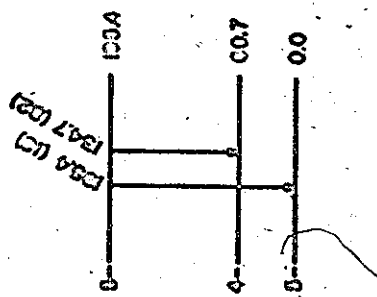
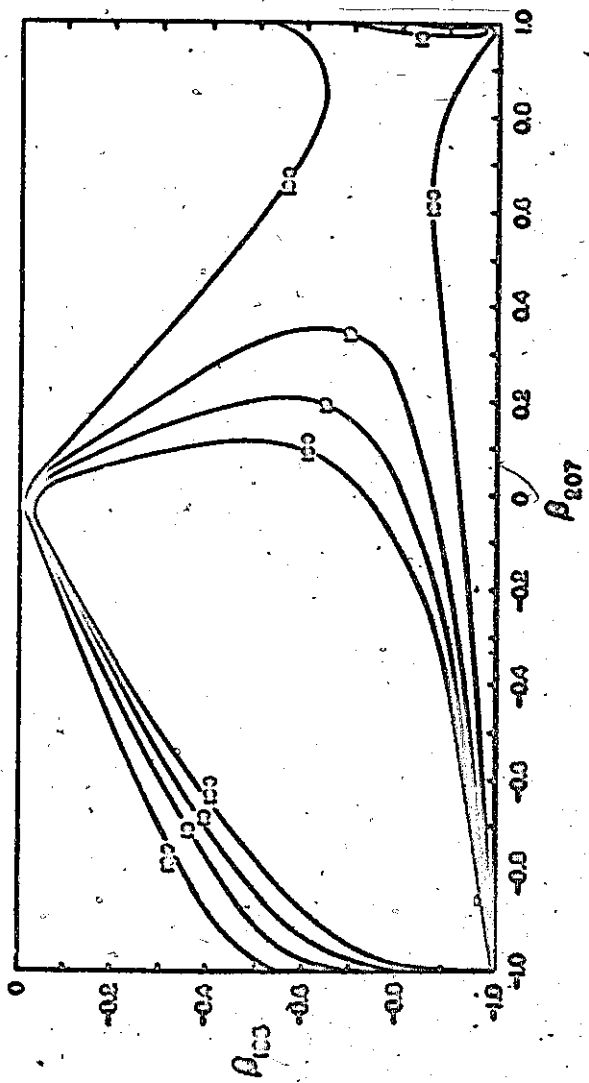
χ^2 plots for branching ratios in ^{144}Pu . For pairs of levels with the same spin, the β amplitudes of only one of the levels is plotted, since these determine the amplitudes of the other levels.



16







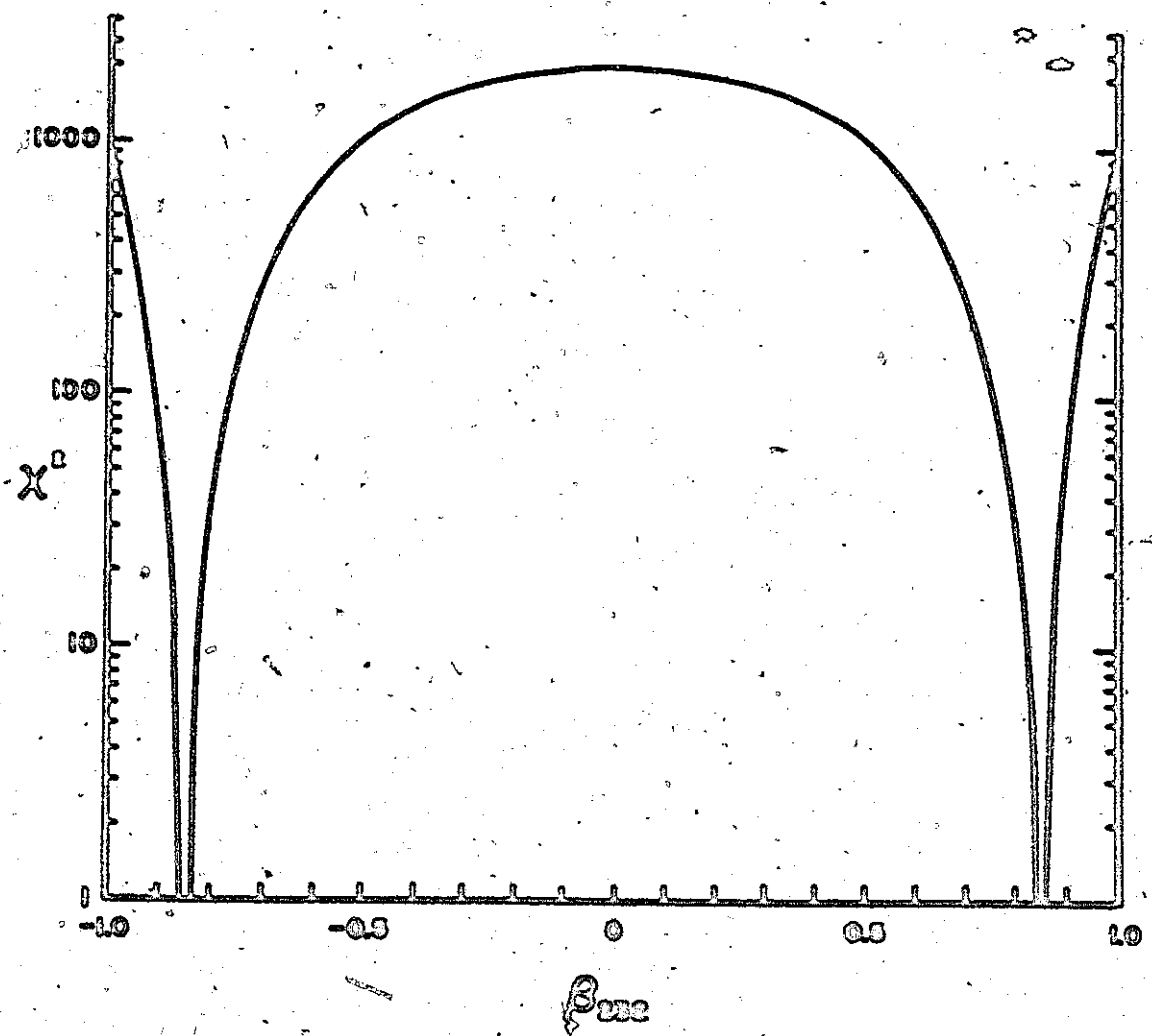
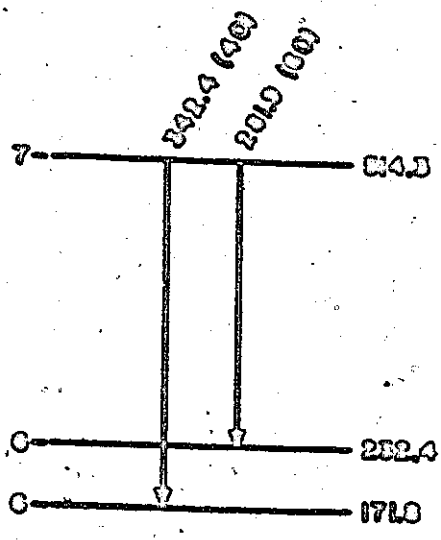


Table 4.4
 Comparison of wave vectors
 deduced from the proton transfer studies,
 and those determined from the
 experimental γ ray branching ratios

Energy (keV)	J^π	Proton Transfer Studies		Branching Ratio Analysis			
		$ \alpha $	$ \beta $	Solution I		Solution II	
				$ \alpha $	$ \beta $	$ \alpha $	$ \beta $
0.0	5^-	1.0(1)	0.0(3)	~ 1.0	0.0032	~ 1.0	0.0050
60.7	4^-	>0.84	<0.55	~ 1.0	0.010	~ 1.0	0.0022
66.6	3^-	>0.84	<0.55	0.90	0.44	0.90	0.44
80.0	2^-	>0.84	<0.55	0.98	0.20	0.98	0.20
171.8	6^-	0.87(8)	0.50(13)	0.85	0.52	0.85	0.52
195.4	5^-	0.39(14)	0.92(5)	0.0032	~ 1.0	0.0050	~ 1.0
207.4	4^-	0.45(11)	0.89(5)	0.010	~ 1.0	0.0022	~ 1.0
232.4	6^-	0.36(12)	0.93(5)	0.52	0.85	0.52	0.85
249.9	1^-	0.50(10)	0.87(6)	0.76	0.65	0.76	0.65
279.3	3^-	0.47(10)	0.88(6)	0.44	0.90	0.44	0.90
363.3	2^-	0.26(11)	0.96(3)	0.20	0.98	0.20	0.98
514.4	7^-	<0.22	>0.97	0.0	1.0	0.0	1.0

As indicated in section 4.2a the 342.38 keV line may be a doublet, in which case the $J=6$ wave vectors would have to be modified.

the amplitudes of the other states given in Table 4.4. For each of the tabulated solutions there are four possible sets of phases, giving the same theoretical branching ratios. The allowed phases are shown in Table 4.5. A comparison of the experimental and theoretical branching ratios, presented in Table 4.6, shows reasonably good agreement except for some of the very weak branches.

The agreement between the calculated and experimental branching ratios is much better for ^{142}Pr (Kern et al. 1968) than for ^{144}Pm . This is most likely due to the fact that the configuration mixing between the $2d_{5/2}$ and $1g_{7/2}$ proton states is much smaller in ^{144}Pm . This is not surprising since the splitting between these single particle states is approximately twice as great in ^{144}Pm . As a result, a relatively small admixture of additional configurations in the low lying levels of ^{144}Pm would play an important role in determining those decay properties. This was also found in the case of ^{140}La (Jurney et al. 1970).

4.2h Ground State Magnetic Moment

Employing the techniques of low temperature nuclear orientation, Shirley et al. (1961) determined the ground state magnetic moment of ^{144}Pm . From their measured value of $|\mu| = 1.63(14) \mu_N$ for $J=5$, they concluded that the $2d_{5/2}$ proton configuration was favoured, although a strong $1g_{7/2}$ admixture was likely in view of the proximity of these two states in the odd promethium isotopes.

Table 4.5

Relative Phases for β Amplitudes

Energy (keV)	J^π	Sign β							
		Solution I				Solution II			
0.0	5^-	+	+	+	+	+	+	+	+
60.0	4^-	+	+	+	+	-	-	-	-
66.6	3^-	+	+	-	-	+	+	-	-
80.0	2^-	+	+	-	-	+	+	-	-
171.8	6^-	-	+	-	+	-	+	-	+
195.4	5^-	-	-	-	-	-	-	-	-
207.4	4^-	-	-	-	-	+	+	+	+
232.4	6^-	+	-	+	-	+	-	+	-
249.9	1^-	+	+	-	-	+	+	-	-
279.3	3^-	-	-	+	+	-	-	+	+
363.3	2^-	-	-	+	+	-	-	+	+
514.4	7^-	+	+	+	+	+	+	+	+

Table 4.6

Comparison of calculated and experimental branching ratios

Initial State (keV)	J_i^{π}	Final State (keV)	J_f^{π}	Branching Ratios		
				Experimental	Calculated	
				Solution I	Solution II	
514.4	7^-	171.8	6^-	40.1(1.9)	40.1	40.1
		232.4	6^-	59.9(1.9)	59.9	59.9
363.3	2^-	66.6	3^-	40.6(2.1)	41.3	41.8
		80.0	2^-	22.7(1.7)	15.1	14.8
		249.9	1^-	10.7(0.7)	10.6	10.6
		279.3	3^-	26.0(1.9)	33.0	32.8
279.3	3^-	60.7	4^-	61.6(1.6)	71.0	71.7
		66.6	3^-	4.52(52)	0.71	0.69
		80.0	2^-	22.7(1.2)	23.1	22.6
		207.4	4^-	11.2(1.0)	5.2	5.0
232.4	6^-	0.0	5^-	100	99.3	99.3
		171.8	6^-	<1*	0.72	0.72
207.4	4^-	0.0	5^-	<1	0.21	0.11
		60.7	4^-	<1	0.002	<0.001
		66.6	3^-	100	99.8	99.9
195.4	5^-	0.0	5^-	18.3(1.0)	18.2	18.3
		60.7	4^-	81.7(1.0)	81.8	81.7

* This branch would not have been resolved from the 60.74 keV γ ray. The limit has been estimated from the 171.8 keV gate set in the (a,n) coincidence experiments.

If the neutron and proton orbits contain at most one unpaired nucleon, then one can express the magnetic moment in terms of these configurations as

$$\mu_J = \alpha_J^2 \mu(\pi 2d_{5/2} \nu 2f_{7/2} : J) + (1 - \alpha_J^2) \mu(\pi 1g_{7/2} \nu 2f_{7/2} : J) \quad 4.2$$

where $\mu(\pi 2d_{5/2} \nu 2f_{7/2} : J)$ denotes the magnetic moment for a state with spin J arising from the $\pi 2d_{5/2} \nu 2f_{7/2}$ configuration only, $\mu(\pi 1g_{7/2} \nu 2f_{7/2} : J)$ being defined in a similar way. Using the experimentally measured magnetic moments of the neighbouring odd A nuclei, equation 4.2 becomes

$$\mu_{J=5} = 2.21 \alpha^2 + 1.23 (1 - \alpha^2) \text{ m.m.}$$

Taking $\mu_{J=5} = +1.68(14) \text{ m.m.}$ gives $\alpha^2 = 0.46(14)$, in strong disagreement with the present work.

A possible reason for the discrepancy may be the simplicity of the model which has been employed to explain the proton transfer and γ ray data. Other components which would be present in the ground state wave function include those from the $\pi 2d_{3/2} \nu 2f_{7/2}$ and $\pi 1g_{7/2} \nu 3p_{3/2}$ configurations. Since the $\pi 2d_{3/2}$ state occurs at an excitation of ~ 1400 keV in ^{143}Pm , possible admixtures of the former configuration are not expected to be significant. However, to explain the magnetic moment measurement one would then have to postulate $>20\%$ admixtures of the latter configuration. The (d,p) reaction to ^{140}La and ^{142}Pr would be sensitive to even small $3p_{3/2}$ components in the low lying levels. The observed angular distributions for these states are consistent with pure $l=3$ transfers (Korn 1967, 1968). Large admixtures of $\nu 3p_{3/2}$ in the ground state of ^{144}Pm would thus seem unlikely. Assuming an almost pure $\pi 2d_{5/2} \nu 2f_{7/2}$ ground state,

in agreement with the proton transfer results, it is surprising that the experimental branching ratios can be reasonably well reproduced, but not the ground state magnetic moment (also an H1 matrix element).

Another possibility which cannot be excluded, is the uncertainty in the measured value of the magnetic moment. If its value were larger by ~20% then all the experimental data would be consistent with the relatively simple shell model. In light of the considerable uncertainties in estimating the parameters required for the magnetic moment measurement such an increase may not be unreasonable. A more up-to-date determination of the magnetic moment would be very useful in this respect.

4.3 Energy Levels Above 600 keV

4.3a Construction of High Energy Scheme

The experimental level scheme, deduced from the proton transfer and γ ray studies, is shown in Fig. 4.5. Nearly all the levels have been identified in both the ($^3\text{He},d$) and (α,t) reactions. The decay modes for some of the states were found from γ - γ coincidence experiments, and others were deduced from energy fits alone. The γ ray and spin assignments for this scheme are much less certain than those for the low energy scheme, on account of the limited data available.

In the case of the low energy scheme the γ ray intensity ratios exhibited a strong dependence on the spins of the de-exciting levels. This dependence has been used to suggest spins for the higher excited states. γ rays which were in coincidence showed that the

Fig. 4.5

Proposed high energy scheme of ^{144}Pr (>600 keV).
Tentative λ value assignments are also included for states
>600 keV.

dependence does not change drastically for the high energy transitions. For example, the 669 and 327 keV γ rays have $(p,n)/(a,n)$ intensity ratios of ~ 0.25 , implying a $J=7$ assignment. Coincidence data show that these γ rays follow the decay of the 841 keV state to the 514 keV ($J=7$) and 171 keV ($J=6$) states. Also from the coincidence data, the 1080 keV state decays to the 172 keV state via a 908 keV γ ray with an intensity ratio consistent with $J=5$ or 6. The deduced spins for the 841 and 1080 keV states are thus plausible, since the 669, 327 and 908 keV γ rays could be fast M1, E1 or E2 transitions.

The 218 and 1058 keV coincident γ rays establish a level at 1337 keV which decays to the 279 keV ($J=3$) state by the 1058 keV γ ray. Since the 279 keV state has $J=3$ this level must have $1 \leq J \leq 5$. The $(p,n)/(a,n)$ intensity ratio is 4.0 which is consistent with a spin of 4, 5 or 6, so one concludes that the 1337 keV state has $J=4$ or 5.

It is thus reassuring that the spins of the 841, 1080 and 1337 keV levels, predicted on the basis of γ ray intensity ratios, are consistent with low multipolarity (≤ 2) for the observed γ rays. All γ rays observed in both the (a,n) and (p,n) reactions have intensity ratios lying between 0.1 and 1.0, approximately the same limits observed for γ rays in the low energy scheme. The remaining γ rays had intensity ratio limits which were also in this range. (The possible limits set by the experimental data are ~ 0.01 and ~ 100 .) Hence spin assignments for the high energy levels, deduced from γ ray intensity ratios would appear to be possible.

The lines at 809 and 819 keV are seen strongly just above the (p,n) threshold. They are present at proton beam energies ≥ 4.5 MeV but absent at energies ≤ 4.15 MeV. Since the ground state threshold is ~ 3.2 MeV, these γ rays must originate from levels ≤ 1300 keV. Further, since the strongest γ rays observed just above threshold presumably arise from low spin states, the lines at 809 and 819 keV must feed similar states at excitations ≤ 500 keV. Their (p,n)/(α ,n) intensity ratio also indicates low spin. The 250, 279 and 363 keV states must be ruled out since the lines would have been present in the coincidence windows (assuming states are not isomeric). It is assumed, therefore, that the 809 and 819 keV lines feed the low spin states at 67 and 80 keV from levels at 875 and 899 keV observed in the particle work. Although lines feeding the levels at 80, 66 and 60 keV states would be in coincidence with the 60.7 keV γ ray, the small detection efficiency and high internal conversion coefficient (~ 6.6) for a 60.7 keV M1 transition, would make it difficult to observe such lines in coincidence. The 809 keV line could also be a ground state transition from a level which is not populated in the proton transfer work. The spin of such a level could be 4, or possibly 3 if the transition were E2.

Parity assignments have been made for some of the levels which were resolved in both the ($^3\text{He},d$) and (α,t) reactions. They were deduced from the ($^3\text{He},d$) and (α,t) cross section ratios given earlier in Chapter II (Fig. 2.9). Levels which were consistent with $l \leq 2$ were assumed to have -ve parity ($l=1$ is unlikely from shell

model considerations).

Many of the unplaced γ rays must originate from levels which are not populated in the proton transfer experiments. It is thus difficult to place these transitions uniquely in the level scheme.

4.3b Interpretation of High Energy Scheme

On the basis of the shell model, the important proton states in the high energy scheme are expected to be the $3s_{1/2}$, $1h_{11/2}$ and $2d_{3/2}$ states. These states have been identified experimentally in the odd proton $N=82$ nuclei (Wildenthal et al. 1971). The proton transfer reactions would thus populate states arising from the coupling of these proton states to the $2f_{7/2}$ neutron state. The configurations give rise to the following levels

$$\begin{aligned} \pi 3s_{1/2} \nu 2f_{7/2} & : J=3,4 \text{ with negative parity} \\ \pi 1h_{11/2} \nu 2f_{7/2} & : J=2 \text{ to } 9 \text{ with positive parity} \\ \pi 2d_{3/2} \nu 2f_{7/2} & : J=2 \text{ to } 5 \text{ with negative parity.} \end{aligned}$$

Hence the observed states with $J > 5$ must arise from the $\pi 1h_{11/2} \nu 2f_{7/2}$ configuration only, and have $l=5$. The states at 841 and 948 keV are consistent with this assignment, although the proposed level at 836 keV could modify the cross section ratio and the predicted l value for the 841 keV state.

The low spin states at 876 and 899 keV can also be explained in terms of the configurations already mentioned. The 876 keV state, which has $l < 2$, may arise from either the $\pi 3s_{1/2} \nu 2f_{7/2}$ or the $\pi 2d_{3/2} \nu 2f_{7/2}$ configurations (or both), while the 899 keV state would correspond to the 2^+ member of the $\pi 1h_{11/2} \nu 2f_{7/2}$ configuration to

account for its $l=4, 5$ assignment. The 6^+ state from the latter configuration may be the 1080 keV state, which is strongly populated in the $(^3\text{He},d)$ and (α,t) reactions. The l value of the 1104 keV state would then have to be ≤ 2 to account for the $(^3\text{He},d)/(\alpha,t)$ ratio for both states.

In addition to levels containing different proton states, the (α,n) and (p,n) reactions can also populate levels arising from different neutron states. The (d,p) angular distributions measured by Kern et al. (1967, 1968) indicate the presence of $3p_{3/2}$ neutron states at excitation energies >600 keV in ^{140}La and ^{142}Pr . The lowest lying levels from such configurations are

$$\begin{aligned} \pi 2d_{5/2} \nu 3p_{3/2} & : J=1 \text{ to } 4 \text{ with negative parity} \\ \pi 1g_{7/2} \nu 3p_{3/2} & : J=2 \text{ to } 5 \text{ with negative parity.} \end{aligned}$$

The identification of these levels is very difficult with the limited data available. The 836 and 1337 keV levels, which were not identified in the proton transfer experiments, both have spin assignments of 4 or 5, and are thus consistent with states containing a $\nu 3p_{3/2}$ admixture. Although the proposed high energy scheme must be regarded as tentative, it is not inconsistent with simple shell model predictions.

4.4 Shell Model Calculations

4.4a Introduction

As described in Chapter I, the low lying levels of the odd-odd $N=83$ nuclei are well suited to shell model studies. Theoretical interpretations of this series of nuclei must account for the level

energies, spins, parities and electromagnetic properties of the many (>40) observed states in these nuclei. Following the experimental investigation of ^{140}La (Kern et al. 1967), detailed calculations were made by Struble (1967) and later by Heyde and Brussaard (1968).

Struble performed quasiparticle model calculations employing a finite range, two body, central force as the residual interaction in a relatively large configuration model space ($\pi 2d_{5/2}$, $\pi 1g_{7/2}$, $\pi 2d_{3/2}$, $\nu 2f_{7/2}$, $\nu 3p_{3/2}$, $\nu 2f_{5/2}$). The calculation of Heyde and Brussaard was performed in terms of the unified model in intermediate coupling, where three single particle configurations ($\pi 2d_{5/2}$, $\pi 1g_{7/2}$, $\nu 2f_{7/2}$) were coupled to a vibrating core (^{138}Ba). The results of both calculations are in reasonable agreement with the level scheme of ^{140}La .

More recently the N=82 nuclei were extensively studied both experimentally and theoretically by Wildenthal (1969,1971). The use of a surface delta type two body interaction (Green and Moszkowski 1965) met with considerable success in describing the properties of both the odd-even and the even-even nuclei. Calculations by Hussain (1973) showed that such an interaction can also give a good description of the odd-odd nucleus ^{142}Pr . In light of the experimental data for ^{140}La , ^{142}Pr and ^{144}Pm , further calculations have been undertaken using the Oak Ridge Shell Model Code, adapted by D. Bohan for use with the CDC6400 at McMaster. The calculations are discussed in the following section.

4.4b The Odd Odd N=83 Nuclei

In order to assess the validity of a surface delta interaction as an effective interaction, calculations were performed for all odd-odd N=83 nuclei. Retaining the simplicity of the two configuration model, the active protons beyond the doubly magic $^{132}_{50}\text{Sn}_{82}$ were allowed to occupy the $1g_{7/2}$ and $2d_{5/2}$ orbits only. The odd neutron, confined to the $2f_{7/2}$ orbit, was coupled to proton configurations of the type

$$(1g_{7/2})_0^{n_1} (2d_{5/2})_{5/2}^{n_2} \text{ and } (2d_{5/2})_0^{n_2} (1g_{7/2})_{7/2}^{n_1},$$

where n_1 is the number of protons in the $1g_{7/2}$ orbit, and n_2 is the number in the $2d_{5/2}$ orbit. All possible values of n_1 and n_2 were considered in this lowest seniority scheme.

To carry out such a calculation one must first choose two strength parameters to define the two body surface delta interaction (one strength parameter for each of the possible isospin values (T=0 or 1) of the interacting pair), and also the single particle energy splitting between the $1g_{7/2}$ and $2d_{5/2}$ proton orbits. From the work of Wildenthal, the most appropriate values are; 0.520 MeV for the energy splitting, and 0.383 MeV for the T=1 strength parameter (A_1). These values were obtained from a least squares fit to 40 energy levels of known J^π in the N=82 nuclei from A=136-145. The only remaining parameter, the T=0 strength (A_0), was given the values 0.2, 0.3, 0.4, 0.5 and 0.6 MeV in the present calculations. By restricting the protons and neutrons to different orbits, the isospin formalism becomes redundant. However, since the residual two

body force is isospin dependent, matrix elements which differ only in the isospin quantum number, will generally have different values. Matrix elements of this type were replaced by the average values for $T=0$ and $T=1$.

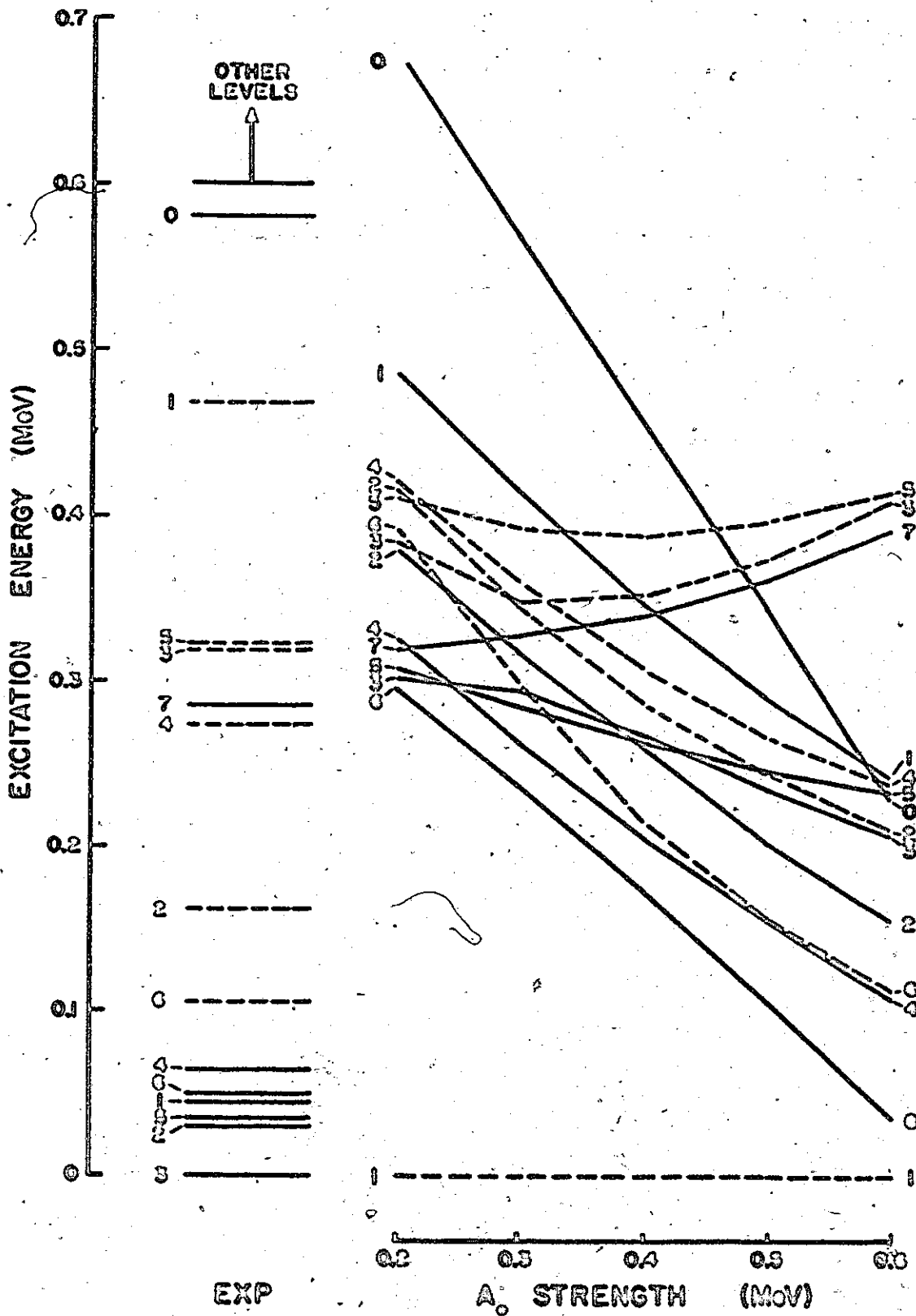
The calculated spectra for ^{140}La , ^{142}Pr and ^{144}Pm are shown in Fig. 4.6. In order to estimate the most appropriate $T=0$ strength, for each of the nuclei the root mean square (RMS) energy deviation was calculated for the different values of A_0 , assuming an energy correspondence between theoretical and experimental levels of a given spin. The absolute excitation energies were adjusted in each case to minimize the RMS deviation. The results, summarised in Fig. 4.7, indicate that the most appropriate value of the $T=0$ strength for ^{140}La , ^{142}Pr and ^{144}Pm is approximately the same as the $T=1$ strength of 0.383 MeV. The calculation for ^{140}La shows an RMS deviation of 116 keV in contrast to 90 keV from Struble's calculation and an estimated 80 keV from the work of Heyde and Brussaard. The comparison is, however, very favourable when one considers that in Struble's calculation, employing a nine-configuration model space, five free parameters were adjusted to best fit the ^{140}La spectrum. In the calculation of Heyde and Brussaard seven adjustable parameters were used.

It is interesting to note that in ^{142}Pr and ^{144}Pm $J=1$ and 0 states are predicted to be well above the other levels arising from the $\pi 2d_{5/2} \nu 2f_{7/2}$ and $\pi 1g_{7/2} \nu 2f_{7/2}$ configurations. Experimentally this would also appear to be the case since these spins are the only two which have not been identified in ^{142}Pr and ^{144}Pm . According to

Fig. 4.6

Calculated spectra for ^{140}La , ^{142}Pr and ^{144}Pm , for different $T=0$ strengths, are compared with the experimental level schemes. Solid lines and dashed lines indicate a predominant $1g_{7/2}$ and $2d_{5/2}$ proton component respectively. Experimental levels which contain an admixture $>40\%$ are denoted in such a way as to reproduce the theoretical level ordering.

^{140}La



^{144}Pm

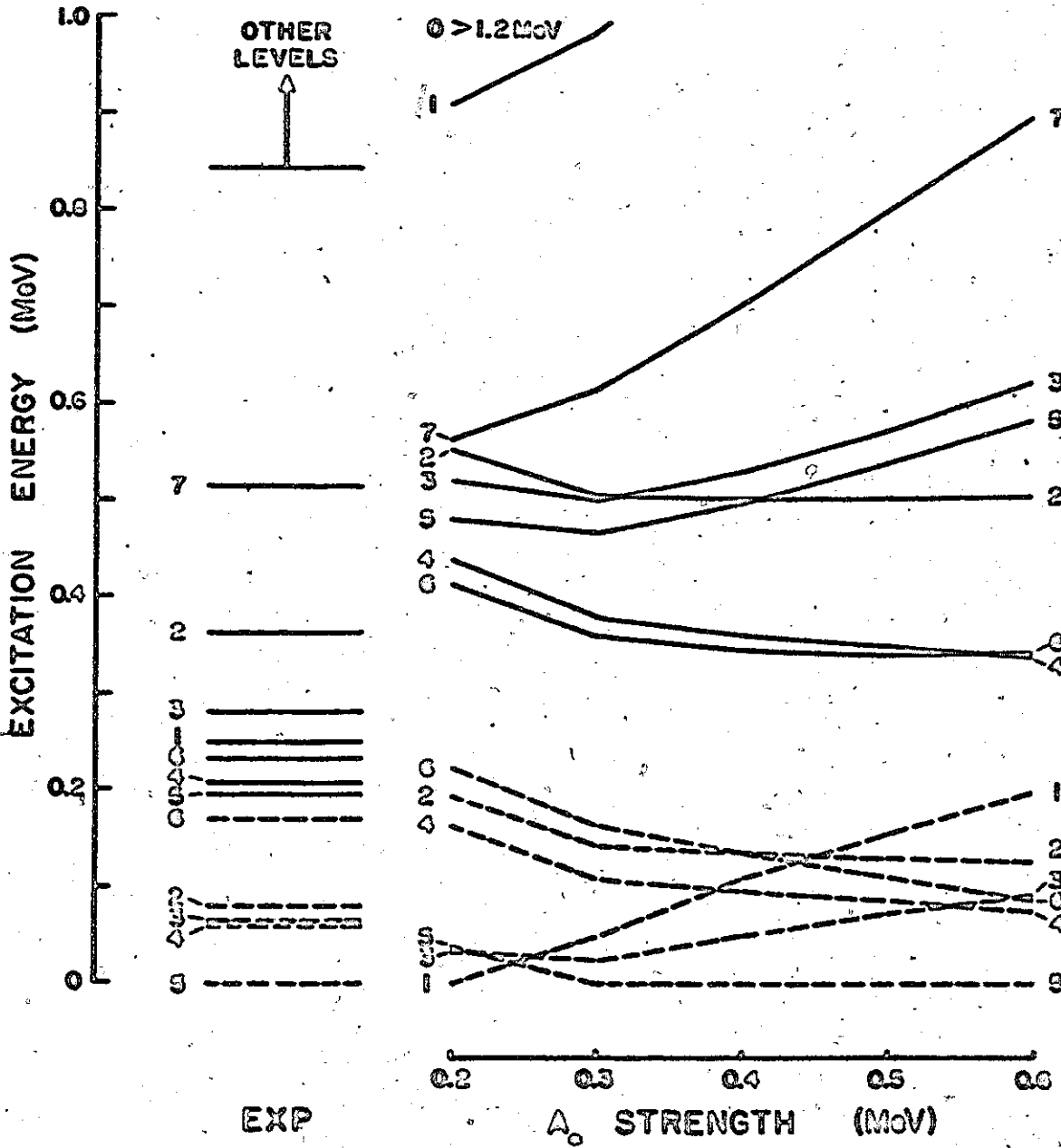
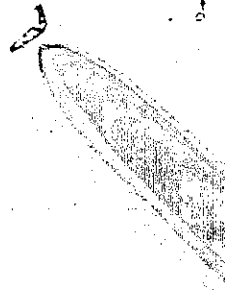
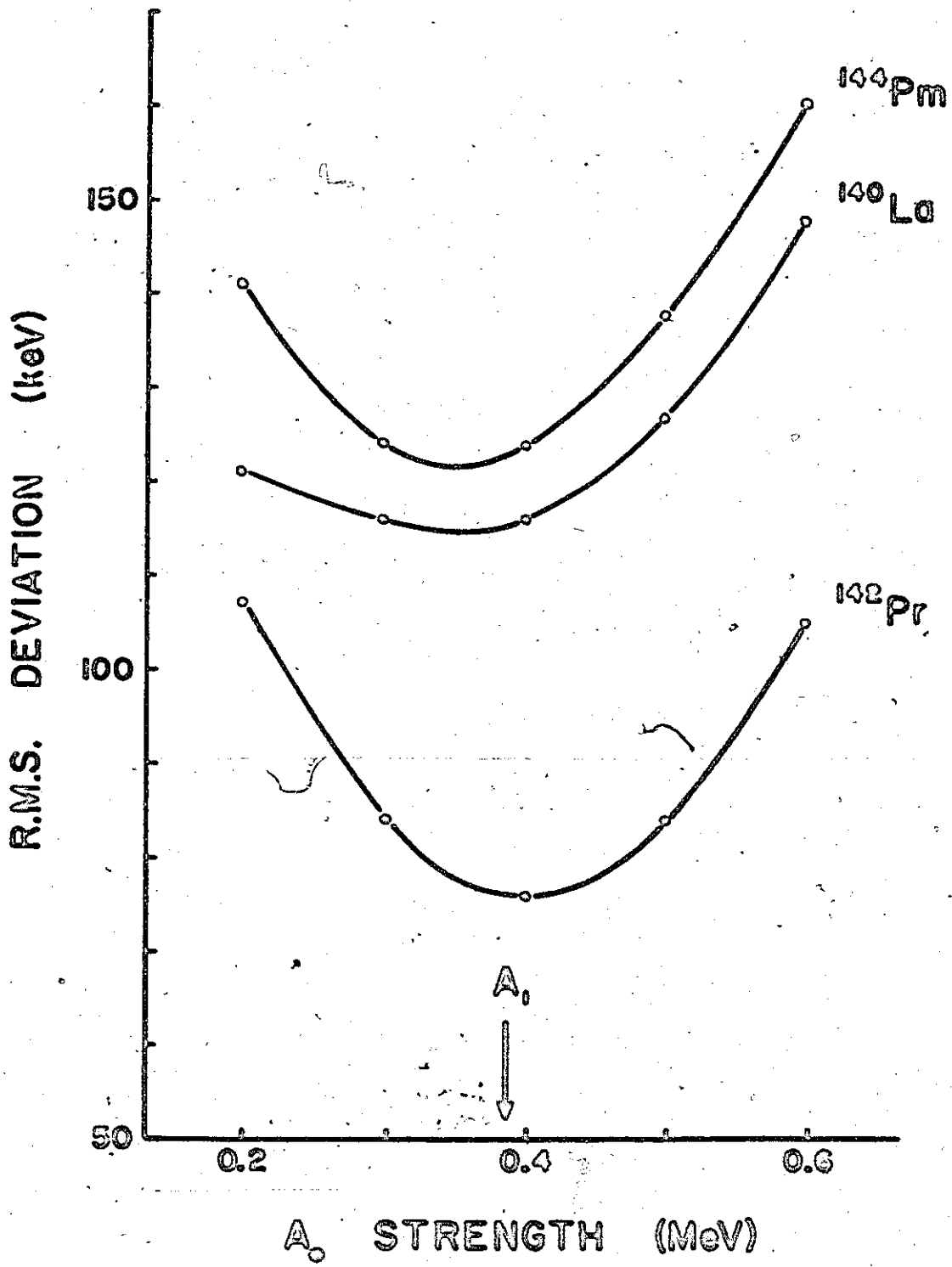


Fig. 4.7

Root mean square energy deviation for the theoretical and experimental spectra of ^{140}La , ^{142}Pr and ^{144}Pm for different choices of the $T=0$ strength.





the calculation these states would occur at energies where the level density is known, experimentally, to be high. In ^{140}La and ^{142}Pr the lower $J=1$ states are depressed considerably in energy, so as to be the ground states for these nuclei, although the calculation correctly predicts the 5^- ground state of ^{144}Pm .

A more realistic test of the model is provided by a comparison of the computed wave functions with those derived from experiments. For states of a given spin, one makes a correspondence between those which exhibit similar theoretical and experimental admixtures. For most of the levels, however, the wave function correspondence is just the same as the energy correspondence, except for the $J=3$ and 4 levels in ^{142}Pr , and the $J=1$ states in ^{140}La and ^{144}Pm . (The RMS energy deviation in this case is actually smaller for the SDI calculation than for Struble's calculation.) The computed configuration mixing amplitudes and those measured in the present work for ^{144}Pm , are shown in Table 4.7.

Although the agreement for ^{140}La and ^{142}Pr is not as good as that for ^{144}Pm , Struble's calculation for ^{140}La indicates $\pi 2d_{5/2} \nu 2f_{7/2}$ admixtures which are very similar to those from the present SDI calculations.

The most serious problem is posed by the $J=1$ states. Theoretically the lower $J=1$ state has a predominant $\pi 2d_{5/2} \nu 2f_{7/2}$ and is depressed in energy, whereas experimentally the lowest $J=1$ states in ^{140}La and ^{144}Pm contain a predominant $\pi 1g_{7/2} \nu 2f_{7/2}$ component. In ^{140}La , where both $J=1$ states have been found, the predicted energy

Table 4.7

Theoretical and experimental configuration mixing amplitudes for ^{144}Pm . The amplitudes α^2 for the $(\pi 2d_{5/2} \nu 2f_{7/2})$ configuration are given, the $(\pi 1g_{7/2} \nu 2f_{1/2})$ amplitudes being $(1-\alpha^2)$.

Energy (keV)	Spin J	Configuration Mixing Amplitude (α^2)	
		Proton transfer Studies	Theoretical ($A_0=0.4$ MeV)
0	5	1.0(1)	0.96
61	4	>0.70	0.87
67	3	>0.70	0.92
80	2	>0.70	0.94
172	6	0.75(15)	0.56
195	5	0.15(10)	0.04
207	4	0.20(10)	0.13
232	6	0.13(10)	0.44
250	1	0.25(10)	0.71
279	3	0.22(10)	0.08
363	2	0.07(6)	0.06
514	7	<0.05	0.0

splitting of ~ 360 keV compares favourably with the experimental splitting of 424 keV. However, the lower state has a calculated $\pi 2d_{5/2} \nu 2f_{7/2}$ component of 98% while experimentally it is $\sim 35\%$. Similar discrepancies are also found for the $J=1$ state in ^{144}Pm . One might argue that such disagreement is most likely a result of the highly truncated configuration space, and (or) the simple phenomenological force which has been used. At first, these explanations seem unlikely in light of the fact that a similar discrepancy occurs in Struble's calculations. Unfortunately the compositions of the wave functions from the unified model calculation of Heyde and Brussaard are not readily available. However, their computed (d,p) spectroscopic factor for the $J=1$ state at 467 keV shows the largest deviation from the experimental value. It was suggested by Struble that the $J=1$ discrepancy might be resolved by the inclusion of a tensor force. This seems very plausible since the work of Sliv and Kharitonov (1968) indicates that for $J=J_{\min}$ and $J=J_{\min}+1$ (where $J_{\min} = |j_p - j_n|$), the tensor force matrix elements can differ considerably from other matrix elements. Hence for both the $\pi 2d_{5/2} \nu 2f_{7/2}$ and $\pi 1g_{7/2} \nu 2f_{7/2}$ configurations the tensor force matrix elements for $J=1$ could be very important. The discrepancy thus seems to originate with the residual interaction. (Perhaps a simple J dependent term could be included in the SDI to modify matrix elements involving J_{\min} and $J_{\min}+1$.)

In conclusion, it is quite remarkable that such a simple interaction containing just one free parameter (if $A_0=A_1$), and employing a very simple configuration space, can not only describe the experimental data for the odd proton and the even-even $N=82$ nuclei,

but also accounts for most of the features in the odd-odd $N=83$
nuclei.

SUMMARY

An experimental investigation of the level structure of the odd-odd $N=83$ nucleus ^{144}Pm has been described. In particular the properties of the low lying levels have been studied in detail, and can be understood in terms of simple shell model configurations. At the present time, this work represents the only available data on the level scheme of this nucleus, and adds considerably to the known data for the series of odd-odd $N=83$ nuclei.

The $(^3\text{He},d)$ and (α,t) proton transfer reactions have been employed to independently extract spectroscopic factors and tentative spin assignments from general assumptions about the properties of neighbouring nuclei and the reaction mechanism. The method is a convenient alternative (and supplement) to standard angular distribution analysis in terms of DWBA theory, and could be extended to neutron and proton transfer studies of odd-odd nuclei in other regions of the periodic table.

The γ ray studies revealed interesting correlations between γ ray intensity ratios, measured in the (p,n) and (α,n) reactions, and nuclear spins. It would be profitable to study the limitations and validity of this technique for assigning nuclear spins, under a variety of conditions. Its application to states in regions of high level density could prove especially useful.

Theoretical calculations using a surface delta interaction in a highly truncated space give a good description of the low lying

states of ^{140}La , ^{142}Pr and ^{144}Pm , except for the $J=1$ states. It would thus be interesting to locate the "missing" $J=1$ states and establish their character. The proton pick-up reaction $^{143}\text{Nd}(d, ^3\text{He})^{142}\text{Pr}$ and further γ - γ studies of the (α, n) and (p, n) reactions leading to states in ^{142}Pr and ^{144}Pm could be useful in this respect. The γ ray studies would also allow the higher excited states to be investigated with a view to locating the +ve parity states arising from the $\pi 1h_{11/2} \nu 2f_{7/2}$ configuration. The properties of these states would further test the validity of the proposed residual interaction.

APPENDIX 1

Al.1 Level Schemes of ^{143}Pm and ^{145}Pm

Al.1a Introduction

Although it was not intended to study the odd-even nuclei ^{143}Pm and ^{145}Pm , sufficient information was obtained in the course of this work to justify reporting their level schemes. Earlier investigations of ^{143}Pm have included the proton transfer studies of Wildenthal et al. (1971), and Hansen et al. (1968). The ($^3\text{He},d$) and ($d,^3\text{He}$) angular distributions measured by Wildenthal et al. and the (t,α) angular distributions of Hansen et al. enabled the $2d_{5/2}$, $1g_{7/2}$, $3s_{1/2}$, $2d_{3/2}$ and $1h_{11/2}$ proton states to be identified. The decay properties of these states have been investigated using the $^{143}\text{Sm}(e,c)^{143}\text{Pm}$ reaction (de Frenne et al. 1968, Hesse 1969) and the $^{141}\text{Pr}(\alpha,2n)^{143}\text{Pm}$ reaction (Ejiri et al. 1972). The only previous studies of the level scheme of ^{145}Pm have involved the $^{145}\text{Sm}(e,c)^{145}\text{Pm}$ reaction in which the $2d_{5/2}$ and $1g_{7/2}$ states were observed (Brosi et al. 1959).

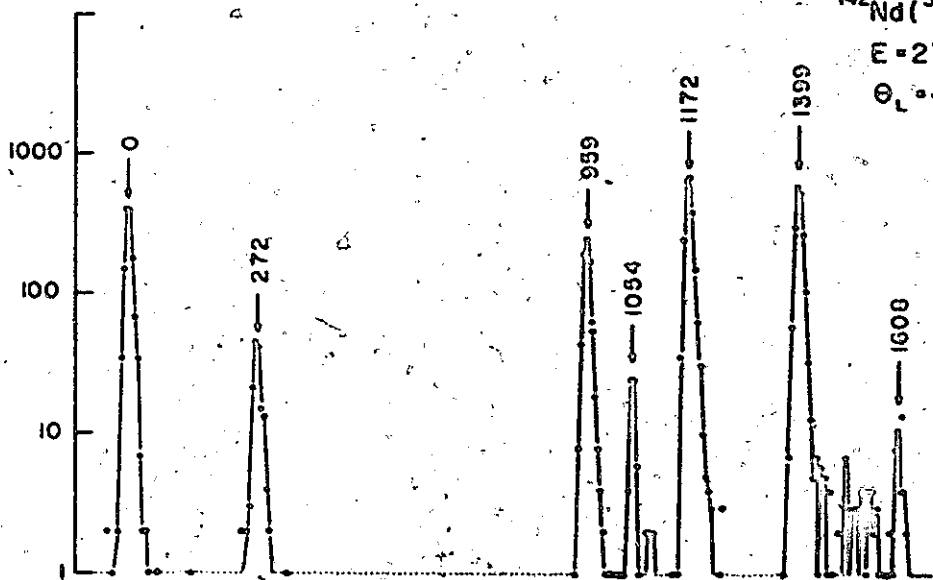
Al.1b Experimental Studies

($^3\text{He},d$) and (α,t) reactions to ^{143}Pm and ^{145}Pm were carried out at beam energies of, 27 MeV and laboratory angles of 42.5 and 50°. Spectra from the ($^3\text{He},d$) reactions are shown in Fig. Al.1. In the case of ^{143}Pm the expected single particle states are strongly populated, whereas the structure of ^{145}Pm reveals the presence of many

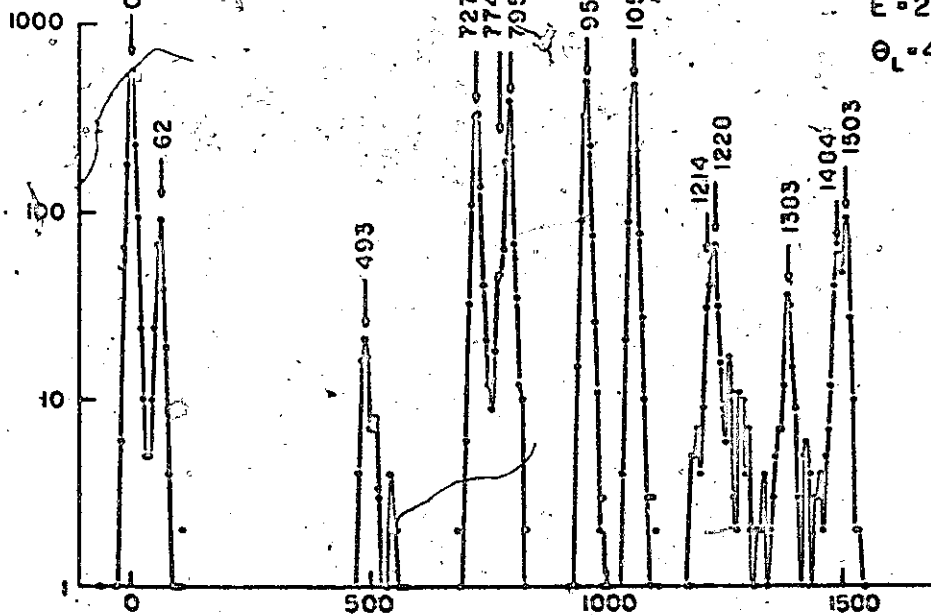
Fig. A1.1

Deuteron spectra from the $^{142}\text{Nd}(^3\text{He},d)^{143}\text{Pm}$ and
 $^{144}\text{Nd}(^3\text{He},d)^{145}\text{Pm}$ reactions.

COUNTS PER 0.25 mm STRIP



$^{142}\text{Nd}(^3\text{He},d)^{143}\text{Pm}$
 $E = 27 \text{ MeV}$
 $\theta_L = 42.5^\circ$



$^{144}\text{Nd}(^3\text{He},d)^{145}\text{Pm}$
 $E = 27 \text{ MeV}$
 $\theta_L = 42.5^\circ$

EXCITATION ENERGY (keV)

more states. The additional two neutrons in the $2f_{7/2}$ orbit have thus a profound effect on the observed states, particularly at an excitation of ~ 1 MeV. The states arising from the particle phonon-coupling are expected to be depressed more in ^{145}Pm than in ^{143}Pm , since the target nuclei ^{142}Nd and ^{144}Nd have phonon states at 1.5 and 0.7 MeV respectively. Such states, however, would not be expected to be populated with cross sections comparable to the single particle states. The measured excitation energies of ^{143}Pm and ^{145}Pm , presented in Tables A1.1 and A1.2, confirm earlier studies of these nuclei, and extend our knowledge of ^{145}Pm .

A1.1c l Value and Spin Assignments for ^{145}Pm

A comparison of the $(^3\text{He},d)$ and (α,t) cross section ratios for both ^{143}Pm and ^{145}Pm enable tentative l values and spins to be assigned to states in ^{145}Pm . The known l values for the ground state and first excited states in ^{145}Pm , and those identified in ^{143}Pm by Wildenthal provide calibration points for determining the l and Q dependence on the cross section ratio. This is shown in fig. A1.2.

The ratios for states which are weakly populated in both the $(^3\text{He},d)$ and (α,t) reactions cannot be considered reliable indicators of l values since multistep reaction processes may significantly modify the cross sections. For example, the $3/2^+$ state at 1054 keV in ^{143}Pm is shown by Wildenthal to have an $l=2$ angular distribution in the $(^3\text{He},d)$ reaction, but its cross section ratio measured in this work implies an $l \geq 5$ assignment. This state is very weakly populated in both the $(^3\text{He},d)$ and (α,t) reactions and cannot be a

Table A1.1.

Summary of level energies and
proton transfer cross sections for ^{143}Pm

Energy (keV)	Differential Cross Section ($\mu\text{b}/\text{str}$)		Energy Levels from Other Work			
	$(^3\text{He}, d)$ $\theta_L = 42.5^\circ$	(α, t) $\theta_L = 50^\circ$	Wildenthal et al. (1971)	Hansen et al. (1968)	de Frenne et al. (1968)	Hesse (1969)
0	509(52)	79(8)	0	0	0	0
*272(2)	64(8)	27(3)	270(5)	273(15)	272.9(2)	272.0(3)
959(2)	303(33)	172(18)	962(10)	964(15)		
1054(4)	9(3)	8(1)	1066(10)		1056.6(5)	1056.8(3)
1172(2)	920(94)	14(2)	1172(10)	1183(15)	1173.3(5)	1173.4(4)
					1341.0(1.0)	1342.9(8)
1399(2)	789(81)	22(3)	1402(12)	1409(15)	1403.5(5)	1403.4(4)
					1515.7(5)	1515.4(3)
1608(4)	11(2)	<10		1576(15)		
				1638(15)		

* Energy from the $^{141}\text{Pr}(\alpha, 2n)^{143}\text{Pm}$ reaction at $E_\alpha = 20$ MeV gives
272.069(25) keV.

The uncertainties in the cross sections allow for a systematic error of
~10%.

Table A1.2

Summary of level energies and
proton transfer cross sections for ^{145}Pm

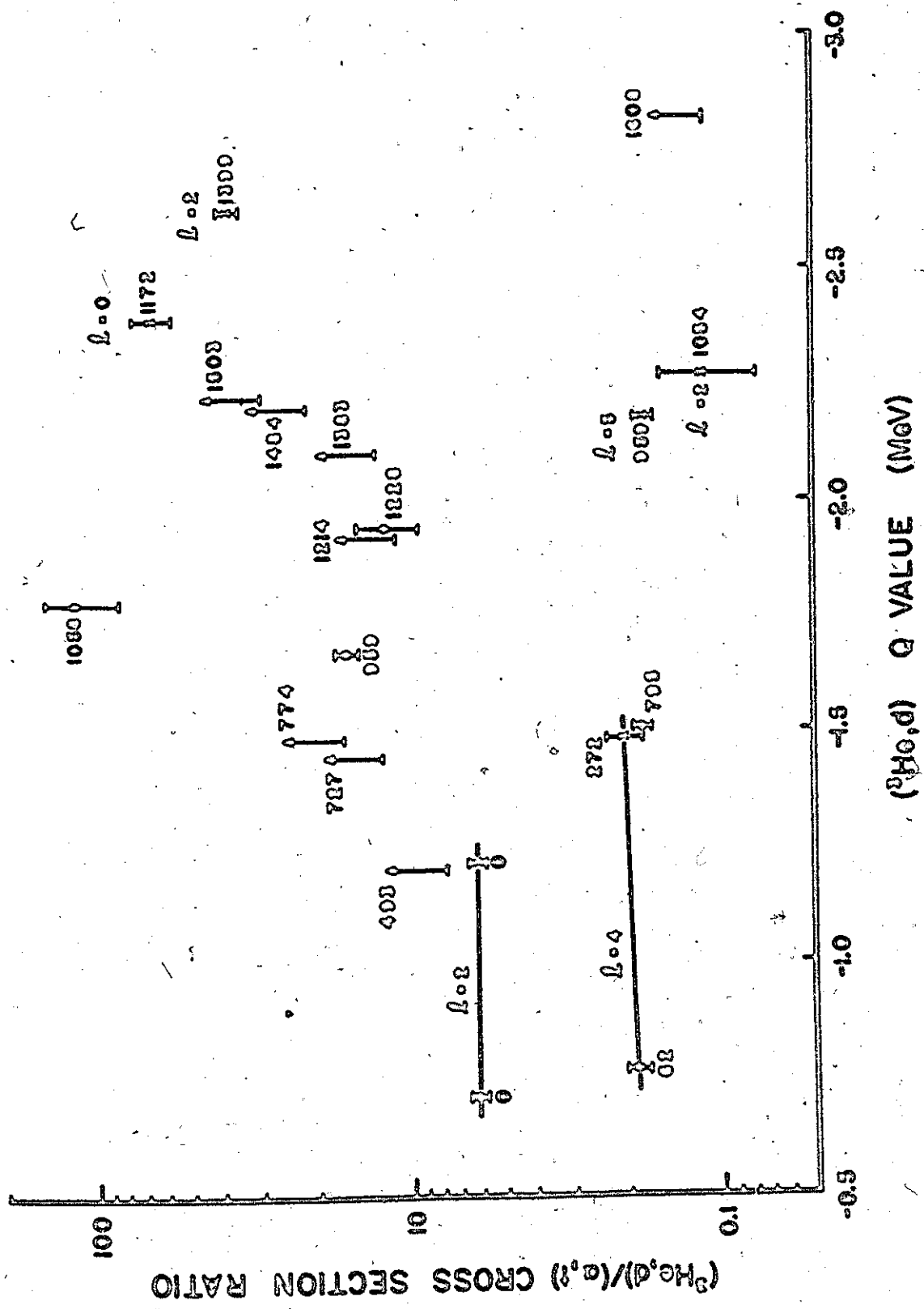
Energy (keV)	Differential Cross Section ($\mu\text{b}/\text{str}$)		Energy levels from other work Brosi Chiao & et al. Martin (1959) (1967)	
	$^3\text{He}, d$ $\theta_L = 42.5^\circ$	(α, t) $\theta_L = 50^\circ$		
0	591(61)	94(11)	0	0
62(2)	94(11)	49(6)	62	61.4
493(4)	23(4)	<3	485	495
727(3)	368(42)	<3		
774(3)	49(8)	<3		
795(2)	349(38)	196(20)		
959(2)	461(49)	29(4)		
1058(3)	467(52)	4(1)		
1214(4)	33(7)	<3		
1228(4)	60(9)	5(1)		
1383(3)	38(6)	<3		
1484(3)	62(8)	<3		
1503(3)	88(11)	<3		

Peaks with $^3\text{He}, d$ cross sections $< 8 \mu\text{b}/\text{str}$ are not included since they may be due to isotopic impurities in the ^{144}Nd target.

The uncertainties in the cross sections allow for a systematic error of $\sim 10\%$.

Fig. A1.2

($^3\text{He}, d$)/(α, t) cross section ratios for states in
 $^{143}\text{Pm}(X)$ and $^{145}\text{Pm}(O)$.



simple single particle state.

Whereas in ^{143}Pm most of the proton transfer strength is concentrated in only a few states, in ^{145}Pm there is appreciable splitting of this strength among many states. Apart from the ground state and first excited state, the levels at 959 and 795 are most strongly populated in both the $(^3\text{He},d)$ and (α,t) reactions. The most likely "single particle" assignments for these states are $3s_{1/2}$ or $2d_{3/2}$, and $1h_{11/2}$ respectively. It is clear however that the states in this region are strongly mixed so that the assignments must be considered tentative. $(^3\text{He},d)$ angular distributions and (p,n) studies of ^{145}Pm would be valuable in elucidating the structure of these states.

APPENDIX 2

A2.1 Q Values

In the present work the extraction of the spectroscopic factors and nuclear spins for ^{144}Pm depends on the differences in the Q values for the ($^3\text{He},d$) reactions to ^{143}Pm , ^{144}Pm , ^{145}Pm . When the experiments were undertaken the uncertainty in the Q value for the $^{142}\text{Nd}(^3\text{He},d)^{143}\text{Pm}$ reaction was greater than 300 keV (Maples et al. 1966), and consequently would have affected the earlier analyses. Fortunately, however, the proton transfer experiments allowed the reaction Q values and their differences to be measured very accurately since the ^{143}Nd targets contained ^{142}Nd and ^{144}Nd impurities.

Using the target and projectile masses from Mattauch et al. (1965), and the known calibrations for the analyzing magnet and spectrograph, the ($^3\text{He},d$) Q values were calculated from the best resolution exposures at 24 and 27 MeV. Although the experimental values differed by <15 keV an uncertainty of 20 keV has been adopted to account for possible errors in the magnet calibrations. (Elastic exposures, taken at the end of some runs to compare the analyzing magnet and spectrograph calibrations showed consistency.) The measured Q values, given in Table A2.1, are in agreement with those recently published by Gove and Wapstra (1972), but disagree with the Q value for the $^{142}\text{Nd}(^3\text{He},d)^{143}\text{Pm}$ reaction, measured by Wildenthal et al. (1971) and found to be -1.099(25) MeV.

Although the measured Q values have relatively large uncer-

Table A2.1

 $(^3\text{He},d)$ Q Values

Reaction	Q values (MeV)	
	This Work	Gove and Wapstra, (1972)
1 $^{142}\text{Nd}(^3\text{He},d)^{143}\text{Pm}$	-1.219(20)	-1.220(11)
2 $^{143}\text{Nd}(^3\text{He},d)^{144}\text{Pm}$	-0.815(20)	-0.830(40)
3 $^{144}\text{Nd}(^3\text{He},d)^{145}\text{Pm}$	-0.712(20)	-0.686(7)

tainties their differences can be found with much higher precision.

For the reactions $A(a,b)B$ and $A'(a,b)B'$ at a given beam energy

$(Q-Q') = (T_B - T_{B'}) + (T_b, -T_{b'})$ where T denotes kinetic energy. The term $(T_b, -T_{b'})$ was measured from the positions of the ground states of ^{143}Pm , ^{144}Pm and ^{145}Pm which were present on each of the $(^3\text{He},d)$ and (α,t) exposures. An additional (α,t) exposure was made at 27 MeV using a target containing a mixture of enriched ^{142}Nd and ^{144}Nd . The quantity $(T_B - T_{B'})$, which was calculated using the accepted masses, Q values and beam energies, is typically a few keV and is not sensitive to realistic changes in the parameters. The Q value differences employed in the present work are $(Q_3 - Q_2) = 105.2(1.6)$ keV; $(Q_3 - Q_1) = 508.0(1.3)$ keV and $(Q_2 - Q_1) = 402.7(1.6)$ keV, the subscripts denoting the reaction listed in Table A2.1.

These Q values, and more especially their differences, could be useful in resolving the mass discrepancies which are known to exist in this region (Wapstra and Gove 1971). For example, the mass doublet $^{144}\text{Sm} - ^{144}\text{Nd}$ is given as 1817(3) keV by McLatchie et al. (1964) and 1780.2(1.0) keV by Meredith and Barber (1972). Taken with data from the $^{144}\text{Sm}(n,\gamma)^{145}\text{Sm}$ and $^{145}\text{Sm}(e.c.)^{145}\text{Pm}$ reaction (Wapstra and Gove 1971), the Q value for the $^{144}\text{Nd}(^3\text{He},d)^{145}\text{Pm}$ reaction yields a value of 1811(22) keV, in agreement with that given by McLatchie.

APPENDIX 3

A3.1 γ Ray Absorption in Targets

The targets used in the (α,n) and (p,n) reactions were sufficiently thick to stop the incident beams. Consequently the α particles can penetrate ~0.06mm into the target before their energy falls below the reaction threshold, while the corresponding distance for protons is ~0.4mm. A 60 keV γ ray produced by reactions at these depths would be attenuated by ~30% in the (α,n) reaction and ~90% in the (p,n) reaction. For γ rays >500 keV the attenuation would be <3% in both reactions. Hence, in order to measure branching ratios or compare relative γ ray intensities in the different reactions, it is clear that the observed intensities of the relatively low energy γ rays must be corrected for attenuation in the targets. This is especially important for targets with high Z.

The attenuation estimated for the 60 keV line are crude estimates, since the γ radiation produced by each reaction emanates from all parts of the target where the (α,n) and (p,n) reaction can occur. The extent of this region is determined by the incident particle energy, reaction threshold, and stopping power of the beam in the target. The fraction (f) of γ rays of a given energy which are detected, is given by

$$f = \frac{\int \sigma(E) \exp(-\mu x / \cos\theta) dx}{\int \sigma(E) dx} \quad \text{A3.1}$$

where $\sigma(E)$ is the reaction cross section for beam energy E, μ is the appropriate γ ray absorption coefficient, x is the penetration distance

of the beam, and θ is the angle between the detector and the normal to the target. It is assumed that this normal is anti-parallel to the beam direction and that the detector is on the same side of the target as the incident beam. The latter condition must hold for A3.1 to be valid.

The relative cross section dependences on particle energy were deduced from the experimentally measured excitation functions for the $^{139}\text{La}(\alpha, n)^{142}\text{Pr}$ reaction (Verdieck 1967) and for the $^{142}\text{Ce}(p, n)^{142}\text{Pr}$ reaction (Furukawa 1967). Absorption coefficients for each γ ray of interest were calculated using the photon cross section data tabulated by Strom and Israel (1970). For a given penetration distance the beam energy was determined from the stopping power data of Williamson et al. (1966), and hence $\sigma(E)$ found. Expression A3.1 was numerically integrated treating several hundred dx elements. For low energy γ rays the attenuation due to the target is much larger for the (p,n) reaction than the (α, n) reaction on account of the much larger depth of penetration of the protons, whereas the attenuation is negligible for γ ray energies >300 keV in both reactions. This is illustrated in Fig. A3.1.

The finite solid angle, subtended by each detector, gives rise to uncertainties in f , since expression A3.1 is valid only if the solid angle is negligible. Other sources of error rise from uncertainties in μ , $\sigma(E)$ and the stopping power data. The effects of these errors in f have been estimated in table A3.1 for different γ ray energies.

Fig. A3.1

γ ray attenuation due to the targets used in the
(α, n) and (p, n) reactions.

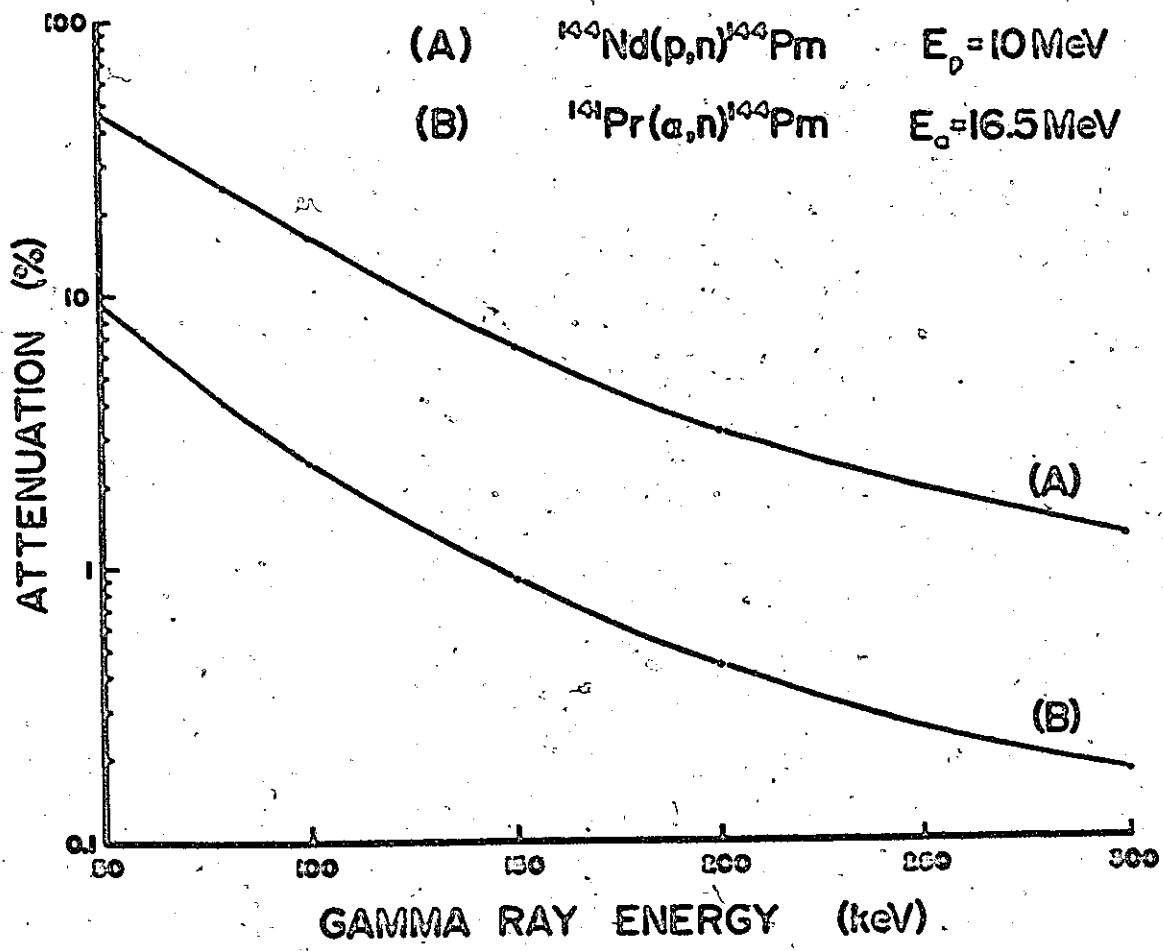


Table A3.1

Uncertainties in γ ray attenuation

Reaction	% error in f			
	E_{γ} (keV) =	50	100	200
$^{141}\text{Pr}(\alpha, n)^{144}\text{Pm}$ $E_{\alpha} = 16.5 \text{ MeV}$		2	1	0.5
$^{144}\text{Nd}(p, n)^{144}\text{Pm}$ $E_p = 10 \text{ MeV}$		10	4	1

APPENDIX 4

A4.1 Decay of ^{144}Pm

The decay of ^{144}Pm has been studied by Pagden et al. (1963) and Bunney et al. (1964), their results being consistent with a ground state half-life of ~ 360 days. The decay proceeds almost exclusively by electron capture to excited states in ^{144}Nd , which subsequently decay by γ emission. Lines are observed at 417.8, 617.8 and 696.6 keV, while other lines account for $\sim 2\%$ of the branches.

In the work of Pagden et al., a ^{144}Pm source was prepared by the (p,n) reaction on $^{144}\text{Nd}_2\text{O}_3$ (isotopic enrichment 96%) with a beam energy of ~ 10 MeV. The off-line γ ray activity from the source was then studied over a period of 2 years. Although each of the three γ rays yielded decay curves which were consistent with the ~ 360 day half-life of ^{144}Pm , they exhibited an additional period with a half-life of ~ 60 days.

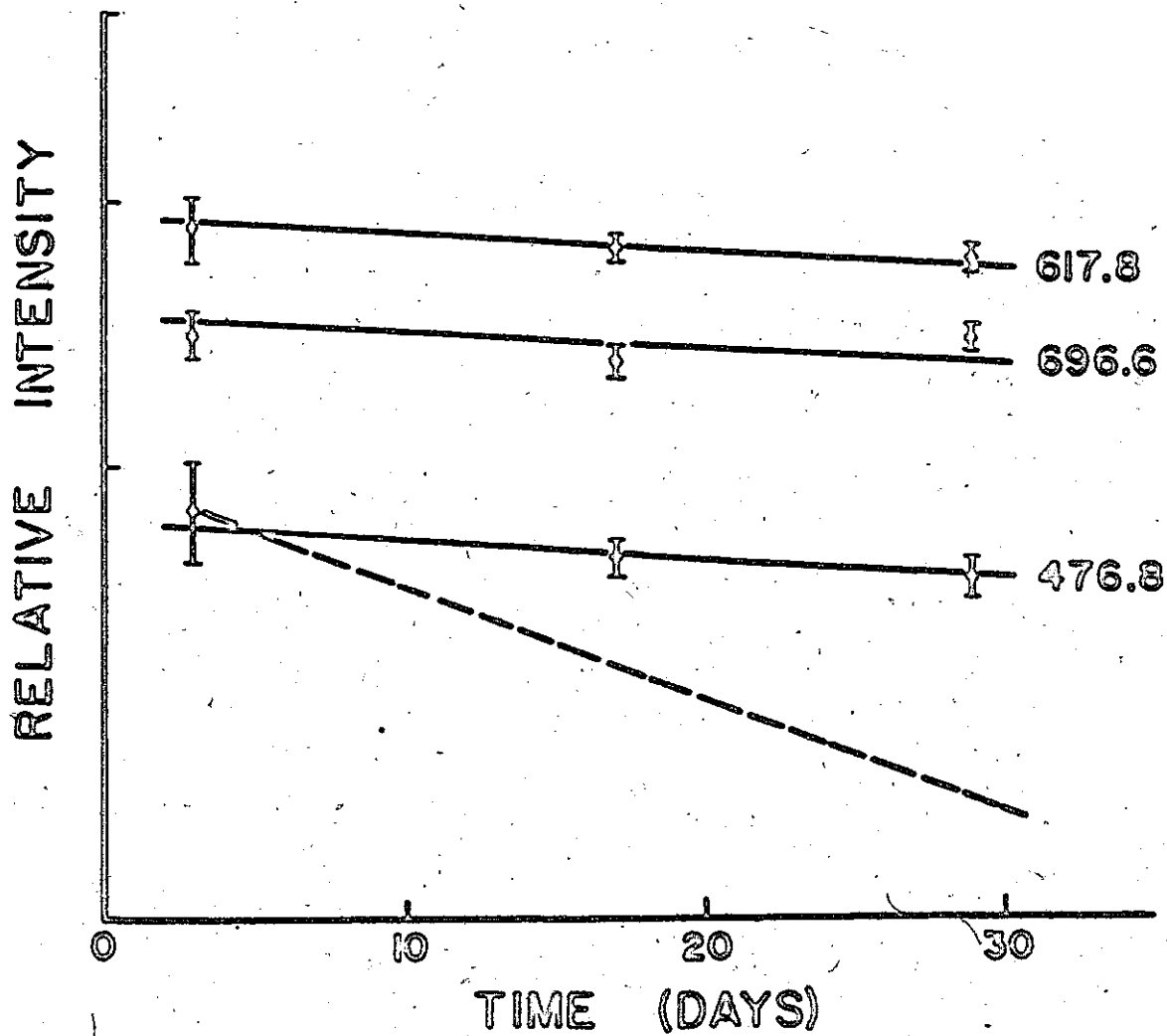
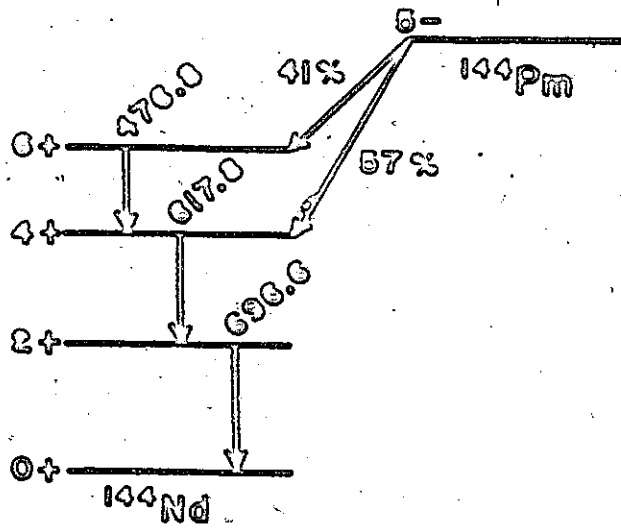
The presence of such an isomeric state could be difficult to detect in both the proton transfer and in-beam γ ray studies. For example, a 1^- state (one of the "missing" states) at ~ 60 keV would be weakly populated in the proton transfer reactions and would not be resolved from the 4^- state at 60.737 keV. γ rays feeding this state would reasonably be attributed to the 4^- state. If such a state were present it could have an appreciable lifetime. (The 6^- state in ^{148}Pm , which decays by a 61 keV E4 transition, has a half life of

43 days.)

The targets used in the (α,n) and (p,n) experiments were therefore studied off-line, with a high resolution $12 \text{ cm}^3 \text{ Ge(Li)}$ detector (courtesy of the McMaster β and γ ray spectroscopy group). The decays of the strongest lines are shown in Fig. A4.1 for the (p,n) target. There is no indication of a 60 day component in the data, nor was there in a similar experiment using the (α,n) target.

Fig. A4.1

Decay of strongest lines from (p,n) target. Solid line denotes half life of 360 days, while dashed line represents an additional half life of 60 days. Weak branches in the decay scheme are not shown.



REFERENCES

- Agarwal, Y.K., Baba, C.K. and Bhattacharjee, S.K. 1964. Nucl. Phys. 58, 641.
- Aniol, K. 1973. M.Sc. Thesis, McMaster University.
- Antman, S., Pettersson, H., Zehlev, Z. and Adam, I. 1970. Z. Physik 237, 292.
- Arya, A.P., Turk, M. and Arya, P.A. 1971. Phys. Rev. C3, 1615.
- Aubin, G., Barrette, J., Barrette, M. and Monaro, S. 1969. Nucl. Instr. and Meth. 76, 93.
- Austern, N., Drisko, R.M., Halbert, E.C. and Satchler, G.R. 1964. Phys. Rev. B133, 3.
- Bäcklin, A. and Malmskog, S.G. 1967. Arkiv Fysik 34, 531.
- Brahmavar, S.M. and Hamilton, J.H. 1969. Nucl. Instr. and Meth. 69, 353.
- Brosi, A.R., Ketelle, B.H., Thomas, H.C. and Kerr, R.J. 1959. Phys. Rev. 113, 239.
- Bunney, L.R. and Scadden, E.M. 1964. J. Inorg. Nucl. Chem. 26, 1795.
- Burde, J., Rakavy, M. and Adam, G. 1965. Nucl. Phys. 68, 561.
- Burke, D. G. Private Communication.
- Chase, R.L. 1968. Rev. Sci. Instr. 39, 1318.
- Chiao, L.W. and Martin, M.J. 1967. Nucl. Data B2-1-81.
- Daniels, J.M. and Felsteiner, J. 1968. Can. J. Phys. 46, 1849.
- Dave, V.R., Nelson, J.A. and Wilenzick, R.M. 1970. Nucl. Phys. A142, 619.
- Davidson, J.P. 1968. "Collective Models of the Nucleus" Academic Press.
- de Frenne, D., Hoyde, K., Dorikens-Vanpraet, L., Dorikens, M. and Demuyck, J. 1968. Nucl. Phys. A110, 273.
- de Shalit, A. and Talmi, I. 1963. "Nuclear Shell Theory" Academic Press.

- Dohan, D.A. 1972. Ph.D. Thesis, McMaster University.
- Eisenberg, J.M. and Greiner, W. 1972. "Nuclear Theory" vol. I, North Holland Publishing Co.
- Ejiri, H., Shibata, T. and Satch, K. 1972. Phys. Lett. 38B, 73.
- Flynn, E.R., Armstrong, D.D., Beery, J.G. and Blair, A.G. 1969. Phys. Rev. 182, 1113.
- Furukawa, M. 1967. Nucl. Phys. A90, 253.
- Geiger, J.S., Graham, R.L. and Ewan, G.T. 1961. Bull. Am. Phys. Soc. 6, 71.
- Gove, N.B. and Wapstra, A.H. 1972. Nucl. Data Tables 11, 127.
- Green, I.M. and Mozkowski, S.A. 1965. Phys. Rev. B139, 790.
- Greenwood, R.C., Helmer, R.G. and Gehrke, R.J. 1970. Nucl. Instr. and Meth. 77, 141.
- Gunnick, R., Meyer, R.A., Niday, J.B. and Anderson, R.P. 1968. Nucl. Instr. and Meth. 65, 26.
- Hafele, J.C., Flynn, E.R. and Blair, A.G. 1967. Phys. Rev. 155, 1238.
- Hansen, O., Nathan, O., Vistisen, L. and Chapman, R. 1968. Nucl. Phys. A113, 78.
- Haxel, O., Jensen, J.H.D. and Suess, H.E. 1948. Naturwiss, 35, 375.
- Haxel, O. 1949. Phys. Rev. 75, 1766.
- Helmer, R.G., Greenwood, R.C. and Gehrke, R.J. 1971. Nucl. Instr. and Meth. 96, 173.
- Hesse, K. 1969. Z. Physik, 226, 328.
- Heyde, K. and Brussaard, P.J. 1963. Nucl. Phys. A112, 494.
- Holm, G.B., Borg, J. and Rydberg, B. 1970. Conference on the Properties of Nuclei far from the Region of Beta-Stability, Leysin, Switzerland.
- Hussein, S.G. 1973. Ph.D. Thesis, McMaster University.
- Ishimatsu, T., Ohmura, H., Awaya, T., Nakagawa, T., Orihara, H. and Yagi, K. 1969. J. Phys. Soc. Japan 27, 504.

- Journey, E.T., Sheline, R.K., Shera, E.B., Koch, H.R., Maier, B.P.K., Gruber, U., Bader, H., Breitig, D., Schult, O.W.B., Kern, J. and Struble, G.L. 1970. Phys. Rev. C2, 2323.
- Kern, J., Struble, G.L. and Sheline, R.K. 1967. Phys. Rev. 153, 1331.
- Kern, J., Struble, G.L., Sheline, R.K., Journey, E.T., Koch, H.R., Maier, B.P.K., Gruber, U. and Schult, O.W.B. 1968. Phys. Rev. 173, 1133.
- Lederer, C.M., Hollander, J.M. and Perlman, I. 1968. "Table of Isotopes". Wiley and Sons, Inc.
- Lew, H. 1970. Phys. in Can. 26, 25.
- Lu, M.T. and Alford, W.P. 1971. Phys. Rev. C3, 1243.
- Macfarlane, M.H. and French, J.B. 1960. Rev. Mod. Phys. 32, 567.
- Mang, H.J. and Weidenmuller, H.A. 1968. Ann. Rev. Nucl. Sci. 18, 1.
- Maples, C., Goth, G.W. and Cerny, J. 1966. Nucl. Data A2, 429.
- Marion, J.B. and Young, F.C. 1968. "Nuclear Reaction Analysis" North Holland Publishing Co.
- Mayer, M. 1948. Phys. Rev. 74, 235.
- 1949. Phys. Rev. 75, 1969.
- McFadden, L. and Satchler, G.R. 1966. Nucl. Phys. 84, 177.
- McGowan, F.K., Milner, W.T., Kim, H.J. and Hyatt, W. 1969. Nucl. Data A7, 1.
- McLatchie, W., Barber, R.C., Duckworth, H.E. and Van Rookhuyzen, P. 1964. Phys. Lett. A10, 330.
- Meredith, J.O. and Barber, R.C. 1972. Can. J. Phys. 50, 1195.
- Monnard, E., Brissot, R., Carray, L.C., Crancen, J., Ristori, C., Schussler, G. and Moussa, A. 1972. Nucl. Phys. A195, 192.
- O'Neil, R.A. 1970. Private Communication.
- Pagden, I.M.H., Jakeways, R. and Flack, F.C. 1963. Nucl. Phys. 48, 555.
- Raman, S. 1967. Nucl. Data B2-1-47.
- Rowe, D.J. 1970. "Nuclear Collective Motion - Models and Theory" Methuen and Co. Ltd.

- Satchler, G.R. 1964. Nucl. Phys. 55, 1.
-
1965. "Lectures in Theoretical Physics", Vol. VIII C, ed. Kunz, P.D., Lind, D.A. and Britton, W.T. University of Colorado Press, Boulder (Published 1966), p. 73.
- Shirley, D.A., Schooley, J.F. and Rasmussen, J.O. 1961. Phys. Rev. 121, 558.
- Sliv, L.A. and Kharitonov, Y.I. 1968. "Spectroscopic and Group Theoretical Methods in Physics" North Holland Publishing Co.
- Spencer, J.E. and Enge, H.A. 1966. Nucl. Instr. and Meth. 49, 181.
- Storm, E. and Israel, H.I. 1970. Nucl. Data Tables 7, 565.
- Struble, G.L. 1967. Phys. Rev. 153, 1347.
- Toth, K.S., Handley, T.H., Newman, E. and Williams, I.R. 1964. Phys. Rev. B136, 1233.
- Verdieck, E.V. and Miller, J.M. 1967. Phys. Rev. 153, 1253.
- Wapstra, A.H. and Gove, N.B. 1971. Nucl. Data Tables 9, 265.
- Westgaard, L. and Bjørnholm, S. 1966. Nucl. Instr. and Meth. 42, 77.
- White, D.H., Birkett, R.E. and Thomson, T. 1970. Nucl. Instr. and Meth. 77, 261.
- Wildenthal, B.H. 1969. Phys. Rev. Lett. 22, 1118.
- Wildenthal, B.H., Newman, E. and Auble, R.L. 1971. Phys. Rev. C3, 1199.
- Williams, G.N. and McPherson, D. 1968. CRNL PR-P-76 (Unpublished).
- Williamson, C.F., Boujot, J.P. and Picard, J. 1966. "Tables of Range and Stopping Power of Chemical Elements for Charged Particles of Energy 0.05 to 500 MeV", Report CEA-R 3042, Commissariat à l'Energie Atomique - France.
- Yoshida, S. and Zamick, L. 1972. Ann. Rev. Nucl. Sci. 22, 121.